K^+p INTERACTIONS at 10 GeV/c

and

POLLY — A FILM MEASURING MACHINE

JOHN W. P. McCORMICK

SUBMITTED AS A THESIS FOR THE DEGREE OF Ph.D.

IN

THE UNIVERSITY OF GLASGOW

OCTOBER 1971

ProQuest LLC.
789 East Eisenhower Parkway
P.O. Box 1346
Ann Arbor, MI 48106 – 1346

K^+p Interactions at 10 GeV/c

and

Polly - A Film Measuring Machine.

John W.P. McCormick, B.Sc.

This thesis contains the work of the author on an experiment to study the interactions of positive K-mesons with protons at an incident laboratory momentum of 10 GeV/c. It also includes a description of the author's work in implementing a computer controlled bubble chamber film measuring device, Polly, at Glasgow University.

A brief survey of current theoretical ideas relevant to the following work on high energy physics is given in Chapter I. Chapter II describes the experiment, which was a Birmingham-Glasgow-Oxford collaboration using the C.E.R.N. Proton Synchrotron and 2 metre hydrogen bubble chamber. The Glasgow bubble chamber group system of analysis programmes is summarised, and the measurement and analysis of the events in which six charged particles were produced is described.

The results of a spin-parity analysis of the $I=\frac{1}{2}$ low mass baryon system formed in four prong events are shown in Chapter III. These indicate that spin-parities 3/2 and 5/2 states are present, but no evidence for $\frac{1}{2}^+$ states with a $\Delta(1236)\pi$ decay mode was obtained.

Chapter IV is based on the observation of an I=3/2 baryon resonance at 1.9 GeV/c^2 in the four and five body final states.

The branching ratios of this resonance are evaluated, and are compared with results obtained from other experiments.

The theory of single particle momentum distributions has received attention recently: the momentum distributions for negative pions and neutral kaons produced in the experiment are presented in Chapter V, and compared with published data at different beam momenta. The results indicate that the scaling behaviour of the centre-of-mass longitudinal momentum with centre-of-mass energy is not observed in K^+p interactions at around 10 GeV/c incident momentum, although further data from other experiments will be required before this can be definitely established.

The remaining two chapters deal with the aspects of the computer controlled film measuring device, Polly, which have concerned the author. The extraction of bubble density information from the Polly data is treated in depth, and, although at the time of writing Polly had not reached the production stage, the predictions of the derived equations are shown to agree with the Polly data available.

The appendix to this thesis explains the amplitude terms used in the analysis in Chapter III.

Preface

This thesis falls into two parts, the first of which (Chapters I-V) contains a description of the author's work on inelastic interactions of positive kaons with protons at an incident laboratory momentum of 10 GeV/c. The second part of the thesis (Chapters VI and VII) gives an account of the author's work on the development of a computer controlled film measuring machine, Polly.

In Chapter I there is an outline of current theoretical ideas of relevance to the analysis which follows.

Chapter II describes the film measuring, data handling, and analysis, and also contains an account of the author's work in measuring and analysing the six prong events.

The $I=\frac{1}{2}$ N^* resonances which are observed in the four body final states are discussed in Chapter III. Details of a spin-parity analysis carried out by the author are included in this chapter.

Chapter IV describes the $I=3/2$ $\Delta^{++}(1900)$ resonance which is seen in four and five body final states. Branching ratios, and mass and width are obtained for this resonance.

Recently, much interest has been shown by theorists in single particle distributions. The author carried out an analysis of the momentum spectrum of particles in the common 10 GeV/c reactions, with from two to seven particles in the final state, and of the single particle distributions of negative pions and uncharged kaons. This work is included in Chapter V. Comparisons with other experiments indicate

that more data will be required before the validity of the limiting fragmentation ideas referred to in Chapter I can be established. Chapters III, IV, and V are solely the work of the author.

Chapter VI consists of a brief description of some measuring machines, including Polly, which is currently comissioned at Glasgow. Those aspects of the Polly design which were the responsibility of the author are described in some detail.

Finally, in Chapter VII, the important subject of extracting bubble density information from the Polly measurements is discussed, and a formula is derived by the author, and is compared with data.

ACKNOWLEDGEMENTS

The author wishes to thank Professor I.S.Hughes for his help and supervision, and Dr. C. J. Robinson and Dr. R. M. Turnbull for their many helpful discussions.

The author is indebted to the scanning, measuring and computing staff of the Universities of Glasgow, Birmingham and Oxford, and to the crews of the CERN Proton Synchrotron and 2 metre hydrogen bubble chamber. He is grateful to all members of the Glasgow Bubble Chamber Group who have assisted him with difficulties in computing and analysis.

The author gratefully thanks his wife, who typed this thesis, and who gave encouragement and help in the preparation of this work.

Finally, thanks are due to Professor P.I.Dee for the hospitality of his department, and the Science Research Council for the award of a research studentship.

Publications

Observation of a four pion resonance at 1630 MeV in K^+p interactions at 10 GeV/c

Physical Review Letters, 24, 1083 (1970)

K.W.J.Barnham,D.C.Colley,M.Jobes,I.R.Kenyon,K.Pathak, L.Riddiford and P.M.Watkins,

Department of Physics, University of Birmingham.

I.Griffiths,I.S.Hughes,J.W.P.McCormick,I.McLaren, C.D.Procter,R.M.Turnbull,I.R.White,

Department of Natural Philosophy,University of Glasgow.

Study of the L-Meson in 10 GeV/c K^+p Interactions

Nuclear Physics B 26, 71 (1971)

D.C.Colley, M.Jobes,I.R.Kenyon,K.Pathak and P.M.Watkins,

Department of Physics,University of Birmingham

I.S.Hughes,J.W.P.McCormick,C.D.Procter,R.M.Turnbull and I.R.White

Department of Natural Philosophy,University of Glasgow.

Observation of a Strangeness +1 Meson with a Mass of 2800 MeV/c^2

Invited Paper to the International Conference on Meson Resonances and Related Electromagnetic Phenomena,Bologna 1971.

I.Hughes, J.McCormick,C.Procter,R.Turnbull,

University of Glasgow.

Progress on Polly at Glasgow

Paper Presented at International Conference on Data Handling Systems in High-Energy Physics, Cambridge 1970

R.Benetta, G.K.S.Browning, A.P.Conway, T.Finlay, J.W.P.McCormick, H.A.O'Donnell, R.O'Neill and C.J.Robinson.

University of Glasgow.

Presentations by the Collaboration

The following papers have been read at the stated conferences:

A study of the L-meson in 10 GeV/c K^+p interactions.
International Conference on Elementary Particles, Kiev 1970
Birmingham-Glasgow collaboration.

$I=\frac{1}{2}$ resonance production in the $p\pi\pi\pi$ system in 10 GeV/c K^+p interactions.
International Conference on Elementary Particles, Kiev 1970
Birmingham-Glasgow-Oxford collaboration.

Study of $N^*(1700)$ in K^+p interactions at 10 GeV/c
Conference on High Energy Physics, Durham 1970
Birmingham-Glasgow-Oxford collaboration.

Study of the L-meson in 10 GeV/c K^+p interactions
Conference on High Energy Physics, Durham 1970
Birmingham-Glasgow collaboration.

$\Delta^{++}(1900)$ production in K^+p interactions at 10 GeV/c
Conference on High Energy Physics, Lancaster 1971
Birmingham-Glasgow-Oxford collaboration

CONTENTS

Chapter I

Introduction

I.1 Introduction

To search for a theoretical understanding of strong interactions, two approaches can be adopted. In the first of these reaction mechanisms can be investigated. The second approach consists of studying resonance properties. The two methods are complementary; any successful theory of strong interactions would explain the nature of the forces between elementary particles, as revealed by the first approach, and would account for the existence of the known particles and resonances. The theoretical models which have gained some success in describing high energy phenomena are reviewed briefly in this chapter.

I.2 SU_2

The equivalence of neutrons and protons in strong interactions within nuclei led to the concept of these two particles being different charge states within an isotopic spin doublet. Other strongly interacting particles subsequently found could also be grouped into isotopic spin multiplets, each of these multiplets forming an SU_2 group. The rules for combining isotopic spin states are the same as these for ordinary spin. The predictions of isotopic spin invariance of strong interactions have been confirmed, for example in pion-nucleon scattering and strong decay branching ratios of resonances.

I.3 Sakata Model

The extension of the use of SU_2 to include strange particles led originally to the Sakata model (ref. 1.1). All strongly interacting particles and resonances were postulated to be combinations of λ, p, n, and their antiparticles. Mesonic states formed from pairs of the basic Sakatons occur in groups of 9, and reasonable agreement with the experimental situation was achieved. Difficulties arose in the description of the baryon spectrum. In the Sakata model, baryons consist of two Sakatons and one anti-Sakaton. Thus each group of baryons should consist of 27 states, including some for which there is no experimental evidence, e.g. S=1, B = 1 baryons. Another failing of the model was that Σ and ξ particles were treated as composite particles formed by combining the basic n, p, λ states, yet no apparent physical reason existed for choosing the λ state as basic, in preference to the Σ or ξ. In addition, the J^P assignment for the Σ was incorrect.

I.4 SU_3

Gell-Mann and Ne'eman (ref. 1.2) used the SU_3 algebra (ref. 1.3) to obtain a scheme which successfully classifies the $\frac{1}{2}^+$ baryons into octet structures, and the mesons into singlet and octet structures (figure 1.1(a) illustrates the 1^- mesons), with the $3/2^+$ baryons forming an SU_3 decuplet. The SU_3 multiplet structures are characterised by the values of 2T (twice the isotopic spin) corresponding to the isotopic spin subset with highest hypercharge ($2T_{MAX} = \lambda$, say), and with lowest hypercharge ($2T_{MIN} = \mu$, say). Each

multiplet contains particles of a given spin, parity, and baryon number.

SU_3 algebra generates structures which are symmetrical under rotation through 120°. This leads to the concept of u-spin and v-spin, which in SU_3 are analogous to I-spin, with the relative orientation of the I, u, and v axes as shown in figure 1.1(b). Particles lying perpendicular to the u-axis have the same electric charge, Q. When one member of a multiplet is found, SU_3 predicts that all other members of the multiplet should exist. The discovery of the Ω^- after its mass and other properties had been predicted by the SU_3 classification scheme was one of the major triumphs of the scheme. The proliferation of non-strange baryon states found from phase shift analysis has introduced multiplets which have not been completely established. Work must be devoted to finding strange baryon candidates which will fill the vacancies in these multiplets.

I.5 Quark Model

The Quark model of Gell-Mann (ref 1.4) and Zweig gives a physical basis for the SU_3 classification scheme. All mesons in the Quark model are composed of quark-antiquark pairs, and baryons are three quark systems. The properties of the quarks are shown in figure 1.4. The Quark model yields similar results for the mesons as the Sakata model, but for the baryons, the combination of three quarks results in a singlet, two octets, and one decuplet of possible states. This is in much better agreement with the baryon spectrum than the

'27-plets' of the Sakata model. Exotic states, with for example B = 1, S = 1, or doubly charged mesons, which could be accommodated in the SU_3 classification scheme, cannot be made up from three quarks, and therefore the quark model predicts that such states should not exist. Much effort has been devoted to searching for exotic states, but, although there have been reports supporting the existence of Z^*'s, it appears that at the moment insufficient evidence exists for the rejection of the Quark model. The physical existence of quarks has not yet been established. The quark mass does not appear in any predictive equation, and so is indeterminate. This fact makes the experimental search for the quark more difficult.

I.6 SU_6

When the spin of the quarks was taken into account, by Sakita (ref. 1.6), he obtained a higher scheme, which classifies together the SU_3 multiplets corresponding to different J^P values. Since the quarks have spin $\frac{1}{2}$, the $q\bar{q}$ meson states can have spin-parity 0^- or 1^-. The qqq baryon states can have spin $\frac{1}{2}$ or 3/2. The basic baryon SU_6 representation contains 6^3, or 216, states, since each quark of the qqq trio may be p,n or λ and have spin up or down. The 216 states are composed of four subsets which contain, respectively, 20, 56, 70 and 70 states. (Higher spin baryons are also included in the SU_6 scheme when the orbital angular momentum of the quark system is considered). The subset containing 56 states is shown in figure 1.1(c).

Since the other subsets, containing 20, and 70 states, are not in evidence, it is assumed that only states for which the overall quark wave function is symmetric (ref. 1.7) (e.g. 56, L=0) can exist (ref. 1.8), while states which are not completely symmetric (70, L=0, and 20, L=0) cannot. The Roper resonance ($N^*(1470)$), and its SU_3 partners which are not yet well established, lie outside the main sequence. It has been suggested that a radially excited system of quarks could account for these.

I.7 Regge Theory and Regge Trajectory Exchange

The Regge Pole hypothesis (ref. 1.9) predicts that groups of particles with identical quantum numbers (apart from spin) should lie on smooth trajectories on a Chew-Frautschi plot of spin, J, against the square of the particle mass, M . Regge studied the solutions of the Schroedinger equation, for scattering in a Yukawa potential. The scattering amplitude can be expressed as:

$$F(E,\theta) = \sum_{n=0}^{\infty} (2n+1)\, P_n(\cos\theta)\, f_n(E) \qquad (1.1)$$

where the coefficient of the n'th Legendre Polynomial, $P_n(\cos\theta)$, is a function of the energy, E. Regge expressed the scattering amplitude in terms of the integral over the complex l-plane:

$$\frac{1}{2i}\int \frac{dl\,(2l+1)}{\sin \pi l}\; P_l(-\cos\theta)\, f(E,l) \qquad (1.2)$$

which has poles for integral values of 'l', giving the normal scattering amplitude (1.1). The poles of f(E,l) also contribute to the integral: f(E,l) can be expressed $f(E,l) = \frac{\beta(E)}{l-\alpha(E)}$ where $\alpha(E)$ is a Regge Pole trajectory. If at some energy E_n, $\mathrm{Re}\,\alpha(E_n) = n$,

$$f_n(E \sim E_n) \doteq \frac{\beta(E_n)}{\alpha'(E_n)(E_n - E) - i\ \mathrm{Im}\,\alpha(E_n)} \qquad (1.3)$$

where $\alpha'(E) = \frac{d\ \mathrm{Re}\,\alpha(E)}{dE}$

Thus for $\mathrm{Im}\,\alpha(E_n) > 0$, the scattering amplitude contains a Breit-Wigner term with central energy E_n.

The resonance contribution to the scattering amplitude (ignoring the 'background' from the ordinary partial waves) can be expressed in terms of the residues:

$$F(E,\theta) = \sum_i \frac{\pi\ \beta_i(E)\ [2\alpha_i(E) + 1]}{\sin(\pi\,\alpha_i(E))}\ P_{\alpha_i(E)}(-\cos\theta) \qquad (1.4)$$

If it is assumed that the scattering amplitude can be analytically continued from the s-channel (see figure 1.2) to the t-channel, we obtain (letting $t \to \infty$ with s small, and substituting $\cos\theta = 1 + t/(s/2-2) \to t$)

$$F(s,t) = \sum_i \frac{\pi\ \beta_i(s)(2\alpha_i(s) + 1)\ (-t)^{\alpha_i(s)}}{\sin(\pi\,\alpha_i(s))} \qquad (1.5)$$

Since we are considering 't' large, F(s,t) is dominated by the trajectory with the highest value of $\alpha_i(s)$. In the t-channel the scattering amplitude is determined by the exchange of the complete Regge trajectories corresponding to the $\alpha_i(E)$ of equation (1.4). For example, the reaction

$$\bar{p}n \longrightarrow \pi^-\pi^0$$

which would proceed predominantly via ρ-meson formation at low energy (low s), is connected to the corresponding t-channel reaction

$$\pi^+ n \longrightarrow \pi^0 p$$

at high energy (high t), where the Regge trajectory containing the ρ, A_2 etc. mesons, would be exchanged.

Although information on high mass, high spin resonances is poor, sufficient data exists to construct several Regge trajectories (see figure 1.3). Those trajectories which include two or more resonant states are parallel straight lines in the Chew-Frautschi plot.

In order to explain the diffractive production in certain reactions where the exchanged trajectory may have 'vacuum' quantum numbers, the Pomeron Trajectory was introduced. It has been known for some time that the total cross-section for certain reactions, e.g. $\sigma_T(K^+p)$, is almost constant with increasing energy, in the energy range where the Regge exchange model is applicable. Using the optical theorem (ref. 1.10) which relates the total cross-section to the forward part of the elastic scattering amplitude ($t = 0$), it can be shown that $\alpha_p(0) = 1$, since:

$$\sigma_T = \frac{1}{s}\sigma_{el}(t=0)$$
$$\propto s^{(\alpha_p(0)-1)2}$$

$\alpha_p(0) = 1$ gives a constant cross-section as energy increases. The Regge pole hypothesis has had considerable success in describing two body interactions at high energy: its extension to three particle production processes (double Regge exchange) also gives a reasonable description of the data, in the kinematic regions in which it is applicable. It fails, however, to reproduce resonant production of particles. Its power as a classification scheme for particles will be increased if future data on high spin, high mass resonances,

for example the S, T, and U mesons (ref. 1.8) provides more reliable experimental points on the linear trajectories.

I.8 Other Models

The Chan, Loskiewicz, and Allison Model[1.12] is basically an amplitude which gives multi-Regge behaviour at high energies, and phase space distributions for particle systems with low effective masses. However, at low energies, interactions are known to be dominated by resonance production, and any model consistent with duality (ref. 1.13) should give resonant behaviour in the low energy region. Neither the C.L.A. model, nor the Regge models have done this successfully.

Plahte and Roberts (ref. 1.14) modified the C.L.A. model to include two particle resonance information. Although these models have given good fits to a wide variety of data, they have been criticised for the large number of free parameters in the amplitudes, which reduce the predictive value of the models.

The Veneziano Model (ref. 1.15) uses the Euler Beta function in the scattering amplitude. This function has several desirable features, giving Regge behaviour at high energy, and resonance behaviour at low energies. However, the model does not describe diffraction dissociation processes. Computational difficulties limit its applicablity to two or three body final states.

I.9 General Characteristics of High Energy Interactions

A more general way of investigating many body final states

is to compare resonance production, single particle momentum distributions, and four-momentum transfers for different multiplicity final states, and for different beam particles.

Peyrou plots of longitudinal against transverse momentum, for different multiplicities and beam momenta, have shown that the transverse momentum distribution is independent of multiplicity and of incident energy, while the longitudinal momentum is very dependent on these quantities (ref. 1.16). It has been observed that the part of the reaction matrix element which is responsible for the behaviour of leading particles does not depend on multiplicity. For example, the F(t) distribution, obtained by dividing the experimental t(p/p) distribution by the phase space distribution, is similar for all multiplicities up to 8 prongs in π^-p interactions (ref. 1.16). The leading particle behaviour which characterises high energy interactions has led theorists to propose several models.

The isobar model (ref. 1.17) was applied originally to pp interactions at 0.8 to 3.0 GeV/c . In the production of an isobar, a transfer of kinetic energy to the nucleon from the other interacting particle may raise it to an excited state, which does not interact further with the other particles in the collision, and which subsequently decays. The model, as originally applied, gave reasonable agreement with data, assuming that all pion production was derived from the decay of the $\Delta(1236)$ isobar.

The two fireball model (ref. 1.18), based on observation of 1000 GeV/c^2 cosmic ray protons in emulsions, visualises two clouds of particles formed in the interaction, moving rapidly apart in the overall centre-of-mass system in the same direction as the primary particles. The particles within each cloud have transverse momenta of the order of .5 GeV/c.

The Diffraction Dissociation model (ref. 1.19) explains the qualitative similarity between the diffraction peak formed in elastic scattering, and the behaviour of certain types of inelastic reaction. A probability exists for the dissociation of the interacting particles into sets of resonant states and particles, governed by the conservation of relevant quantum numbers, but not by energy conservation. In the interaction, unequal absorption of the different sets of constituents will produce in the final diffracted wave states which were not present in the initial beam. Since the probability of the initial particles dissociating is independent of the rest frame from which they are observed, the diffraction dissociation model provides an explanation for the energy independence of cross-sections for inelastic diffractive reactions.

The isobar model, the two fireball model, and the diffraction dissociation model all give qualitatively similar predictions for the behaviour of the secondary particles in high energy interactions where diffractive processes dominate.

I.10 Limiting Fragmentation

Recently, Feynman (ref. 1.20) suggested that, for very high energy strong interactions, where the transverse momentum distributions are believed to be independent of the total centre-of-mass energy, the most useful variables for describing the single particle distributions are p_T (the transverse momentum) and x ($=2p_L/\sqrt{s}$) which is the ratio of the longitudinal momentum to the maximum possible (where the rest masses have been neglected compared with the energies). Feynman suggested that if the percentage of energy going to final particles of a given type is constant, i.e. $\int \frac{E\,dN}{\sqrt{s}} = \text{const.}$, A say

i.e. $$\int \frac{E}{\sqrt{s}} F(s,\underline{p})\, dp_L\, dp_T^2 = A \qquad (1.6)$$

where $F(s,\underline{p})$ is the number of particles (at total centre-of-mass energy $\sqrt{s}$) of the given type with momentum $\underline{p}$. Then, assuming that the dependence of $F(s,p_L,p_T)$ on s and p_L can be expressed as $F(x,p_T)$, (i.e. p_L scales with $\sqrt{s}$), and putting

$$EF(s,\underline{p}) = f(x,p_T)$$

equation (1.6) becomes

$$\int \tfrac{1}{2} f(x,p_T)\, dx\, dp_T^2 = A$$

which will be valid if $f(x,p_T)$ is independent of energy.

The limiting fragmentation concept of Benecke et al. (ref. 1.21) hypothesises the existence of a limit

$$\lim_{E\to\infty}\left(\frac{d^3\sigma}{d\underline{p}}\right) \longrightarrow \rho(\underline{p})$$

i.e. the partial cross-section that a particle of mass 'm' is emitted with laboratory momentum $\underline{p}$, other emitted particles being ignored, depends only on $\underline{p}$ and is independent of $\sqrt{s}$, the

centre-of-mass energy. The use of laboratory momentum arises from the concept that the fragmentation products from the target separate rapidly from the broken up fragments of the projectile. It can be shown that the limiting fragmentation hypothesis is equivalent to the scaling law for the Feynman variable x, in the limit of infinite beam momentum (see ref. 1.22). Mueller (ref. 1.23) has proposed an analogy to the optical theorem (relating the total cross-section to the imaginary part of the forward elastic scattering amplitude) which could be applied to single particle distributions. This is shown diagrammatically in figure 1.5. Although no model exists for three particle-three particle scattering, theorists have assumed that the basic principles which apply in two particle interactions, may also apply in this case. In two particle interactions, reactions in which the quantum numbers of the beam and target are exotic approach the asymptotic cross-section limit predicted by the Pomeranchuk theorem at lower energies than reactions in which s-channel resonances can be formed. Similarly, in the three particle interaction visualised by Mueller, reactions with exotic quantum numbers would be expected to reach the limiting distributions at lower energies. However, there is some interest in whether, in the reaction

$$a\ b \rightarrow c\ X$$

it is sufficient that $ab\bar{c}$ should be exotic (ref. 1.24), or whether ab must also be exotic (ref. 1.25), as suggested by Ellis et al, to give energy independent limiting distributions.

Experimental analysis of reactions of the type:

$$a + b \rightarrow c + \text{anything}$$

using bubble chamber data is complicated by the fact that unfitted events must be used in order to include reactions in which more than one neutral particle is produced. The single particle distributions which can be investigated are, therefore, restricted to particles which can be identified without kinematic fitting. This thesis is mainly concerned with K^+p interactions. Negative pions, and uncharged secondary mesons with visible charged decays, can be identified in K^+p interactions without fitting the event, and with very little contamination. The single particle distributions for π^- and K^o mesons from the 10 GeV/c K^+p experiment are compared with published data from other experiments and with the Feynman ideas mentioned above in Chapter V.

References

1.1 S.Sakata

Progress of Theoretical Physics 16, 686 (1956)

1.2 M. Gell-Mann and Y. Ne'eman

The Eightfold Way (W.A.Benjamin Inc.,New York 1965)

1.3 H.J.Lipkin

Lie Groups for Pedestrians (North Holland Publishing Co.,Amsterdam, 1965)

1.4 M.Gell-Mann

Physics Letters 8, 214 (1964)

1.5 H.M.Chan

High Energy Reactions and Regge Poles

CERN 67-16 (1967)

1.6 B.Sakita

Phys. Rev. 136 B1756 (1964)

1.7 F.R.Stannard

An Introduction to SU_3

International School at Herceg Novi, 1966

1.8 O.W Greenberg

Proceedings of the Lund International Conference on Elementary Particles (1969).

1.9 B.E.Y. Svensson

Proceedings of the 1967 CERN School of Physics

CERN 67-24

(See also references 1.5 and 1.11)

1.10 P.Waloschek

Phase Shift Analysis

International School at Herceg Novi, 1966

1.11 L.Van Hove

CERN 38-31 (1968)

1.12 H.M.Chan, J.Loskiewicz, W.W.M.Allison

Nuovo Cimento 57A,93 (1968)

1.13 K.Kajantie

Proceedings of the 1970 CERN School of Physics

Loma-Koli,

CERN 71-7

1.14 E.Plahte et al.

Nuovo Cimento Series 1,1,187 (1969)

1.15 G.Veneziano

Nuovo Cimento 57A, 190 (1968)

1.16 O.Czyzewski

Proceedings of the Vienna International Conference

on High Energy Physics (1968)

1.17 S.J. Lindenbaum and R.M. Sternheimer,

Physical Review 105,1874 (1957)

1.18 G.Cocconi

Physical Review 111, 1699 (1958)

1.19 M.L. Good and W.D.Walker

Physical Review 120, 1857 (1960)

1.20 R.P.Feynman

Physical Review Letters 23, 1415 (1969)

1.21 J.Benecke et al.

Physical Review 188, 2159 (1969)

1.22 T.T Chou and C.N.Yang

Physical Review Letters 25 (1072),1970

1.23 A.H.Mueller

Physical Review D 2, 2963 (1970)

1.24 H.M.Chan et al.

CERN Preprint Th 1339 (1971)

1.25 J.Ellis et al.

CERN Preprint Th 1316 (1971)

Figure Captions

1.1(a) 1^- meson nonet

(b) I,U and V axes

(c) A baryon octet and decuplet.

1.2 The Mandelstam variables: the shaded areas in the lower diagram represent the physical regions.

1.3 Two baryon Regge Trajectories

1.4 Quark properties.

1.5 Diagram illustrating the relation between the Optical Theorem applied to elastic scattering, and the Mueller analogy for inclusive reactions.

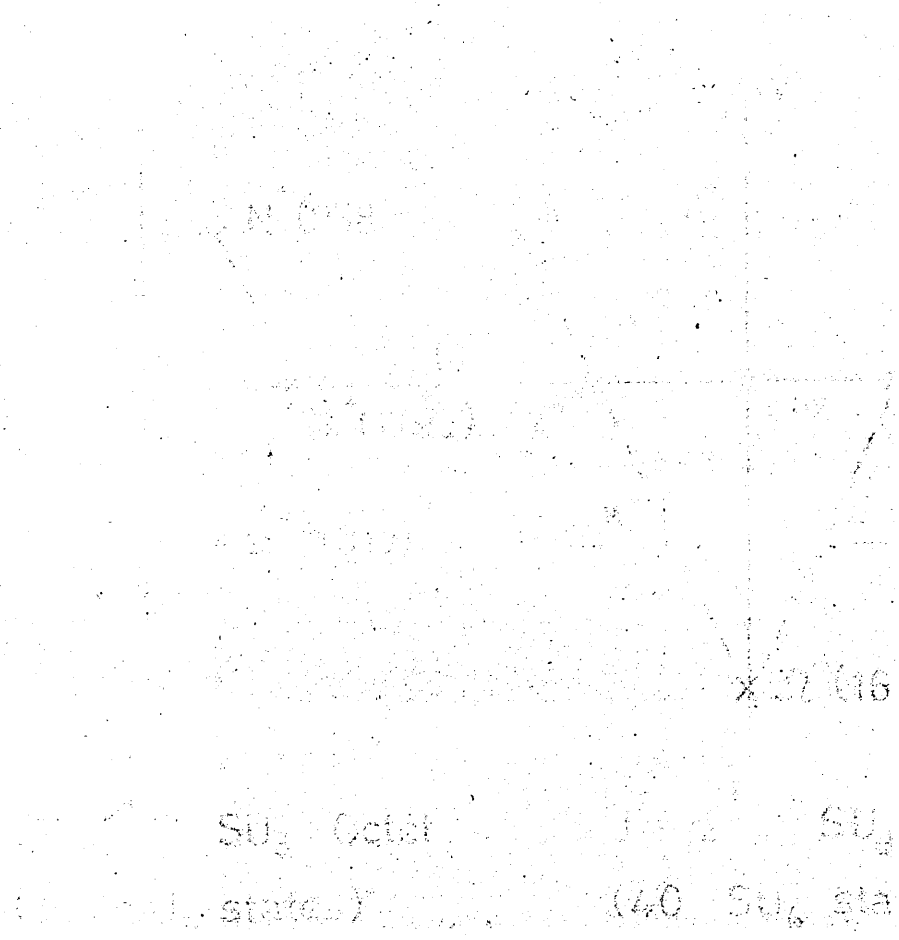

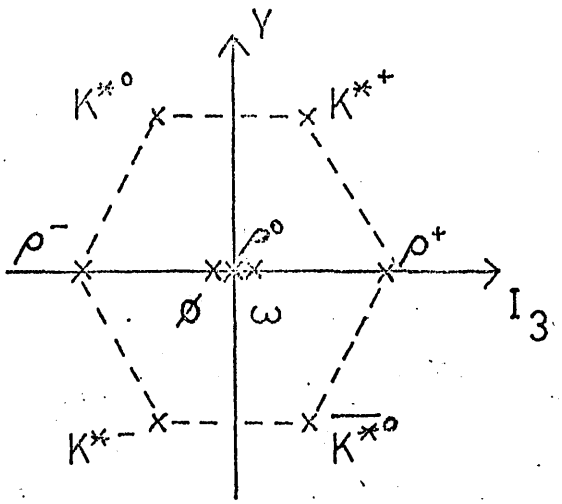

Vector Meson Nonet

$J^P = 1^-$

(a)

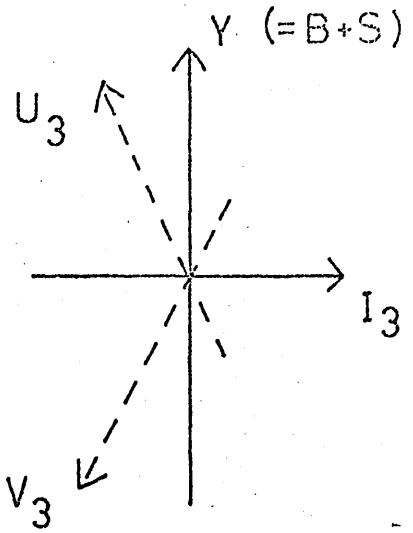

I, U and V SPIN

(b)

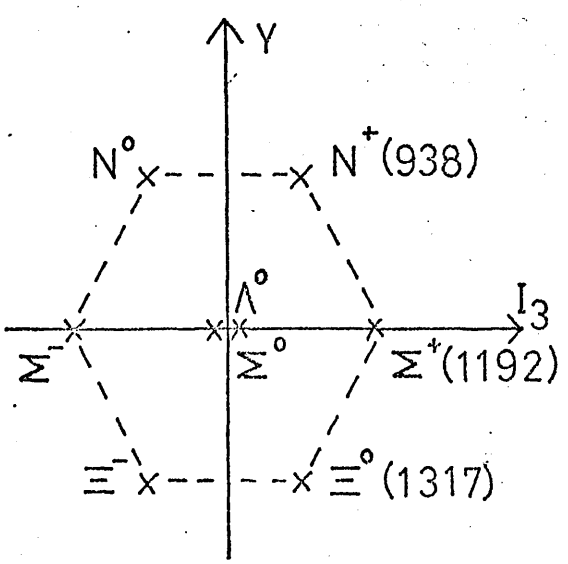

$J^P = \frac{1}{2}^+$ SU_3 Octet

(16 SU_6 states)

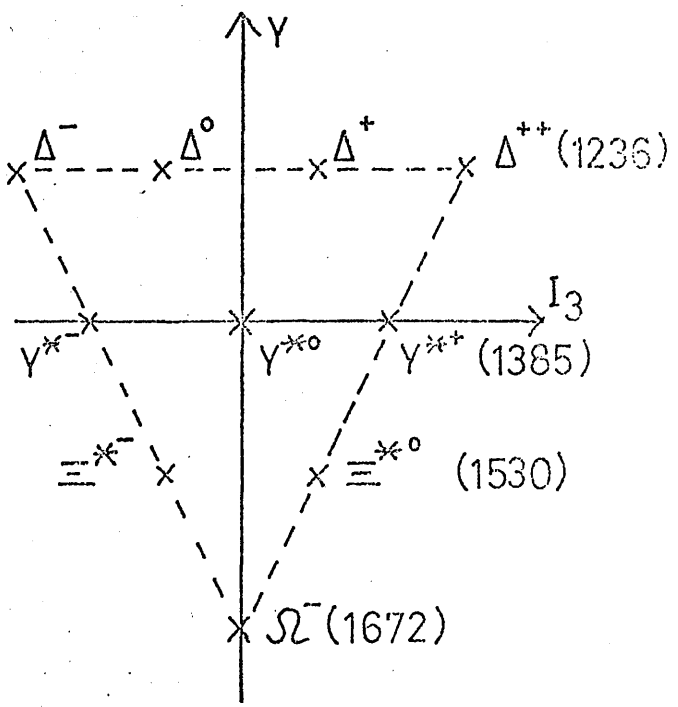

$J^P = \frac{3}{2}^+$ SU_3 Decuplet

(40 SU_6 states)

(c)

FIGURE 1.1

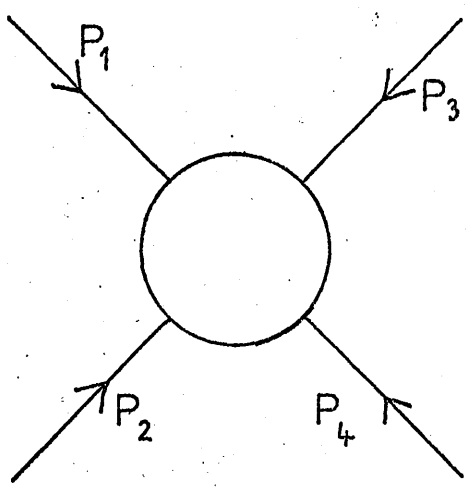

p = momentum 4 - vector

$S = (p_1 + p_2)^2$

$t = (p_1 + p_3)^2$

$u = (p_1 + p_4)^2$

MANDELSTAM VARIABLES (s, t, u)

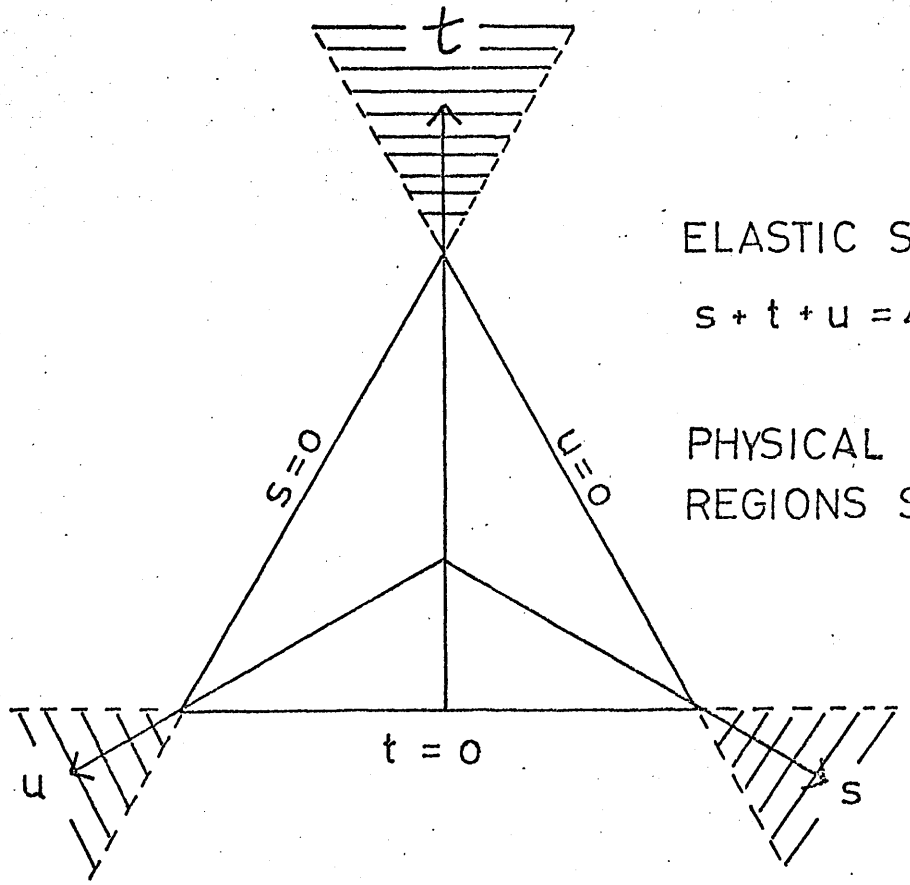

ELASTIC SCATTERING

$s + t + u = 4m^2$

PHYSICAL s, t, u
REGIONS SHADED

FIGURE 1.2

CHEW-FRAUTSCHI PLOT FOR
$I=\frac{1}{2}$ NON STRANGE BARYONS

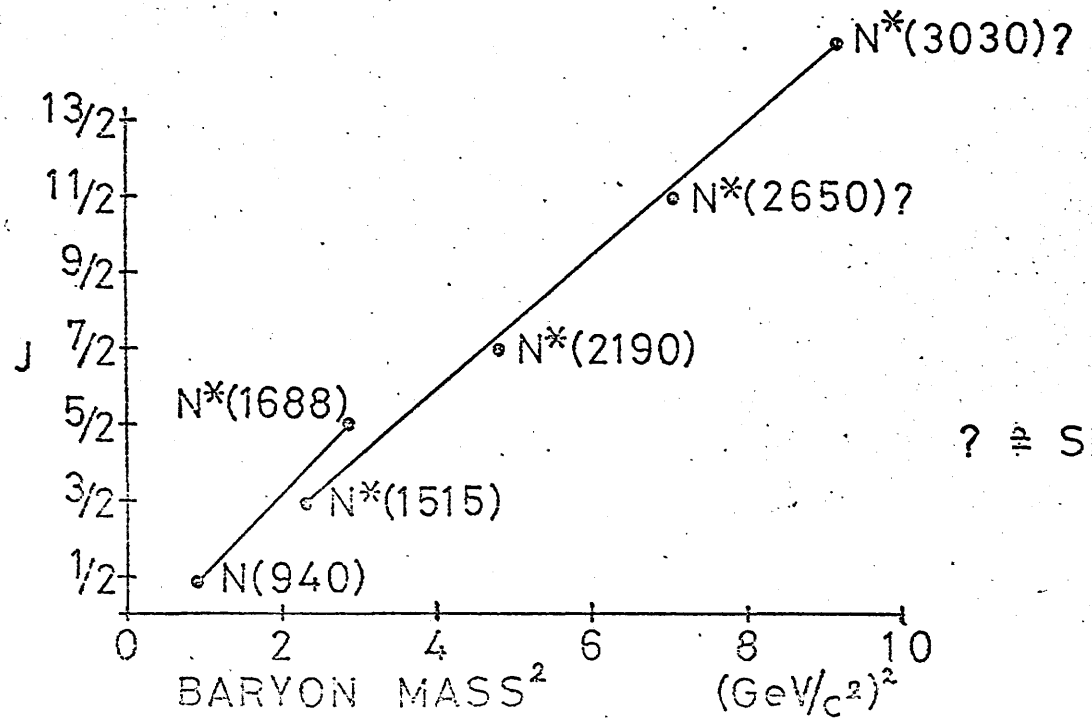

? ≙ SPIN UNCERTAIN

FIGURE 1.3

	I	I_3	Y	S	Q	
P	$1/2$	$1/2$	$1/3$	0	$2/3$	$J^P = 1/2^+$
n	$1/2$	$-1/2$	$1/3$	0	$-1/3$	
λ	0	0	$-2/3$	-1	$-1/3$	$B = 1/3$
$\bar{P}$	$1/2$	$-1/2$	$-1/3$	0	$-2/3$	$J^P = 1/2^-$
$\bar{n}$	$1/2$	$+1/2$	$-1/3$	0	$1/3$	
$\bar{\lambda}$	0	0	$2/3$	1	$1/3$	$B = -1/3$

Quark and Antiquark Properties

FIGURE 1.4

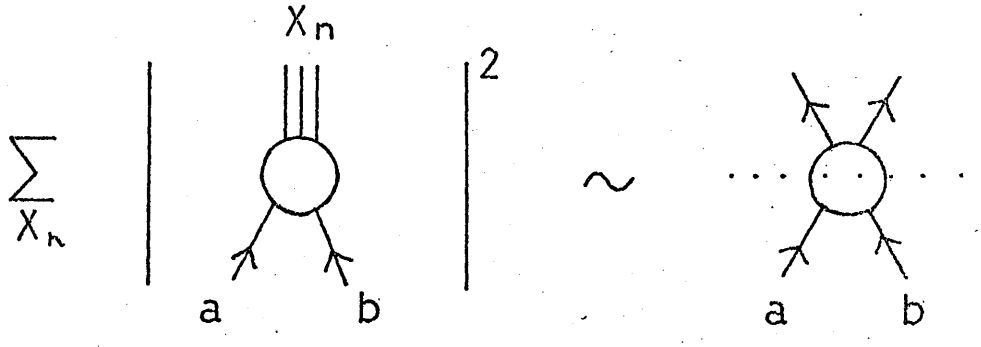

Optical Theorem

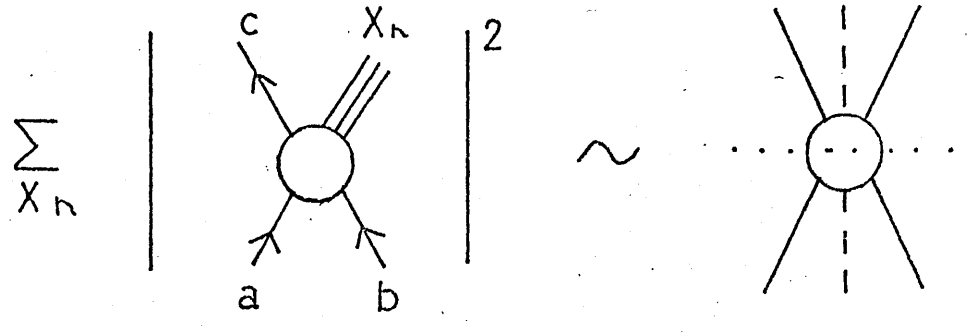

Mueller's Analogy for Inclusive Reactions

FIGURE 1.5

Chapter II

Film Measurement and Data Analysis

II.1 Introduction

The author joined the 10 GeV/c K^+p experiment in June 1969, by which time all the film had been taken. The beam design has been described in detail in previous theses (refs. 2.1, 2.2, 2.3, 2.4). 510,000 exposures were taken with the CERN 2m hydrogen bubble chamber, exposed to a radio frequency separated beam consisting of positive K-mesons at a momentum of 10 GeV/c. The film was taken in 5 separate runs between 1966 and 1968. Film from runs 1 and 3 was measured only for events with associated neutral decays: high proton contamination, due to trouble with the r.f. cavities, made this film unreliable for events without associated V's. Runs 2, 4, and 5 were measured for four prong events, and runs 4 and 5 only, for six prong events.

Runs 1, 2, and 3 film was divided amongst Birmingham, Glasgow, and Oxford film analysis groups, and runs 4 and 5 between Birmingham and Glasgow only.

II.2 Scanning of Film

Scanning was carried out for all primary interactions of the beam track. A restricted fiducial region 96cm long within the bubble chamber was used, and events with primary vertex outside this region were rejected. This was to ensure that high momentum secondary tracks from vertices lying near the top of the fiducial region could be measured for a sufficient length. Charged decays of neutral particles which could possibly be associated with a primary vertex

were accepted if they lay within the larger fiducial region 165cm long.

Each event was given a scanning code, ABC, where A represents the number of charged secondary tracks from the interaction vertex, B is the number of secondary charged tracks decaying (excluding π-μ- e decays), and C is the number of neutrals from the interaction vertex which have a visible decay within the fiducial region.

Cross-section calculations in a subsequent section of the chapter are based on data from 30 half-rolls of film which was scanned three times.

II.3 Measurement and Data Analysis

The author had special responsibility for the six prong events. All the film from runs 4 and 5 was measured in three views for six prong events, on the SMP machines. The output from the SMP programme was written on magnetic tape, which was then used as input for the R.H.E.L. system of programmes consisting of:

(i) GEOMETRY programme (ref. 2.5) for the reconstruction of events. The output from this programme consists of track half-length, reciprocal of momentum, tangent of dip, and azimuth for each measured track, and errors in these quantities. The vertex co-ordinates are also included in the GEOMETRY output tape.

(ii) KINEMATICS programme (ref. 2.6). Using the data from the GEOMETRY programme, KINEMATICS tests various hypotheses

against the experimental parameters for an event, making small adjustments to the measurements, within the experimental error, in order to minimise the χ^2- function:

$$\chi^2 = \sum_{i=1}^{N} \frac{(x_i - x_i^m)^2}{\sigma_i^2}$$

where N = number of measured track quantities

x_i is adjusted value of the measurement of the i'th track variable

x_i^M is the measured value of the i'th track variable

σ_i is the calculated error on the i'th track variable

A fit is attempted by varying the x_i^M at the vertex until energy and momentum are balanced for the hypothesis being tested. In the case of V^o events, the decay vertex is fitted first, followed by the interaction vertex, and finally an overall fit at both vertices is attempted. Fits having a χ^2-probability less than 1% were rejected. For every event, the KINEMATICS programme tries to fit each hypothesis which has the correct topology, for all possible particle-track combinations.

The six prong hypotheses which were attempted are listed in Table 2.1. The KINEMATICS processing time for events of this type is very high, typically, on the IBM 360/44 computer, around 40 seconds per event. This is because the number of particle-track combinations is high. For the $K^+p\pi^+\pi^+\pi^-\pi^-$ final state, for example, there are 12 different particle-track permutations, while the $K^+K^+K^-p\pi^+\pi^-$ final state involves 24 permutations. This high number of permutations,

coupled with the fairly high secondary track momentum possible at 10 GeV/c, even with six prong events, leads to a very high level of kinematic ambiguities.

7053 of the measured events contained at least one fit to one of the hypotheses: the number of fits to each hypothesis is summarised in Table 2.1. It can be seen that, on average, there are over four kinematic fits to each event.

The KINEMATICS programme, in addition to writing the output tape containing the results of the fitting, produces paper output containing a summary of each event, including the predicted ionisation for each track of each fit. The bubble density of a track varies with the velocity of the particle as $\frac{1}{\beta^2}$, where $\beta = \frac{v}{c}$. Since

$$v = \frac{p}{m} = \frac{p}{\sqrt{m_0^2 + p^2}}$$

the bubble density of a track of given momentum depends on the rest mass of the particle. The ionisation predicted by KINEMATICS can be compared with a visual estimate of the B.D. of tracks, and fits which predict the wrong bubble densities can then be rejected.

The level of kinematic ambiguities remaining after bubble density scanning was still high, particularly in the one-constraint fits with a missing neutral particle. Because of this, the one-constraint fits were not considered reliable for physics analysis. In 10 GeV/c K^+p interactions, the cross-section for production of three K-mesons is

approximately 30 times less than the cross-section for the same multiplicity reaction where only one K-meson is produced. For example:

$$\frac{\sigma^{--}(K^+p \longrightarrow K^+K^+K^-p)}{\sigma^{--}(K^+p \longrightarrow K^+\pi^+\pi^-p)} = 0.032 \qquad \text{(ref. 2.4)}$$

Since many of the 931 fits to the $K^+K^+K^-\pi^+\pi^-p$ reaction were ambiguous with fits to the $K^+\pi^+\pi^+\pi^-\pi^-p$ reaction, it was decided to reject fits to the former reaction in cases where such an ambiguity occurred.

To obtain an estimate of the processing efficiency of the measurement, geometrical reconstruction, and kinematic fitting a portion of the film was measured twice. The results from this indicated that the overall processing efficiency for the reaction:

$$K^+p \longrightarrow K^+\pi^+\pi^+\pi^-\pi^-p \qquad (1)$$

was 75%. 15% of the events were lost through failures in the geometrical reconstruction programme, and the remaining 10% loss was due to events of reaction (1) which were not fitted as such by the KINEMATICS programme. (This figure was obtained using the scanning efficiency formula in section II.5).

(iii) The final stage in the chain of post-measurement programmes is JUDGE (ref. 2.7). For fits which have survived the bubble density scanning stage, JUDGE converts the data on the KINEMATICS tape to a convenient form, and writes the output on a data summary tape (DST).

Events which contained more than one fit to a hypothesis after bubble density scanning were given a weight equal to the reciprocal of the total number of fits for that event, using the programme GUDDLE (ref. 2.4). The chain of programmes is shown in figure 2.1.

II.4 Analysis Programmes

The most frequently used analysis programme was SUMX (ref. 2.8). This programme reads the DST and calculates quantities of physical interest, in CHARM subroutines which can be written by the user. The output from SUMX consists of histograms, or of a 'MINIDST' containing selected event quantities.

The programme MINUIT (ref. 2.9) was used to obtain fits of various kinds to experimental data. Phase space distributions (used in Chapters III and IV) were provided by the programme FOWL (ref. 2.10).

II.5 Cross Section Calculations

In the work contained in Chapter V on single particle distributions, it was necessary to calculate cross-sections for each topology. Previous work to obtain the kaon track length for the 30 half-rolls of film used in the cross-section calculations (see ref. 2.4) indicated that using the total K^+p cross-section (which is known accurately from counter experiments) and relating this to the total number of events seen, gave an estimate for the kaon track length which was consistent with that obtained by other methods (beam count,

τ-decay count, and δ-ray momentum spectrum analysis). The total number of events is affected by beam contamination by pions and protons. However, information obtained when the film was being taken, and subsequently in the analysis of the elastic scattering data, shows that proton and pion contamination of the beam was less than 0.5% for Run 2, and less than this for Runs 4 and 5 (ref. 2.3). When the film was being taken, running with the r.f. off indicated that the contamination consisted mainly of non-interacting muons. Muon contamination does not affect the total number of events. The proton contamination was estimated from counter checks when the film was taken, and from running proton hypotheses on the elastic scattering events.

The topological cross-sections, for events with and without K^o production, were evaluated from the scanning data from the 30 half-rolls mentioned previously. Scanning efficiency is topology dependent. To correct for this as fully as possible, the number of events for each topology was corrected individually for scanning efficiency, using the formula:

$$N = (A + C)(B + C)/C$$

where A = number of events found only by scan 1

B = number of events found only by scan 2

C = number of events seen in both scans

N = total number of events

This assumes that the events found by the scanners are a

random sample of the total number of events.

The KINEMATICS programme was used to attempt to fit a K° at the decay vertex of each event noted as a V°. Events in which the neutral particle track obtained in this fit did not pass through the interaction vertex were rejected. For events where the neutral particle could be associated with the interaction vertex, a 3-constraint fit (with the momentum of the K° at the decay vertex the only unknown quantity) was attempted. Those events with missing mass inconsistent with the mass of the K° were rejected. Column 2 of table 2.2 contains the corrected numbers from column 1 indicated by the results of the decay vertex fits for the 30 half-rolls.

Events in which the projection of the neutral track length on the front glass window of the bubble chamber is less than .25 cm. were not used in the analysis, since such events could easily be misidentified. To compensate for this, and for the charged decays occurring outside the fiducial volume, each K° event was given a weight

$$\left[\exp\left(-\frac{L_{MIN}\,M}{TCp}\right) - \exp\left(-\frac{LM}{TCp}\right)\right]^{-1}$$

where $L_{MIN} = 0.25/\cos\lambda$

λ = dip of track

M = mass of K° (GeV/c^2)

p = momentum of K° (GeV/c)

T = mean lifetime of K

L = distance from production vertex to the edge of the fiducial volume along the K° line of flight direction.

The average weight was a function of topology, and these weights are listed here: (it was assumed that the weight for the 801 topology was the same as the 601 weight)

Topology	Weight
201	1.045
401	1.047
601	1.018
801	1.018

To take into account the invisible K^o decay modes,(2.11) another factor of 2.915 (ref. 2.12) was required. (For the 17 two prong events in which two K^o 's fitted, the square of these factors is appropriate). The probability of observing K^o's within the fiducial volume is summarised in table 2.3. Column 3 of table 2.2 contains the number of events corresponding to each topology after correcting for these factors. Finally, the cross-sections for each topology using the 10 GeV/c K^+p total cross-section figure of 17.3 mb ($\pm$.1mb) (ref. 2.13) is shown in column 4.

II.6 The Reaction $K^+p \rightarrow K^+p\pi^+\pi^+\pi^-\pi^-$.

The number of fits to the reaction

$$K^+p \rightarrow K^+p\pi^+\pi^+\pi^-\pi^- \qquad (1)$$

after bubble density scanning, was 1242, corresponding to 862 events. This represents a high level of ambiguities. The cause of these ambiguities was studied. The KINEMATICS programme line printer output revealed that, in a sample of 32 half-rolls of film, 40 events occurred where more than one fit to reaction (1) existed, after bubble density scanning. Of these 40 events, 30 of the ambiguities were caused by positive tracks (usually high momentum tracks) ambiguous

between a pion and a kaon. A scatter plot for the 27 events which had only one pion-kaon ambiguity, in which the laboratory momentum of the two ambiguous tracks are plotted against each other (figure 2.2) shows that such ambiguities occur most often in events where the two tracks have momenta which are similar in value. The single particle momentum spectra for the kaons and pions (Chapter V) are therefore unlikely to be distorted by ambiguities of this type. In the remaining ten ambiguous events of the sample, the ambiguities followed no pattern.

The probability distribution for the fits to reaction (1) showed a pronounced peak below a probabilty of 10%, although, above this value the distribution was reasonably flat. Events with probability below 10% were discarded.

II.7 Resonance Production

A previous attempt to study six-body final states in K^+p interactions (at 5 GeV/c) observed only $K^{*\circ}(890)$ and $\Delta^{++}(1236)$ production (ref. 2.14). The non-observation of higher mass resonances was explained by these authors as being caused by the high number of combinations of particles which can be grouped to form resonances. In the present experiment, at 10 GeV/c, $K^{*\circ}(890)$ and $\Delta^{++}(1236)$ are produced strongly. No statistically significant enhancements were seen in the mass plots corresponding to the decay of other resonances. The $I=\frac{1}{2}$ N^*'s studied in Chapter III in the reaction

$$K^+p \rightarrow K^+p\pi^+\pi^-$$

could not be individually resolved in reaction (1). The mass plot for the four $p\pi^+\pi^-$ combinations for each events (divided by four) is shown in figure 2.3. The hatched ditribution

corresponds to the $p\pi^+\pi^-$ combination with the lowest $\Delta^2(p/p\pi^+\pi^-)$, $(p\pi_1^+\pi_1^-$, say), with the additional constraint that $\Delta^2(p/p\pi_1^+\pi_1^-)$ is less than 0.5 $(GeV/c)^2$, and $M(K^+\pi_1^-)$ does not lie in the $K^{*0}(890)$ band $(0.84 < M(K^+\pi_1^-) < 0.94$ GeV/c^2). This selection should emphasise peripherally produced N^*'s . As can be seen from the hatched distribution, applying the Δ^2 selection produces a distribution which peaks in the 1.5-1.7 GeV/c^2 region, although statistics preclude further conclusions. The smooth curve in figure 2.2 represents phase space generated using the programme FOWL, with events weighted peripherally to reproduce the correct experimental $\Delta^2(p/p)$ and $\Delta^2(K^+/K^+)$ distributions. It can be seen that the higher mass region above about 2.4 GeV/c^2 is adequately described by this curve. Below 1.8 GeV/c^2 there is an excess of events in the experimental distribution, compared with the phase space curve.

A similar technique applied to the $K(n\pi)$ effective mass plots produced no noteworthy results.

The main interest in the analysis of the six prong events proved to be the single particle momentum distributions. These are discussed and compared with other data from other reactions in Chapter V.

II.8 The Reaction $K^+p \to K^0p\,\pi^+\pi^+\pi^+\pi^-\pi^-$.

The other four constraint channel with six charged tracks analysed by the author is the reaction

$$K^+p \to K^0p\,\pi^+\pi^+\pi^+\pi^-\pi^- \qquad (2)$$

with the K^0 decay visible within the chamber. Since there can be no ambiguities in this reaction between the kaon and any of the pions, the data is comparatively free from ambiguities.

203 fits to the reaction were obtained, corresponding to 194 events. (These figures include data from Runs 1, 2 and 3, which were measured for six prong V events, and also from the Birmingham measurements of Runs 4 and 5). However, the background due to the large number of combinations is higher than for reaction (1), since we have to deal with three positive pions.

$K^{*+}(890)$ and $\Delta^{++}(1236)$ are produced in this reaction but, as in reaction (1), there is no statistically convincing evidence for any higher mass resonance production. Data from reaction (2) is also used in Chapter V.

References

2.1 I.M^{c}Laren

Interactions of 10 GeV/c K^{+} Mesons with Protons

Ph.D. Thesis, Glasgow 1968

2.2 I.Griffiths

Inelastic Interactions of 10 GeV/c Positive Kaons with Protons

Ph.D. Thesis, Glasgow 1969

2.3 C.D.Procter

Elastic and Inelastic Interactions of Positive K Mesons with Protons at 10 GeV/c

Ph.D. Thesis, Glasgow 1970

2.4 I.R.White

10 GeV/c $K^{+}p$ Interactions

Ph.D. Thesis, Glasgow 1971

2.5 J.W.Burren and J.Sparrow

Geometrical Reconstruction of Bubble Chamber Tracks

R.H.E.L. NIRL/R/14

2.6 A.G.Wilson and E.C.Sedman

Programme KINEMATICS

N.I.R.N.S. (1963)

2.7 T.Noland

A Users Guide to the JUDGE programme

RHEL / M 136 (1967)

2.8 J.Zoll

The Programme SUMX

CERN Programme Library Y200

2.9 F.James and J.Roos

The Programme MINUIT

CERN Programme Library D506

2.10 F.James

A General Monte Carlo Phase Space Programme, FOWL

CERN Programme Library W505

2.11 This includes the uncharged decay mode $K^0 \rightarrow \pi^0\pi^0$ and the three body decay modes corresponding to K_L^0 decay, which are assumed to constitute 50% of the K^0 decays.

2.12 Reviews of Modern Physics

Vol. 43, No.2, Part II (1971)

2.13 W.Galbraith et al.

Physical Review 138B, 913 (1965)

2.14 W.De Baere et al.

Nuclear Physics B22, 131 (1970)

FINAL STATE	NUMBER OF FITS
$K^+ p \pi^+ \pi^+ \pi^- \pi^-$	1862
$K^+ p \pi^+ \pi^+ \pi^- \pi^- \pi^0$	16130
$K^+ \pi^+ \pi^+ \pi^+ \pi^- \pi^- n$	5322
$p \pi^+ \pi^+ \pi^+ \pi^- \pi^- (K^0)$	5102
$K^+ K^+ K^- p \pi^+ \pi^-$	931
$K^0 p \pi^+ \pi^+ \pi^+ \pi^- \pi^-$	108
$K^0 p \pi^+ \pi^+ \pi^+ \pi^- \pi^- \pi^0$	385
$K^0 n \pi^+ \pi^+ \pi^+ \pi^+ \pi^- \pi^-$	70
TOTAL FITS	29910
CORRESPONDING NUMBER OF EVENTS	7053

Fits to six prong hypotheses before bubble-density scanning.

TABLE 2.1

Topology(1)	Events(2)	Events(3)	Events(4)	Cross-section(5) (mb.)
200	5391	6063	4599	5.50($\pm$0.11)
201	1286	753	2076	2.48($\pm$0.11)
202	156	17	158	0.19($\pm$0.05)
400	4705	5221	3926	4.70($\pm$0.18)
401	1147	631	1926	2.31($\pm$0.11)
600	1346	1452	1212	1.45($\pm$0.09)
601	235	129	369	0.44($\pm$0.04)
800	163	172	152	0.18($\pm$0.02)
801	19	10	30	0.04($\pm$0.01)
Total	14448	14448	14448	17.3 ($\pm$0.1)

TABLE 2.2

TOPOLOGICAL CROSS-SECTIONS AT 10 GeV/c (from scanning information from 30 half-rolls film.

NOTES : (1) Events with charged decays are included, e.g. '210' is included in '200' total.

(2) These figures are corrected for scanning efficiency.

(3) These figures are corrected for decay vertices which do not fit a K^0 hypothesis.

(4) Corrected for unseen decays of K^0 (including K^0_L and uncharged decays, and decays outside the fiducial volume), assuming 50 % K^0_L - 50 % K^0_S

(5) The cross-section for 'V' events includes all K^0 's.

ACTUAL TOPOLOGY	Observed topology								
	200	201	202	400	401	600	601	800	801
201	0.672	0.328	-	-	-	-	-	-	-
202	0.451	0.441	0.108	-	-	-	-	-	-
401	-	-	-	0.672	0.328	-	-	-	-
601	-	-	-	-	-	0.663	0.337	-	-
801	-	-	-	-	-	-	-	0.663	0.337

Probability of observing K^0 decays events as a given topology.

Table 2.3

Figure Captions

2.1 Data processing system

2.2 Scatter plot of π^+ momentum against K^+ momentum, for $K^+p\pi^+\pi^+\pi^-\pi^-$ final state fits involving a pion-kaon ambiguity.

2.3 $p\pi^+\pi^-$ effective mass distribution from $K^+p\pi^+\pi^+\pi^-\pi^-$ final state. There are four combinations of $p\pi^+\pi^-$ per event, and the tctal number of entries in each bin is shown divided by four. The smooth curve shows the prediction of weighted phase space. The hatched distribution shows the $p\pi_1^+\pi_1^-$ effective mass, where $p\pi_1^+\pi_1^-$ is the combination with the lowest $\Delta^2(p/p\pi^+\pi^-)$ In addition, events for which $\Delta^2(p/p\pi_1^+\pi_1^-) > 0.5$ $(GeV/c)^2$ or for which $0.84 < M(K^+\pi_1^-) < 0.94$ GeV/c^2, are excluded.

DATA PROCESSING SYSTEM

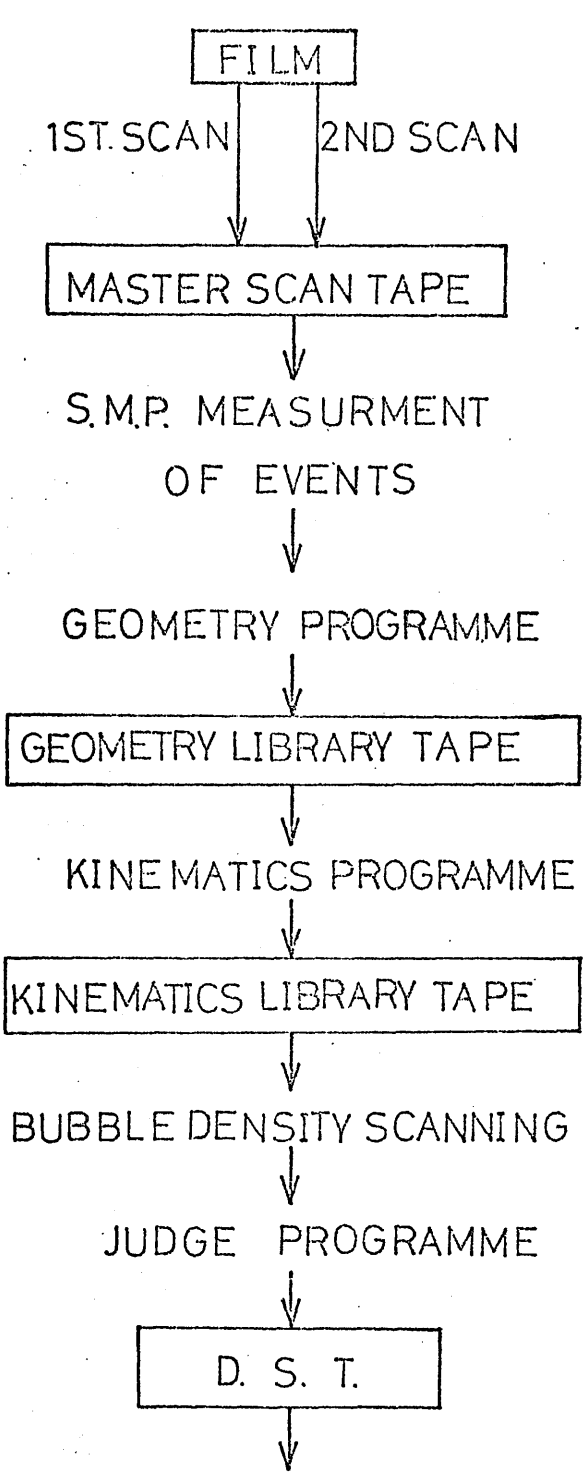

FIGURE 2.1

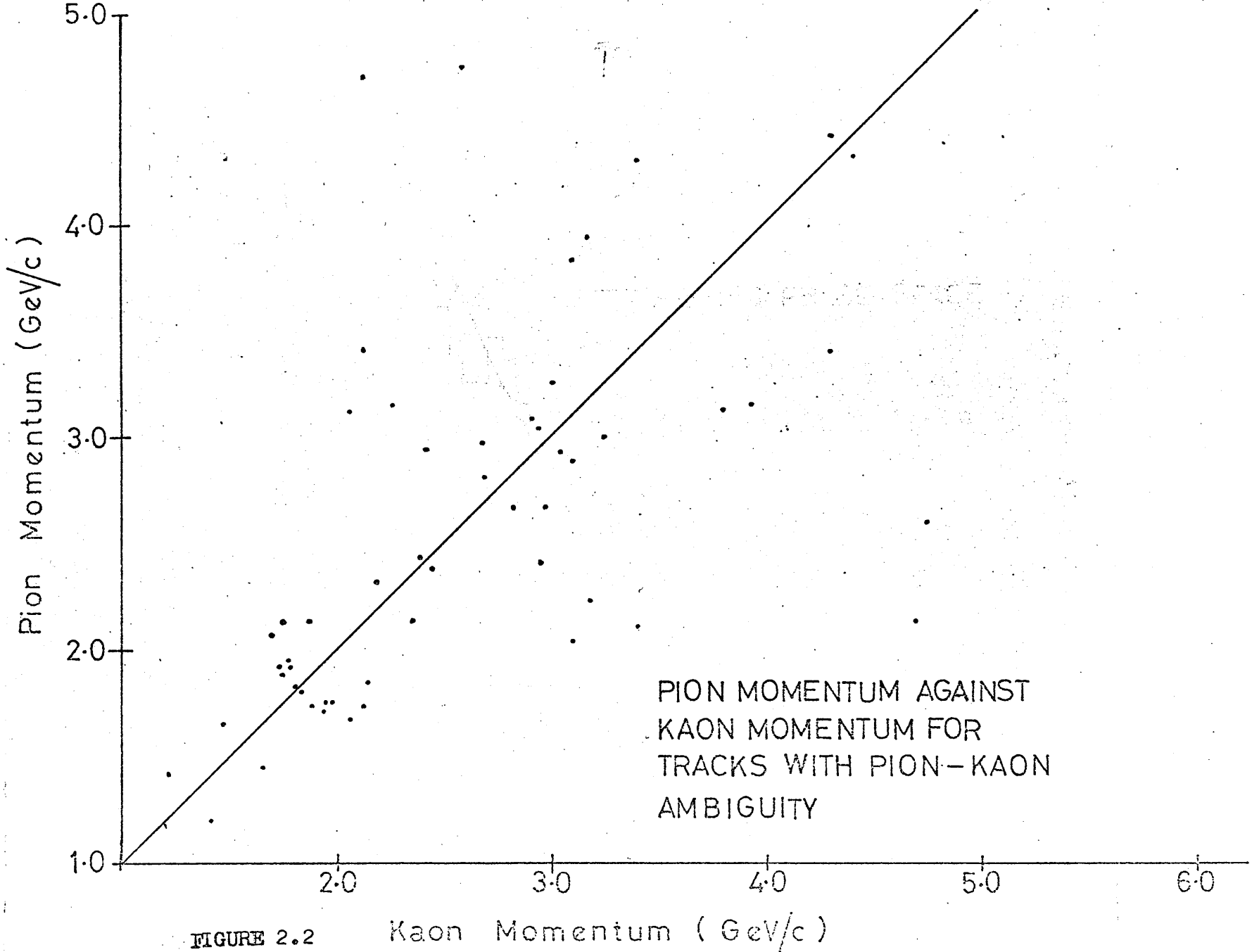
5·0
4·0
3·0
2·0
1·0
Pion Momentum (GeV/c)
2·0
3·0
4·0
5·0
6·0
Kaon Momentum (GeV/c)
PION MOMENTUM AGAINST
KAON MOMENTUM FOR
TRACKS WITH PION–KAON
AMBIGUITY

FIGURE 2.2

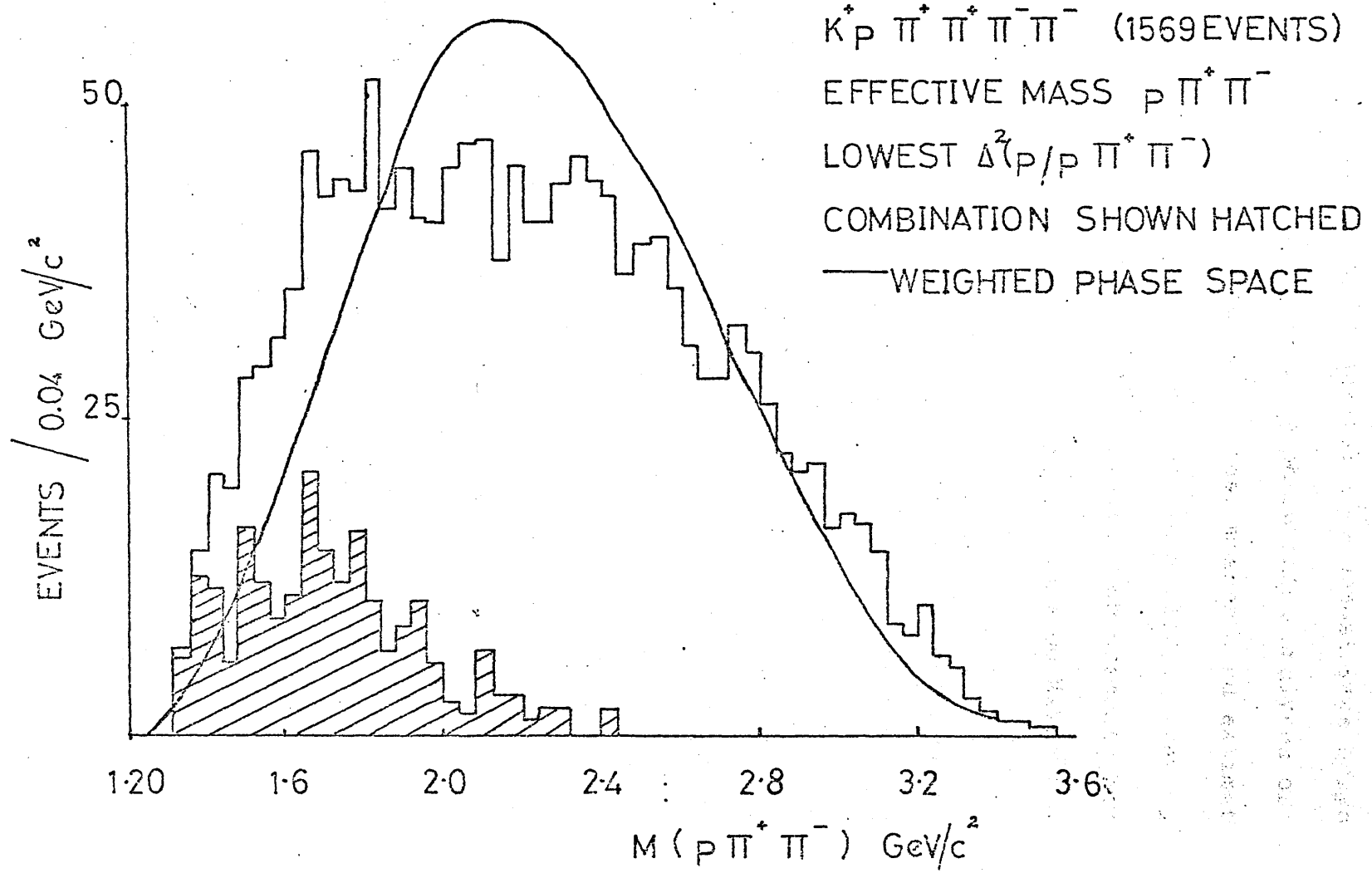
$K^+p\ \pi^+\pi^+\pi^-\pi^-$ (1569 EVENTS)
EFFECTIVE MASS $p\pi^+\pi^-$
LOWEST $\Delta^2(p/p\pi^+\pi^-)$
COMBINATION SHOWN HATCHED
WEIGHTED PHASE SPACE
50
25
EVENTS / 0.04 GeV/c²
1·20
1·6
2·0
2·4
2·8
3·2
3·6
M ($p\pi^+\pi^-$) GeV/c²

FIGURE 2.3

Chapter III

Study of the $I = \frac{1}{2}$ $p\pi\pi$ System in 10 GeV/c K^+p Interactions

III.1 Introduction

Evidence for several $I = \frac{1}{2}$ non-strange baryon resonances has been obtained from phase shift analyses of pion-proton scattering data. The spins, masses, and estimated widths of these resonances are shown in Table 3.1 (ref. 3.1).

In production experiments, enhancements have been observed around 1500 MeV/c^2, and 1700 MeV/c^2. Some experiments have identified the enhancement in the 1500 MeV/c^2 region with the $\frac{1}{2}^+$ Roper resonance, although unique identification of the enhancements as either the $N^*(1470)$ Roper resonance (ref.3.2), or the $3/2^-$ $N^*(1520)$ from mass distributions alone, is difficult. The published experimental data relies mainly on πN and NN interactions where separation of the leading particles from the other final state particles complicates the analysis. More information on the Roper resonance production, and its branching ratios, would be of considerable interest. The branching ratios of the $N^*(1700)$ have aroused interest, with various production experiments giving values for the branching ratio:

$$N^*(1700) \longrightarrow \Delta(1236)\pi / p\pi\pi$$

ranging between 0 and 75% (ref. 3.3). Results from some of these production experiments are summarised in Table 3.2.

Recently, speculation on the nature of the $I = 1/2$ N^* resonances produced in reactions where diffraction

dissociation is possible e.g.

$$\pi^{\pm} p \longrightarrow \pi^{\pm} N^{*}$$

has raised the possibility that the resonances produced in diffraction dissociation processes may not be the same as those seen in phase shift analyses (ref. 3.4), and it has been suggested that the $N^{*}(1700)$ of production experiments may be formed in a dissociation process involving the $N^{*}(1470)$ Roper resonance, and a pion. (See figure 3.1).

We have carried out a study of the low mass peripherally produced $p\pi\pi$ system produced in 4 body final states from the reaction:

$$K^{+}p \longrightarrow K^{+}p\pi^{+}\pi^{-} \qquad (1)$$

In the Birmingham-Glasgow-Oxford 10 GeV/c experiment, there are 14,265 events with at least one fit to this reaction. (The total number of fits to the reaction is 16,229). Most of the following analysis is restricted to those events which have the effective mass of the $p\pi^{+}\pi^{-}$ system below 1.75 GeV/c , and the four-momentum-transfer-squared from the target to the $p\pi^{+}\pi^{-}$ system below 0.5$(GeV/c)^{2}$. The level of kinematic ambiguities for such events is less than 1.5%. Peripheral $p\pi^{+}\pi^{-}$ production corresponds to low laboratory momentum tracks which can be fitted more easily by the programme KINEMATICS (ref. 2.6), and also can be identified at the bubble density scanning stage.

III.2 <u>I-Spin of $p\pi^{+}\pi^{-}$ System</u>

The effective mass distribution of the $p\pi^{+}\pi^{-}$ system, which is a mixture of $I = 1/2$ and $I = 3/2$ states, from reaction

(1) is shown in figure 3.2. Applying a cut on $\Delta^2(p/p\pi^+\pi^-)$ at 0.5 $(GeV/c)^2$ gives the hatched distribution. An enhancement around 1.7 GeV/c^2 is prominent, with another less pronounced peak at 1.5 GeV/c^2. The reaction:

$$K^+p \longrightarrow K^\circ p\,\pi^+\pi^\circ \qquad (2)$$

where the $p\,\pi^+\pi^\circ$ system produced is pure $I=3/2$, exhibits no low mass enhancements in the $p\,\pi^+\pi^\circ$ effective mass plot (shown in figure 3.3, with the hatched distribution corresponding to events with $\Delta^2(p/p\,\pi^+\pi^\circ) < 0.5\ (GeV/c)^2$).

To obtain a very rough estimate of the $I=3/2$ contribution to the $p\,\pi^+\pi^-$ mass spectrum, one can assume that the $I=3/2$ $p\,\pi^+\pi^-$ system decays via $\Delta(1236)\pi$ only. (For the low mass $p\,\pi^+\pi^-$ system below about 1.8 GeV/c^2, most of the events have $p\pi^+$ mass lying in the $\Delta(1236)$ band. Since phase space is restricted at this $p\pi^+\pi^-$ mass, an accurate determination of the branching ratio via $\Delta(1236)\pi$ is difficult.) The ratio of $K^\circ p\,\pi^+\pi^\circ$ to $K^+p\pi^+\pi^-$ for the $I=3/2$ state for the sequential processes shown in figure 3.4, evaluated from the I-spin Clebsch-Gordan coefficients, is 9/2. Taking the number of events with $p\pi\pi$ mass below 1.8 GeV/c^2 from reactions (1) and (2), and correcting for the unseen K°'s from reaction (2), and for the different subsamples of film from which data for reactions (1) and (2) was obtained, gives an estimate of 6% ($\pm$ 2%) for the $I=3/2$ contribution to the $p\,\pi^+\pi^-$ system from reaction (1) below 1.8 GeV/c^2.

The remainder of the analysis will be concerned with the

$p\pi^+\pi^-$ system formed in reaction (1). Only events with $\Delta^2(p/p\pi^+\pi^-) < 0.5$ $(GeV/c)^2$ will be considered, and the $p\pi^+\pi^-$ system will be taken to be $I=1/2$ in the Dalitz Plot analysis.

III.3 Four-Momentum-Transfer-Squared Distribution

The four-momentum-transfer-squared distribution from the target proton to the $p\pi^+\pi^-$ low mass system for the events of reaction (1) is sharply peaked. Figure 3.5 shows exponential fits of the form $Ae^{-b|t|}$ to the Δ^2-distribution below 0.4 $(GeV/c)^2$. The slope of the Δ^2-distributions shows that the low mass $p\pi^+\pi^-$ system is produced peripherally, with the sharpness of the peak decreasing with increasing mass. These Δ^2-distributions are consistent with diffractive production, where spin-parities $1/2^+$, $3/2^-$, and $5/2^+$ etc. are expected to dominate (ref. 3.5). The diagrammatic representation of the process is shown in figure 3.6.

III.4 Angular Distributions

The Berman-Jacob angular distributions can give (ref 3.6) information on the spin of the three body $p\pi^+\pi^-$ system, and also on the spin of the exchanged particle, using the normal to the $p\pi^+\pi^-$ decay plane as analyser (see figure 3.7). The z-axis is taken along the target proton direction in the $p\pi^+\pi^-$ centre of mass, and the y-axis is the normal to the production plane. The angular distributions for the normal can be written as:

$$\sum_{m,l} G_{m,l}\ Y_l^{m*}(\theta,\phi)$$

where the maximum value of $l = 2j$ and j is the spin of the $p\pi^+\pi^-$ system. Moments of the spherical harmonics, normalised to $\langle Y_0^0 \rangle = W_0^0 = 1$, were evaluated across the (θ, ϕ) distributions, for 100 MeV/c^2 wide intervals across the $p\pi^+\pi^-$ mass spectrum. Events with $K^+\pi^-$ effective mass lying in the $K^*(890)$ band ($0.84 < M(K^+\pi^-) < 0.94$ GeV/c^2) were omitted. (This $K^+\pi^-$ effective mass cut is discussed later).

$$W_l^m = \frac{1}{W_0^0} \sum_{i=1}^{N} Y_l^m(\theta_i, \phi_i)$$

The error estimate on the moments (ref. 3.6) is:

$$\delta W = \sqrt{\frac{\overline{W^2} - \overline{W}^2}{N}}$$

where N is the number of events. None of the moments W_l^m for $m \neq 0$, had values significantly different from zero, which is consistent with a spinless exchange particle in figure 3.6.

The moments of spherical harmonics with $m = 0$ are shown in figure 3.8. Y_2^0 has significantly negative values throughout the distribution, suggesting the presence of spin 3/2 contributions even at the lowest $p\pi^+\pi^-$ mass region 1.35 - 1.45 GeV/c^2. Y_4^0 increases from 1.55 GeV/c^2, becoming significant above 1.65 GeV/c^2, where spin 5/2 or higher is indicated. Y_6^0 is small in all mass regions below 1.85 GeV/c^2 and there is little evidence for a spin of 7/2 contribution below this mass. None of the odd moments show significant deviations from zero. This suggests that the $p\pi^+\pi^-$ system we are studying is predominately of either natural or unnatural spin parity, but not a mixture.

III.5 Branching Ratios of $p\pi^+\pi^-$ Systems

Previous attempts to evaluate the branching ratios of the $p\pi^+\pi^-$ enhancement at 1700 MeV/c^2 in production experiments have assumed dominant decays via $\Delta(1236)\pi$ and $p\pi\pi$. The suggestion that the production of the 1700 MeV/c^2 peak is associated in some way with the $N^*(1470)$ Roper resonance, may also imply that the $N^*(1700)$ can decay via $N^*(1470)$ To investigate this, we have assumed possible decays via $N^*(1470)\pi$ and $\Delta(1236)\pi$, as well as three body decay. Inspection of the Dalitz plot for the 1700 to 1750 MeV/c^2 $p\pi^+\pi^-$ mass region shows that the $\Delta(1236)\pi$ and $N^*(1470)\pi$ bands overlap considerably, and so simple background subtraction techniques cannot be used to estimate the branching ratios. A Dalitz plot analysis is required.

An indication that the branching ratio via $\Delta^{++}(1236)\pi^-$ in the 1700 MeV/c^2 enhancement is lower than the percentage of $\Delta^{++}(1236)$ formed from the $p\pi^+\pi^-$ background can be obtained from figure 3.9. In this figure, the percentage of events with $p\pi^+$ mass in the $\Delta(1236)$ band (1.16 to 1.28 GeV/c^2) is shown for 100 MeV/c^2 wide intervals across the $p\pi^+\pi^-$ mass spectrum. This percentage apparently falls off almost linearly as the $p\pi^+\pi^-$ mass and the available $p\pi^+$ phase space are increased. However, around 1600 to 1750 MeV/c^2 there is an indication of a dip in the percentage of events lying in the $\Delta^{++}(1236)$ band.

A Dalitz plot and decay angular distribution analysis, based on a model suggested by Bowler (ref. 3.7), has been carried out by the author, with a view to investigating the branching ratios and spin of the $p\pi^+\pi^-$ system.

III.6 Model Dependent Decay Angle and Dalitz Plot Distribution Analysis

Section III.4 above suggests that the production angular distributions of the $p\pi^+\pi^-$ system are consistent with spin zero exchange. We assume that spin zero exchange is in fact the dominant mechanism, and that the $p\pi^+\pi^-$ system is $I = 1/2$ and has J^P = values $1/2^+$, $3/2^-$ and $5/2^+$ only (see sections III.3 and III.4). For each of these spin-parity assignments, and for a target proton helicity λ, say, transition amplitudes for the decay of the three body $p\pi\pi\pi$ system via two body resonance decay schemes can be formulated. The total amplitude for each target proton helicity, and final proton spin projection, can be written as a sum of such individual amplitudes with relative phase factors and coefficients as free parameters. The final expression for the angular and Dalitz plot distributions is then obtained by averaging the squared modulus of each total amplitude over the initial proton helicity states, and summing over the final proton spin projections. The parameters contained in this expression are varied until the best agreement between the desired distribution and the experimental distribution is obtained.

The main two body decay of the $p\pi^+\pi^-$ system considered is via $\Delta(1236)\pi$, with the relative amounts of $\Delta^{++}(1236)$ and $\Delta^{0}(1236)$ determined by I-spin. An incoherent three body phase space decay is included. In the highest mass region, 1.7 - 1.75 GeV/c^2, an additional term for decay via $N^*(1470)\pi^+$ is allowed.

The coordinate system employed in the analysis is shown in figure 3.10. In the $p\pi^+\pi^-$ centre-of-mass system, the z-axis is chosen along the target proton direction, so that the initial helicity of the target proton in the $p\pi^+\pi^-$ centre-of-mass is the z-component of spin of the $p\pi^+\pi^-$ system formed (assuming spin zero exchange). (See ref 3.8). The y-axis is taken as $\underset{\sim}{p}_{IN} \times \underset{\sim}{p}_{OUT}$, where $\underset{\sim}{p}_{IN}$ and $\underset{\sim}{p}_{OUT}$ are the incoming and outgoing proton directions. The coordinate system used in the two body centre-of-mass systems to describe the two body resonance decays are chosen parallel to the three body centre-of-mass axes. All vectors in the two body centre-of-mass are obtained by a Lorentz transformation direct from the $p\pi^+\pi^-$ centre-of-mass system (ref. 3.9). The amplitude terms, and intensity expression, are included in the Appendix. A maximum likelihood fit was carried out. Due to the complicated transition amplitudes and coordinate system in use, the normalisation terms in the likelihood function were obtained by Monte Carlo integration over phase space, using the programme FOWL (ref. 2.10). Details of the fitting procedure are also included in the Appendix.

It was found that $K^{*o}(890)$ production contributes a spike to the angular distributions which cannot be fitted using this model. All events with $0.84 < M(K^+\pi^-) < 0.94$ GeV/c^2 were, therefore, excluded from the analysis. This removes most of this spike, although a small narrow forward peak can still be seen in some of the angular distributions. This may be due to the effect of resonant production of $K^*(1420)$. Such effects are small and we have not imposed further cuts to exclude $K^*(1420)$ events. Figures 3.11 - 3.17 are the fits to the angular and effective mass distributions. The distributions vary with increasing $p\pi^+\pi^-$ effective mass, and are closely followed by the fits. In all the $p\pi^+\pi^-$ mass regions, the data was fitted well using only $\Delta(1236)\pi$ and three body phase space decays. The relative contributions of $1/2^+$, $3/2^-$, and $5/2^+$ $p\pi\pi$ systems decaying via $\Delta(1236)\pi$ and also of three body non-resonant decay of the $p\pi\pi\pi$ system, are shown in figure 3.18 normalised to the total number of events in each $p\pi^+\pi^-$ mass region.

There are no rapid fluctuations in these contributions from one $p\pi^+\pi^-$ mass interval to the next. $3/2^-$ seems to dominate at low $p\pi^+\pi^-$ masses (below 1.55 GeV/c^2), while $5/2^+$ dominates the high mass regions. We see no evidence for $1/2^+$ in the lower mass region, and do not therefore interpret the 1500 MeV/c^2 enhancement in the $p\pi^+\pi^-$ plot as the Roper resonance. The large $5/2^+$ contribution in the upper region suggests that the $p\pi^+\pi^-$ enhancement at 1700 MeV/c^2 observed in our data can be identified with the $N^*(1688)$, $J^P = 5/2^+$, seen

in phase shift analysis. The comparatively large amount of non-resonant three body decay in the 1650 - 1750 MeV/c^2 $p\pi^+\pi^-$ mass region confirms the conclusion reached in section 5 that the branching ratio of the 1700 MeV/c^2 enhancement via $\Delta(1236)\pi$ is lower than the background $p\pi^+\pi^-$ branching ratio via $\Delta(1236)\pi$.

The fits to the $p\pi^+$ and $p\pi^-$ mass spectrum in the 1700 MeV/c^2 $p\pi\pi^-$ region using decays via $\Delta(1236)\pi$ and phase space only, reproduce the features of the data well, without the inclusion of $N^*(1470)\pi^+$ decay terms. When these terms are included, no improvement in the likelihood function is obtained, and the highest likelihood corresponds to a negligible amount of $N^*(1470)\pi^+$.

III.7 Conclusions

The $p\pi^+\pi^-$ system from the reaction:

$$K^+p \longrightarrow K^+p\pi^+\pi^-$$

shows enhancements at 1.5 GeV/c^2 and 1.7 GeV/c^2. These are absent in the reaction

$$K^+p \longrightarrow K^0p\pi^+\pi^0$$

and we therefore assume that they are $I=\frac{1}{2}$ structures.

By considering the angular distributions of the normal to the $p\pi^+\pi^-$ decay plane, and also from a model-dependent analysis of the Dalitz Plot and decay angular distributions, we conclude that the $p\pi^+\pi^-$ region below 1.5 GeV/c^2 is predominantly $J^P = 3/2^-$ while above 1.6 GeV/c^2 $J^P = 5/2^+$ is dominant. We see no evidence for the 1500 MeV/c^2

enhancement in our data being the Roper resonance, and no evidence that the $N^*(1700)$ decays via the Roper resonance. If $\frac{1}{2}^+$ states do occur, they do not decay predominantly through $\Delta(1236)\pi$.

If we take the number of events corresponding to the decay of the $5/2^+$ system via $\Delta(1236)\pi$ relative to the non-resonant decay, we find a branching ratio of 50% for decay via $\Delta(1236)\pi$.

References

3.1 Particle Data Group

Reviews of Modern Physics 43 (1971)S1

3.2 L.D. Roper et al.

Physical Review 138B,190 (1965)

3.3 V.Alles-Borelli et al.

Nuovo Cimento 47, 232 (1967)

G.Alexander et al.

Physical Review 154(2),1285 (1967)

Y.Y.Lee et al.

Physical Review 159(2),1156 (1967)

S.P.Almeida et al.

Physical Review 174,1638 (1968)

J.I.Rhode et al.

Physical Review 187,1844 (1969)

V.E.Barnes et al.

Physical Review Letters 23,1516 (1969)

R.B.Willman et al.

Physical Review Letters 24,1260 (1970)

3.4 D.R.O.Morrison

International Conference on High Energy Physics,

Kiev 1970

3.5 D.R.O.Morrison et al.

Physical Review 165, 1699 (1968)

3.6 S.M.Berman and M.Jacob

Physical Review 165,1699 (1968)

3.7 Birmingham-Glasgow-Oxford collaboration

International Conference on High Energy Physics

Kiev 1970

Session 5b, Paper 5

3.8 B.T.Feld

Models of Elementary Particles

Blaisdell Publishing Company,1969

3.9 W.Koch

Proceedings of the 1964 Easter School for Physicists

Herceg Novi 1964

CERN 64-13 Volume II

3.10 J.D.Jackson

Nuovo Cimento 34,1644 (1964)

3.11 S.Glashow and A.Rosenfeld

Physical Review Letters 10,192 (1963)

3.12 E.W. Anderson et al.

Physical Review Letters 16,855 (1966)

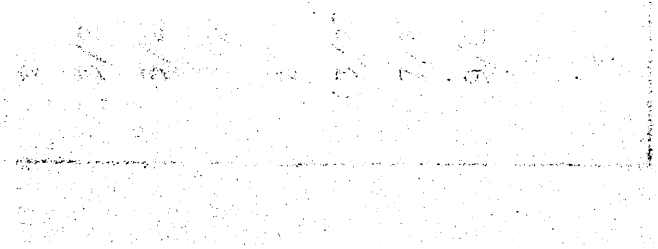

Table 3.1

$I = \frac{1}{2}$ S = 0 Baryons from phase-shift analysis

Natural Spin-Parity				Unnatural Spin-Parity			
J^P	Mass	Γ	SU_3 Status	J^P	Mass	Γ	SU_3 Status
$\frac{1}{2}^+$	1470	260	Bad	$\frac{1}{2}^-$	1535	80	Fair
$3/2^-$	1520	115	Good	$5/2^-$	1670	145	Good
$5/2^+$	1688	125	Fair	$\frac{1}{2}^-$	1700	280	Bad
$(3/2^-$	1730	?)	-	$(3/2^+$	1860	355)	-
$\frac{1}{2}^+$	1780	405	-				
$(3/2^-$	2030	290)	-				
$7/2^-$	2190	300	-				
$9/2^+$	2220	300	-				
?	2650	360	-				
?	3030	400	-				

SU_3 Status : Good = 2 other members of octet known
Fair = 1 " " " " "
Bad = 0 " " " " "

Table 3.2

$N^*(1700)$ branching ratios from other production experiments

Experiment	Main Branching Ratios	Method of Determination of Branching Ratios
$\bar{p}p$ 5.7 GeV/c (A. Borelli)	No evidence for $\Delta^{++}\pi^-$ decay	Obtained by comparing $p\pi^+$ and $p\pi^-$ mass spectra.
pp 5.5 GeV/c (Alexander)	67% decay via $\Delta^{++}\pi^-$	Obtained by fitting 1-D $p\pi^+$ mass plot.
π^-p 3.6 GeV/c (Lee)	Evidence for some $\Delta\pi$ decay	Comparison of $p\pi^-$ mass spectra gives 9:1 ratio for 1238 bump as expected from I-spin.
pp 10 GeV/c (Almeida)	31% via $\Delta^{++}\pi^-$	Background in $p\pi^+$ plot given by O.P.E. model, events above background in $p\pi^+$ plot give $\Delta^{++}\pi^-$ production.
pp 22 GeV/c (Jespersen)	Dominant Δ^{++} decay	1-D $p\pi^+$ mass plot fitted. Also Δ^{++} selection does not reduce $N^*(1700)$ peak appreciably.
K^-p 7.3 GeV/c (Barnes)	No decay via Δ^{++}	Dalitz plot fit. $\Delta\pi$ +phase space.
π^+p 13.1 GeV/c (Willmann)	75% decay via Δ^{++}	Dalitz plot fit. $\Delta\pi$ + phase space

Figure Captions

3.1 Diffraction Dissociation diagram for production of $N^*(1700)$

3.2 } Effective mass $p\pi^+\pi^-$ from reactions $K^+p \to K^+p\pi^+\pi^-$, and $K^+p \to K^0p\pi^+\pi^0$.

3.3 } The hatched distribution shows events with $\Delta^2(p/p\pi^+\pi^-) < 0.5$ $(GeV/c)^2$

3.4 I-spin Clebsch-Gordan coefficients for $I = 3/2$ $N\pi\pi$ production in K^+p interactions

3.5 Exponential fits to $\Delta^2(p/p\pi^+\pi^-)$ distributions for four $p\pi^+\pi^-$ mass intervals

3.6 Diagrammatic representation of peripheral $p\pi^+\pi^-$ production in $K^+p\pi^+\pi^-$ final state

3.7 Co-ordinate system defining Berman-Jacob θ and ϕ angles

3.8 Moments of spherical harmonics across the Berman-Jacob θ and ϕ angular distributions, for six $p\pi^+\pi^-$ mass intervals.

3.9 Percentage of events with $1.16 < M(p\pi^+) < 1.28$ GeV/c for $p\pi^+\pi^-$ mass intervals 50 MeV/c^2 wide.

3.10 Co-ordinate system used in Dalitz plot and angular distribution analysis of $p\pi^+\pi^-$ system

3.11 - 3.17 For seven 50 MeV/c wide $p\pi^+\pi^-$ mass intervals:
(Top and centre) Fits to the azimuth angles of figure 3.11 for the $p\pi$ (left) and $p\pi$ (right) two body systems.
(Bottom) Fits to the $p\pi$, $p\pi$ and $\pi^+\pi^-$ effective mass spectra.

3.18 Number of events with $J^P = 5/2^+$, $3/2^-$ and $1/2^+$ decaying via $\Delta(1236)\pi$, and (bottom) via three body phase space, for the $p\pi\pi$ mass intervals of figures 3.11 - 3.17

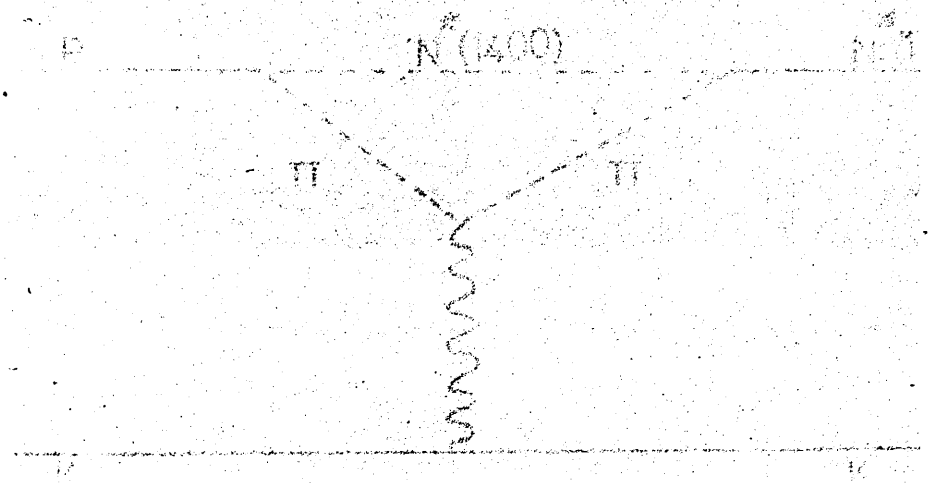

DIFFRACTION DISSOCIATION DIAGRAM
FOR PRODUCTION OF N*(1700)

FIGURE 3.J

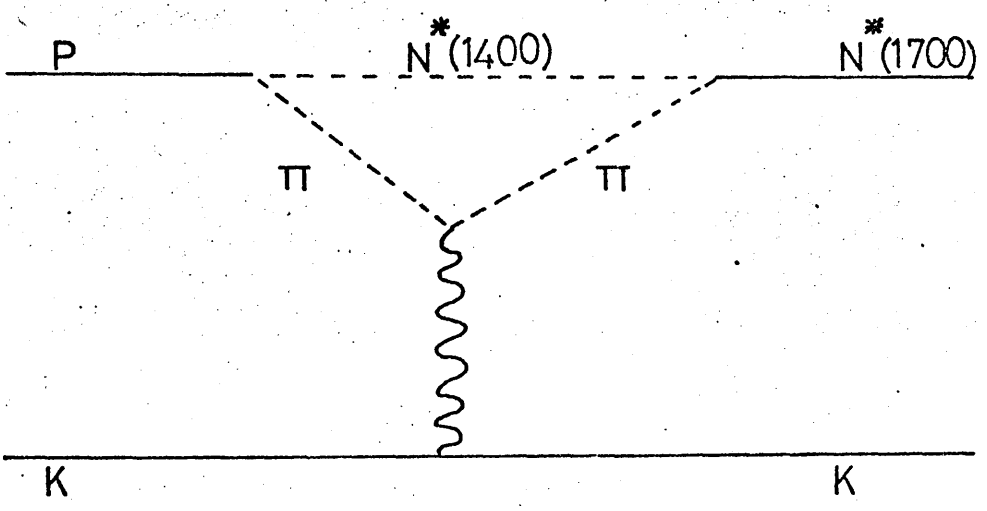

DIFFRACTION DISSOCIATION DIAGRAM FOR PRODUCTION OF $N^{*}(1700)$

FIGURE 3.1

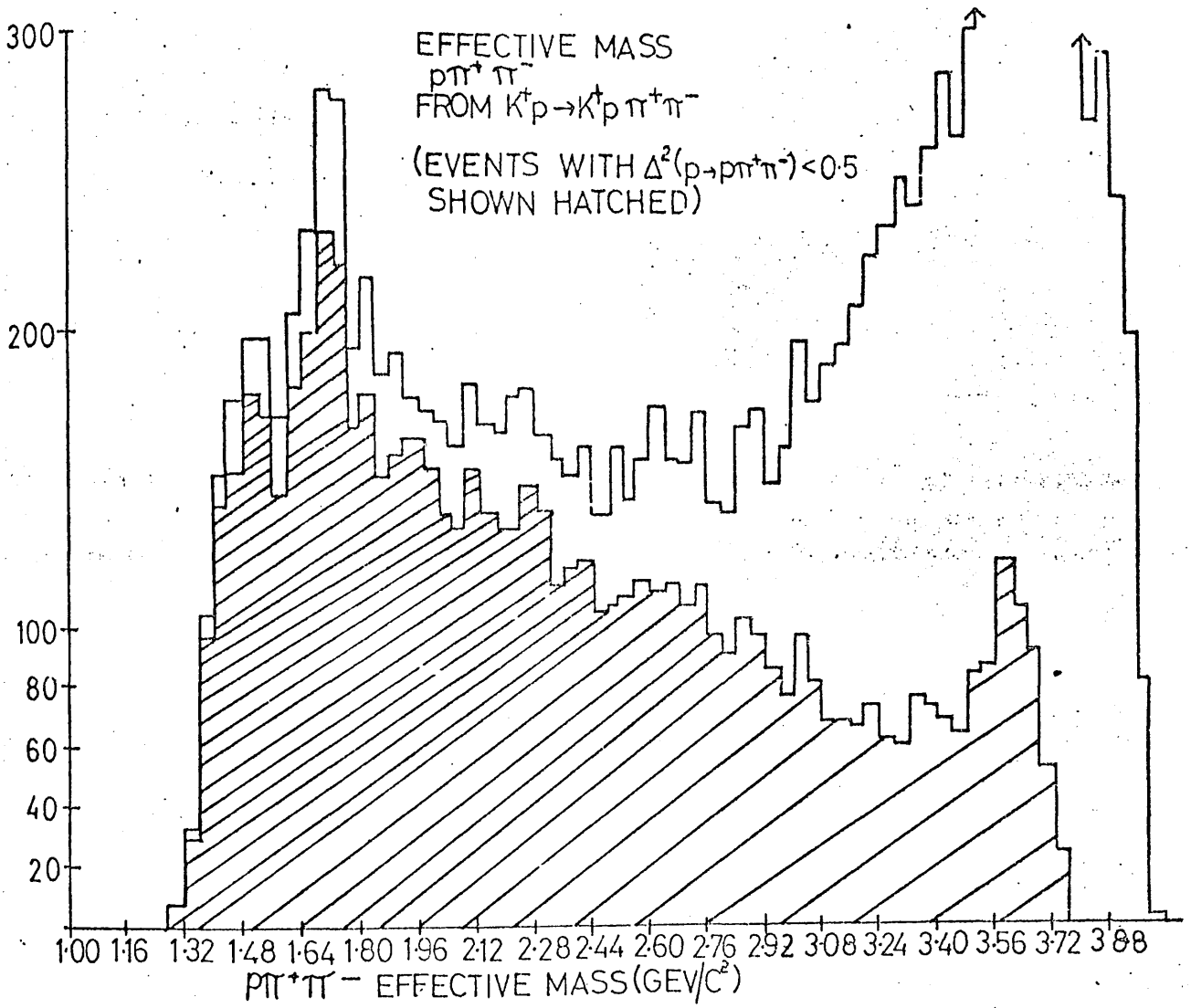

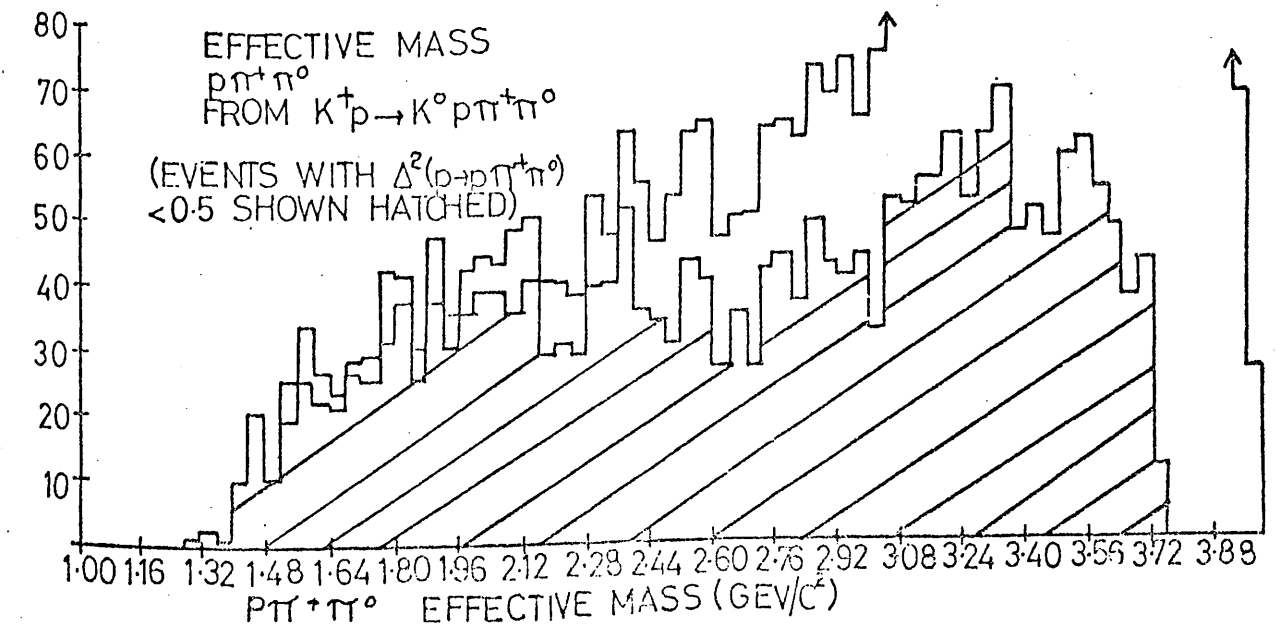

FIGURE 3.2 (above)

FIGURE 3.3 (below)

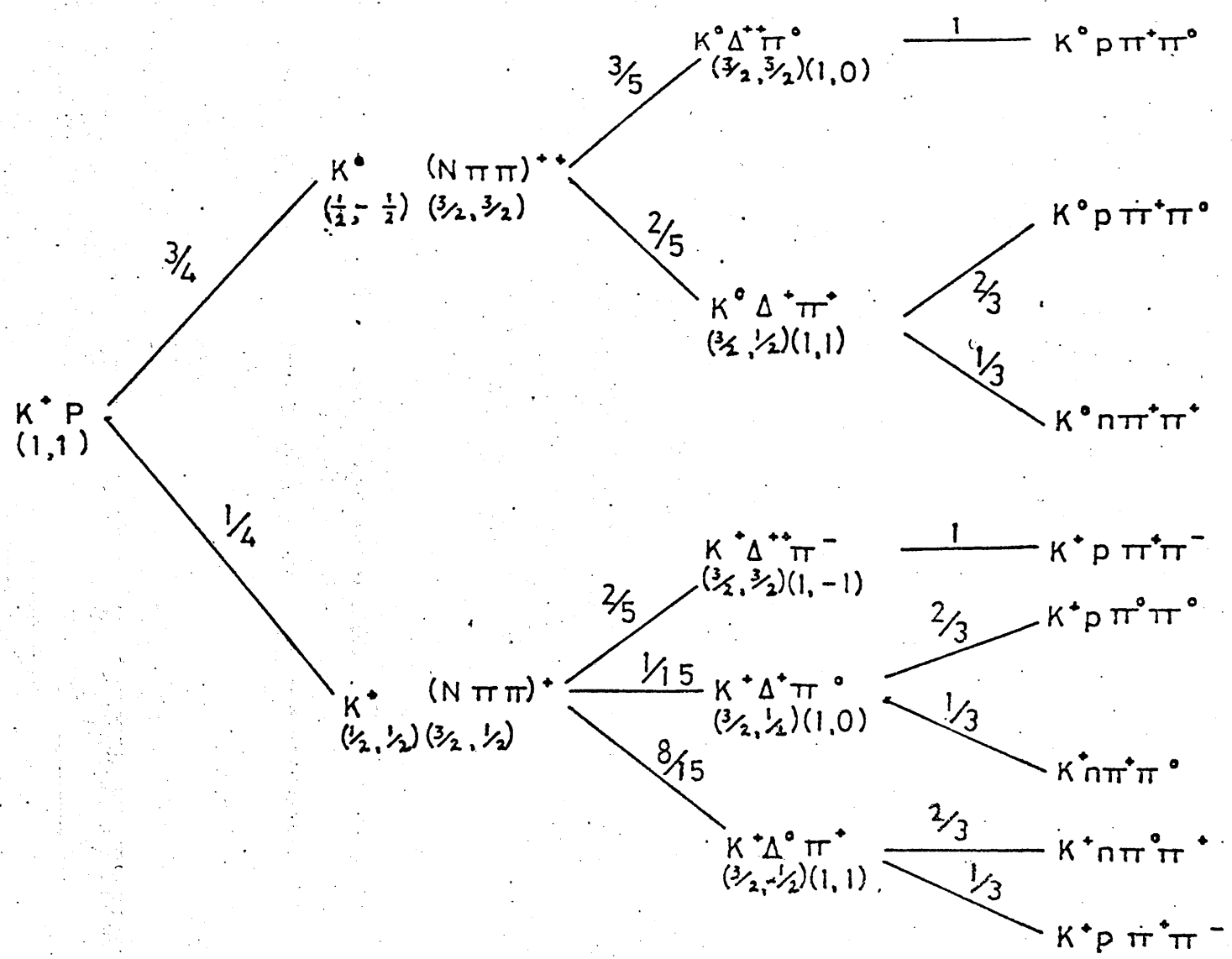

I-SPIN CLEBSCH-GORDAN COEFFICIENTS FOR I = 3/2 NTTTT STATE

FIGURE 3.4

$K^{\pm}p \to K^{\pm}p\,\pi^-\,\pi^-$

$\Delta^2(p \to p\,\pi^+\pi^-)$ DISTRIBUTIONS

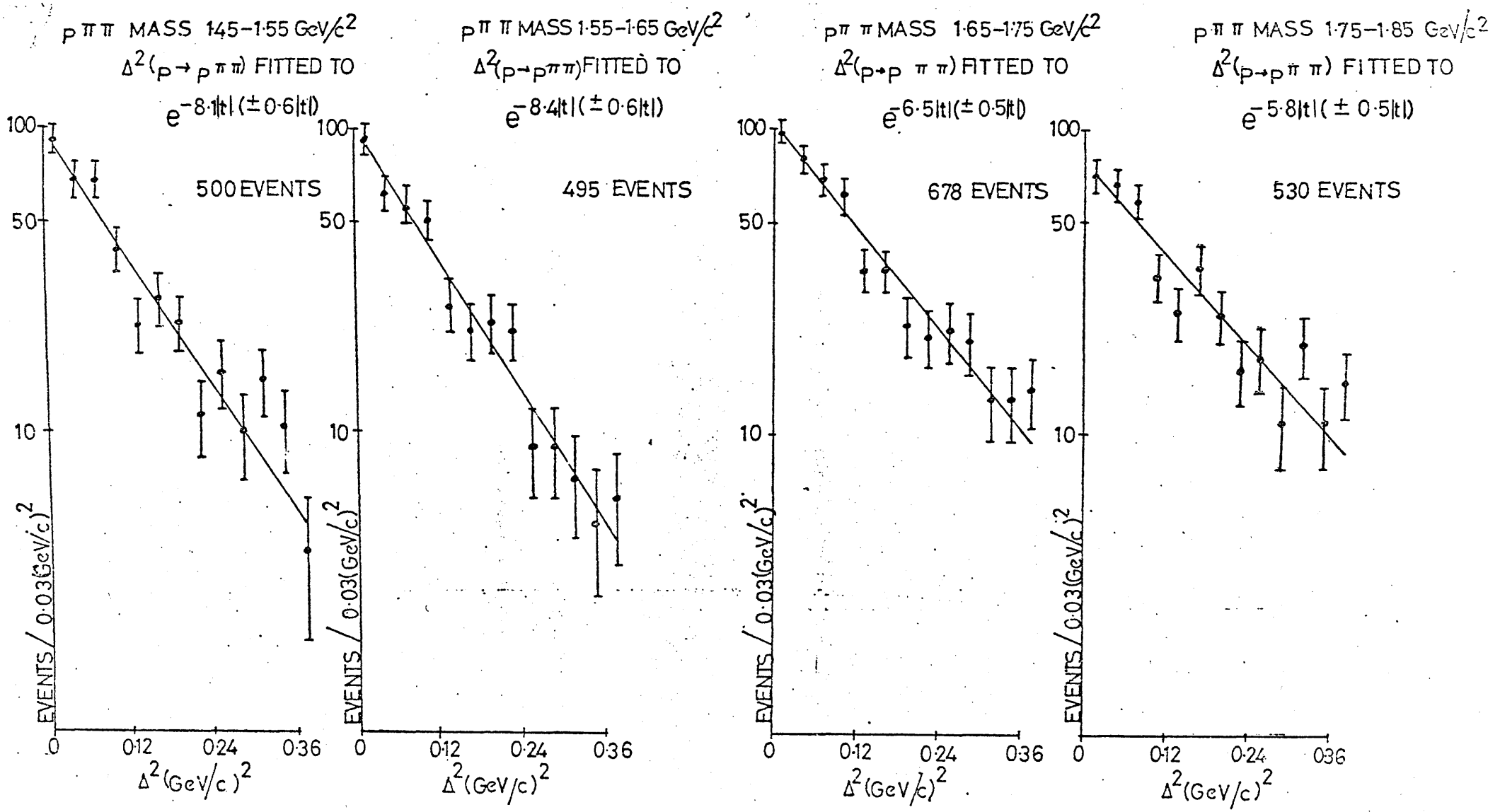

FIGURE 3.5

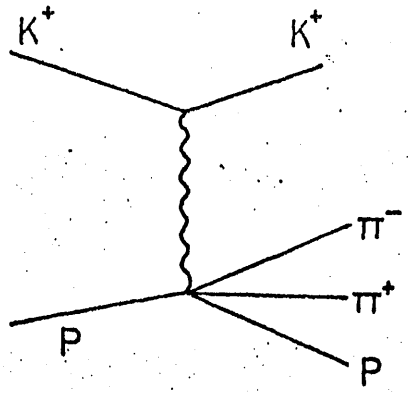

FIGURE 3.6

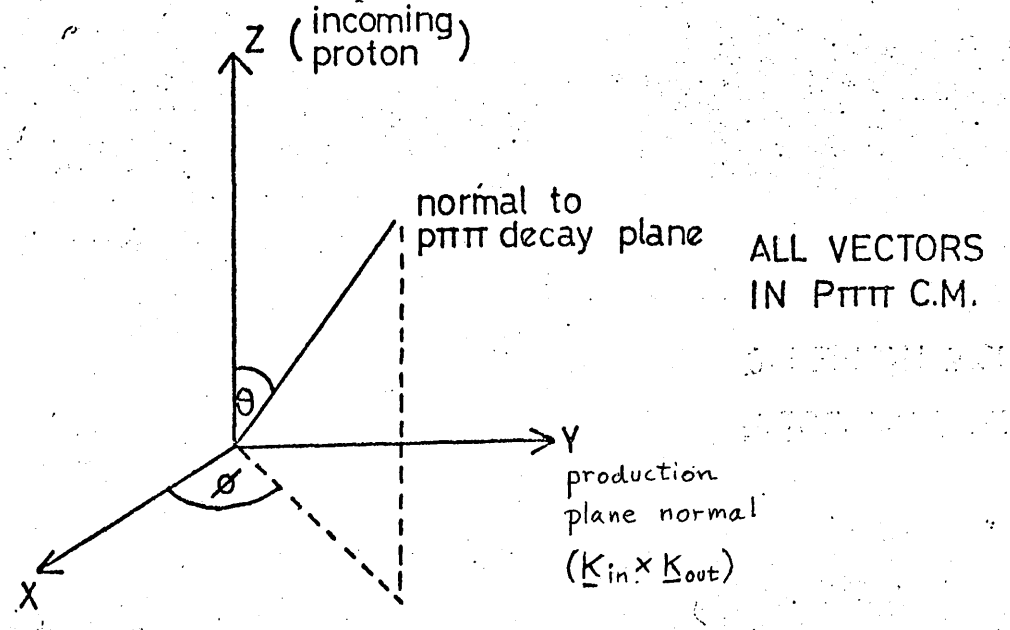

FIGURE 3.7

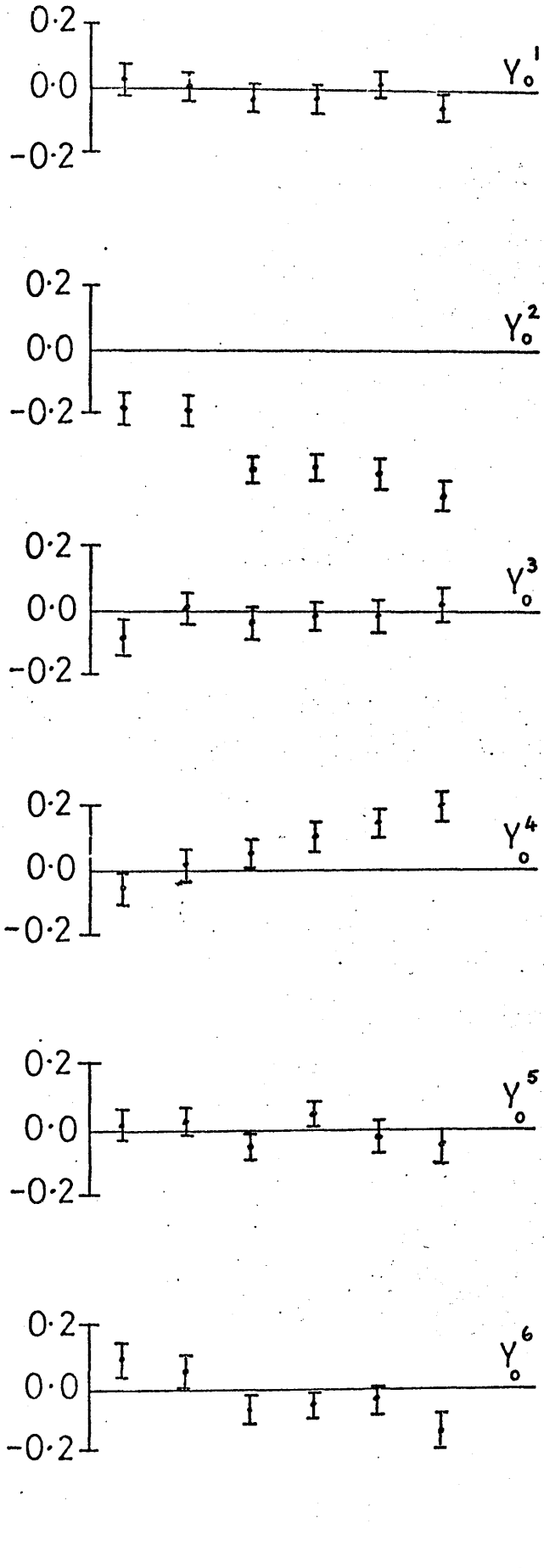

VARIATION OF SPHERICAL HARMONIC MOMENTS WITH $P\pi^+\pi^-$ EFFECTIVE MASS

FIGURE 3.8

PERCENTAGE OF TOTAL EVENTS WITH $P\pi^+$ EFFECTIVE MASS LYING BETWEEN 1·16–1·28 GeV/c^2

EVENTS WITH $\Delta^2(p\to p\pi^+\pi^-) > 0{\cdot}5\,(\mathrm{GeV}/c)^2$ OMITTED

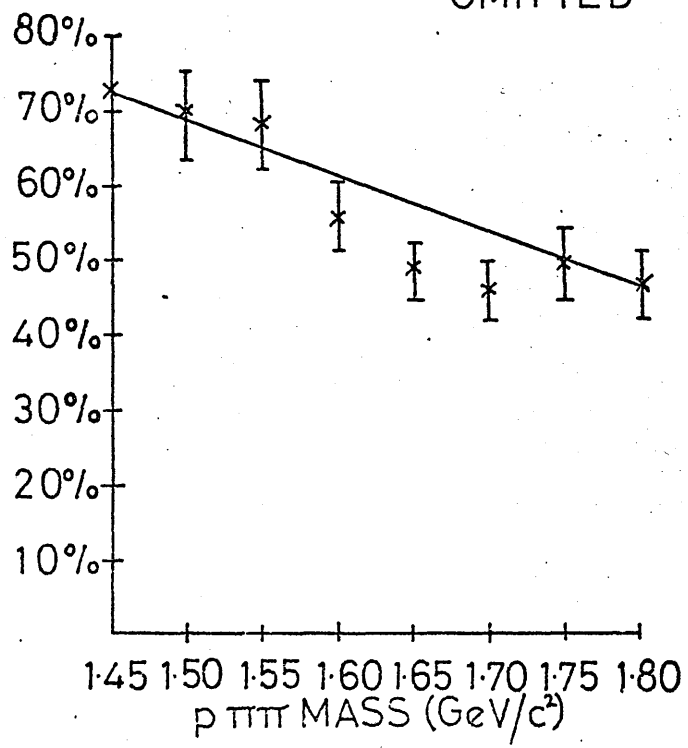

FIGURE 3.9

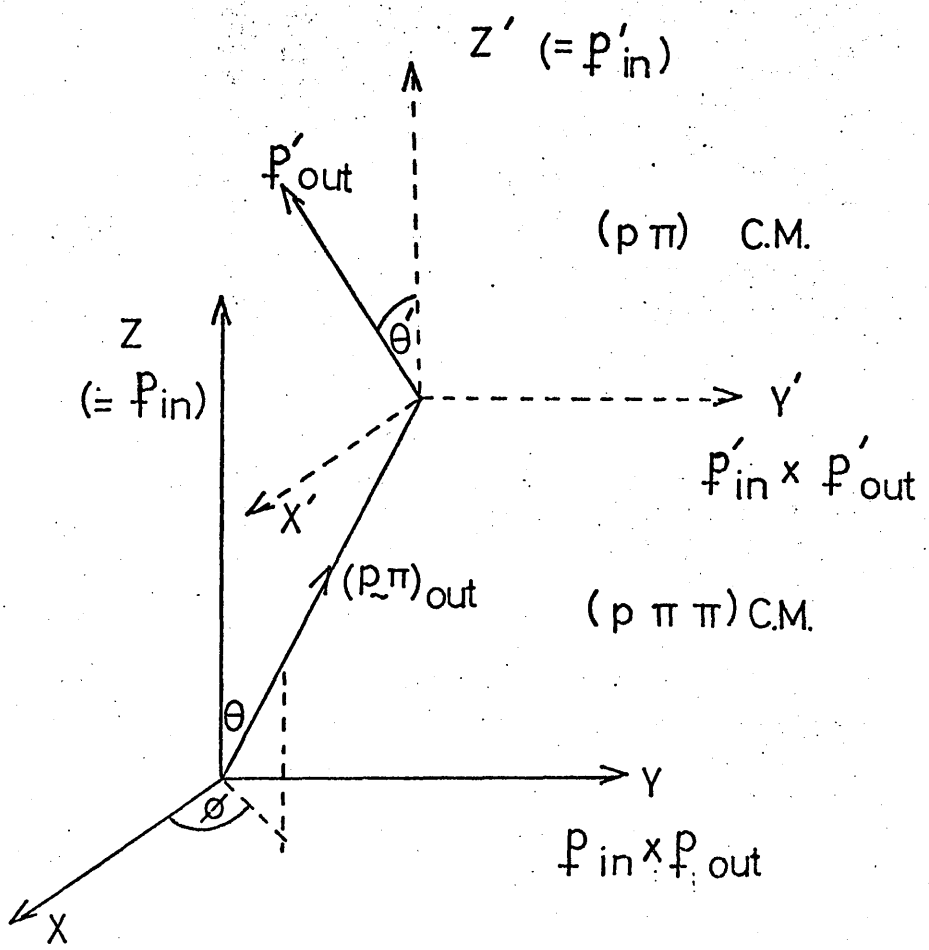

CO-ORDINATE AXES FOR DECAY OF P π π SYSTEM.

FIGURE 3.10

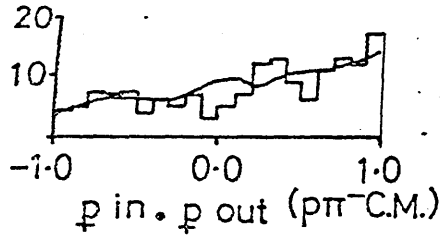

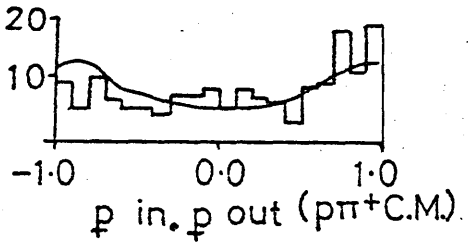

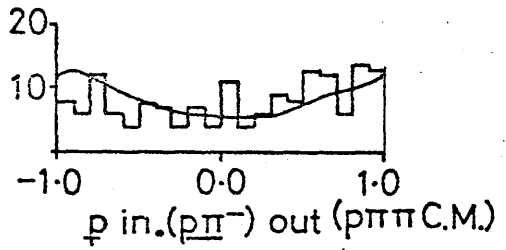

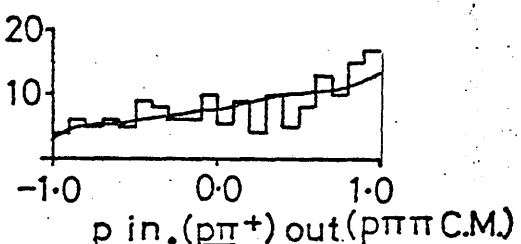

$1{\cdot}4 < M(p\pi^+\pi^-) < 1{\cdot}45$ GeV/c²

(160·5 EVENTS)

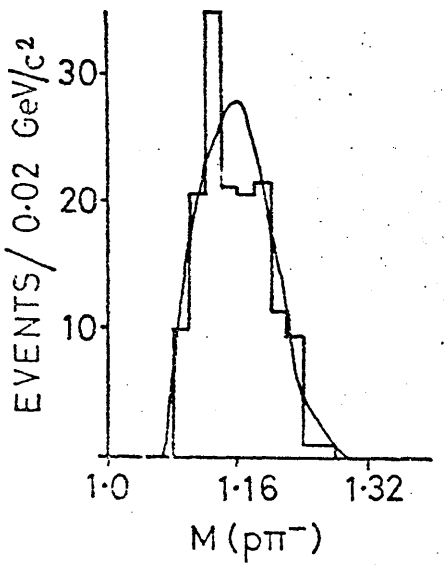

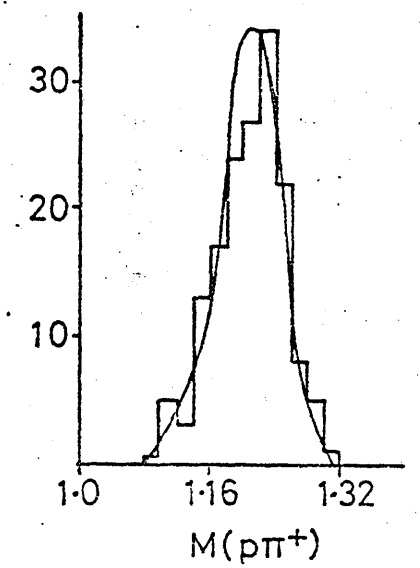

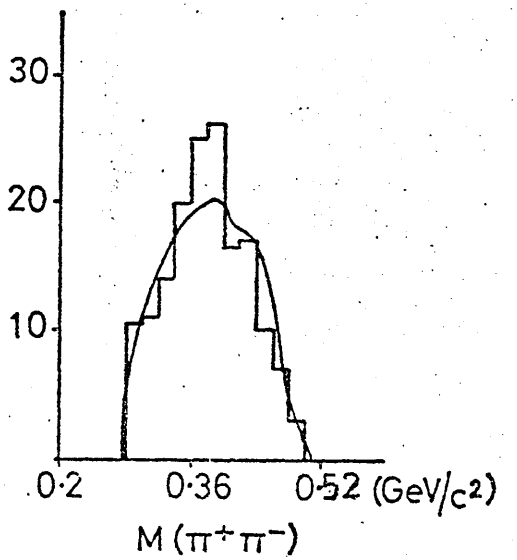

FIGURE 3.11

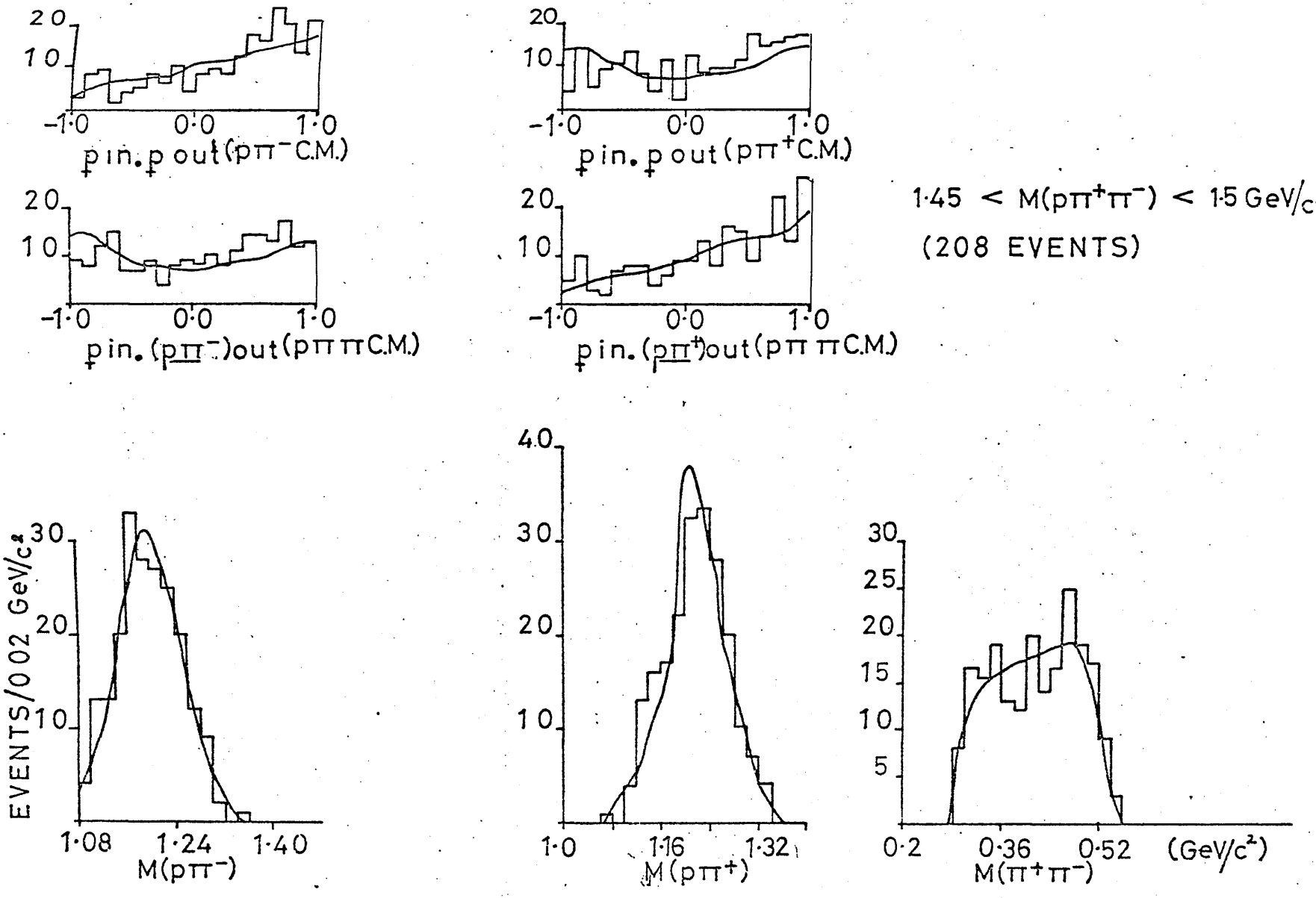
20
10
-1·0
0·0
1·0
p in. p out (pπ⁻ C.M.)
p in. p out (pπ⁺ C.M.)
p in. (pπ⁻) out (pππ C.M.)
p in. (pπ⁺) out (pππ C.M.)
1·45 < M(pπ⁺π⁻) < 1·5 GeV/c²
(208 EVENTS)
EVENTS/0·02 GeV/c²
30
20
10
1·08
1·24
1·40
M(pπ⁻)
4·0
30
20
10
1·0
1·16
1·32
M(pπ⁺)
30
25
20
15
10
5
0·2
0·36
0·52
(GeV/c²)
M(π⁺π⁻)

FIGURE 3.12

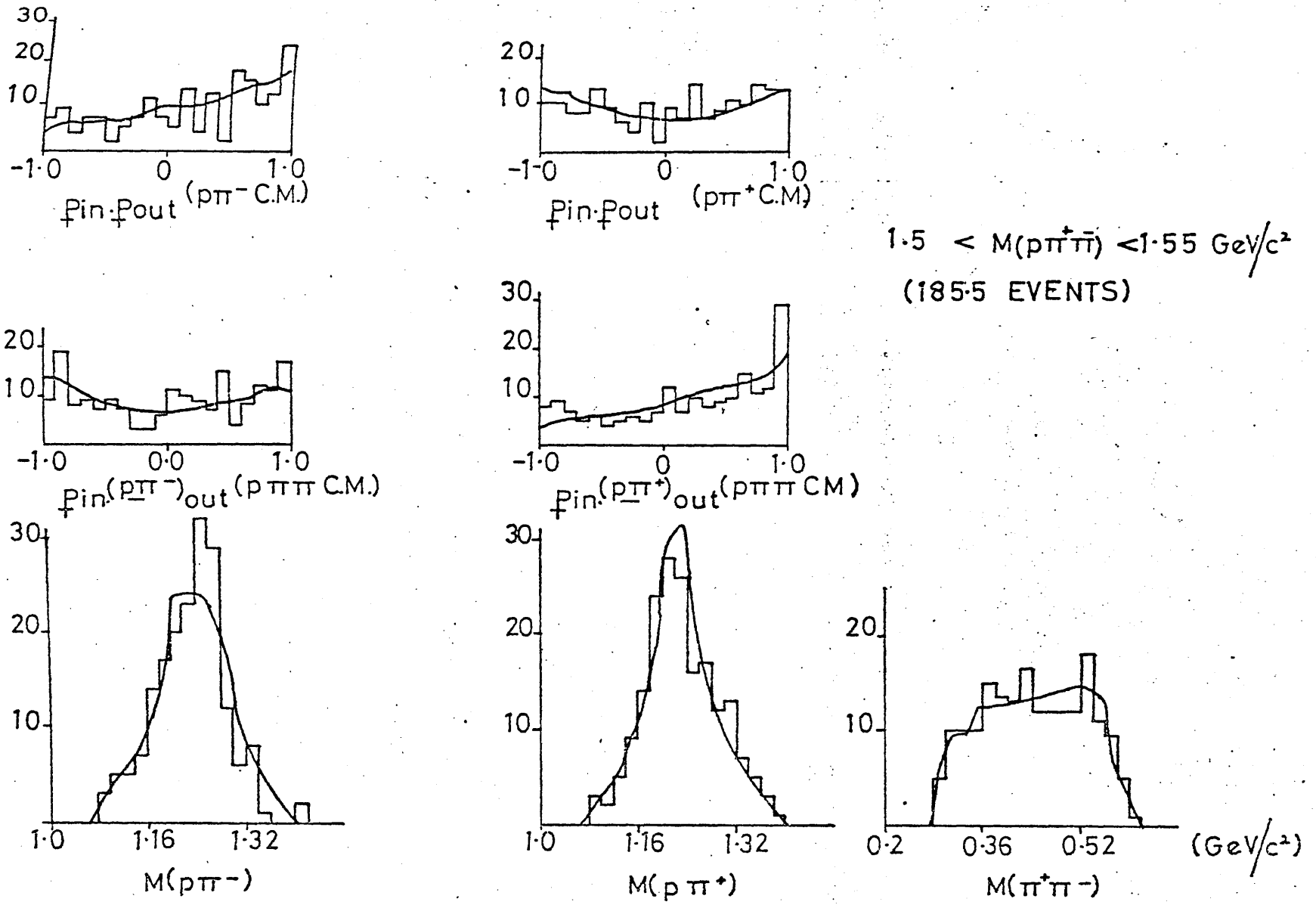
30
20
10
-1·0
0
1·0
p̂in·p̂out (pπ⁻ C.M.)
20
10
-1·0
0
1·0
p̂in·p̂out (pπ⁺C.M.)
1·5 < M(pπ⁺π⁻) <1·55 GeV/c²
(185·5 EVENTS)
20
10
-1·0
0·0
1·0
p̂in.(pπ⁻)out (pππ C.M.)
30
20
10
-1·0
0
1·0
p̂in.(pπ⁺)out (pππ CM)
30
20
10
1·0
1·16
1·32
M(pπ⁻)
30
20
10
1·0
1·16
1·32
M(pπ⁺)
20
10
0·2
0·36
0·52
(GeV/c²)
M(π⁺π⁻)

FIGURE 3.13

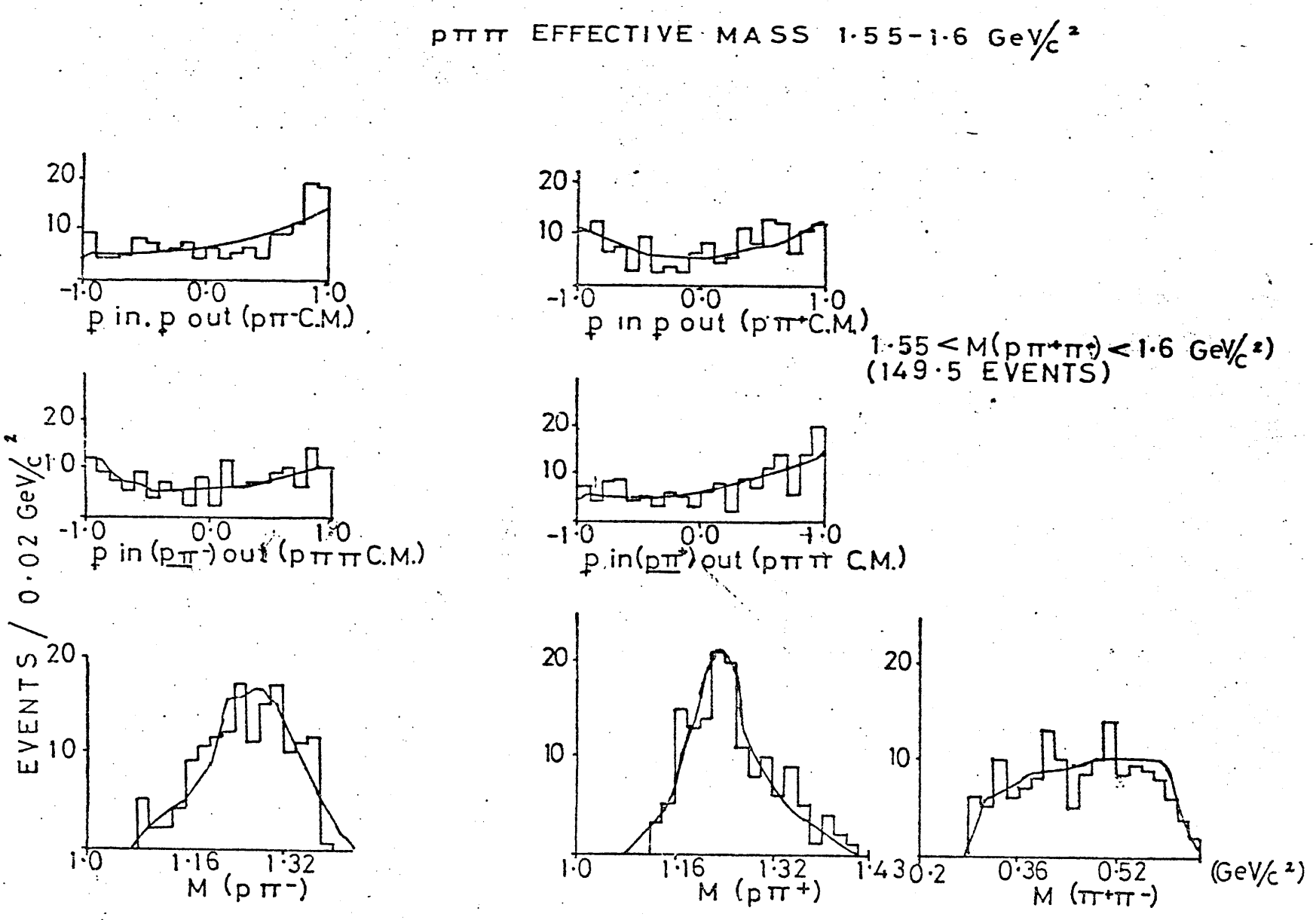
pππ EFFECTIVE MASS 1·55–1·6 GeV/c²
1·55 < M(pπ⁺π⁻) < 1·6 GeV/c²
(149·5 EVENTS)
p in, p out (pπ⁻C.M.)
p in p out (pπ⁺C.M.)
p in (pπ⁻) out (pππ C.M.)
p in (pπ⁺) out (pππ C.M.)
EVENTS / 0·02 GeV/c²
M (pπ⁻)
M (pπ⁺)
M (π⁺π⁻)
(GeV/c²)

FIGURE 3.14

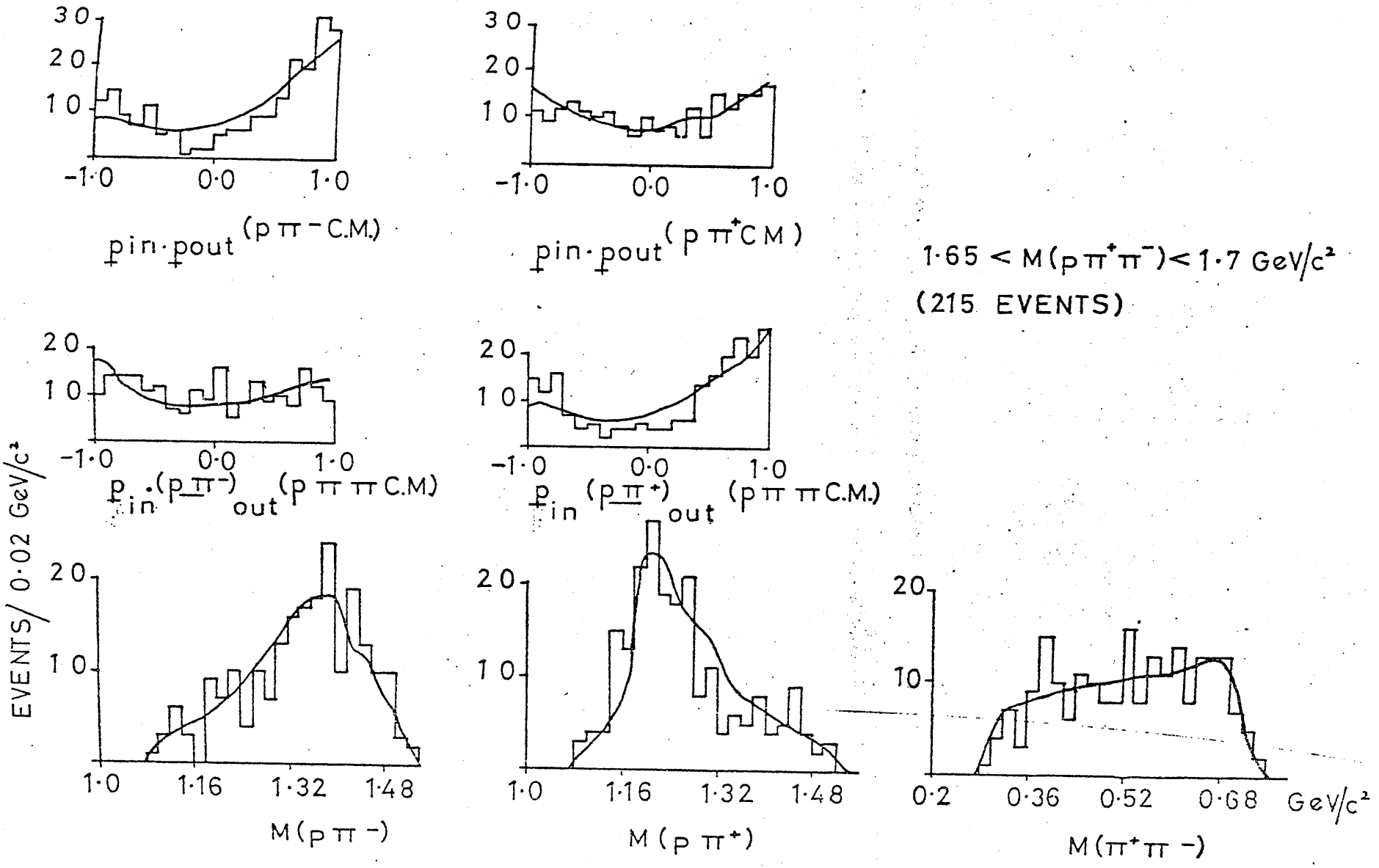
30
20
10
-1·0
0·0
1·0
$\hat{p}_{in} \cdot \hat{p}_{out}$ (p π⁻ C.M.)
$\hat{p}_{in} \cdot \hat{p}_{out}$ (p π⁺ C.M.)
1·65 < M(p π⁺ π⁻) < 1·7 GeV/c²
(215 EVENTS)
p_{in} (p π⁻) p_{out} (p π π C.M.)
p_{in} (p π⁺) p_{out} (p π π C.M.)
EVENTS / 0·02 GeV/c²
1·0
1·16
1·32
1·48
M(p π⁻)
M(p π⁺)
0·2
0·36
0·52
0·68
GeV/c²
M(π⁺ π⁻)

FIGURE 3.15

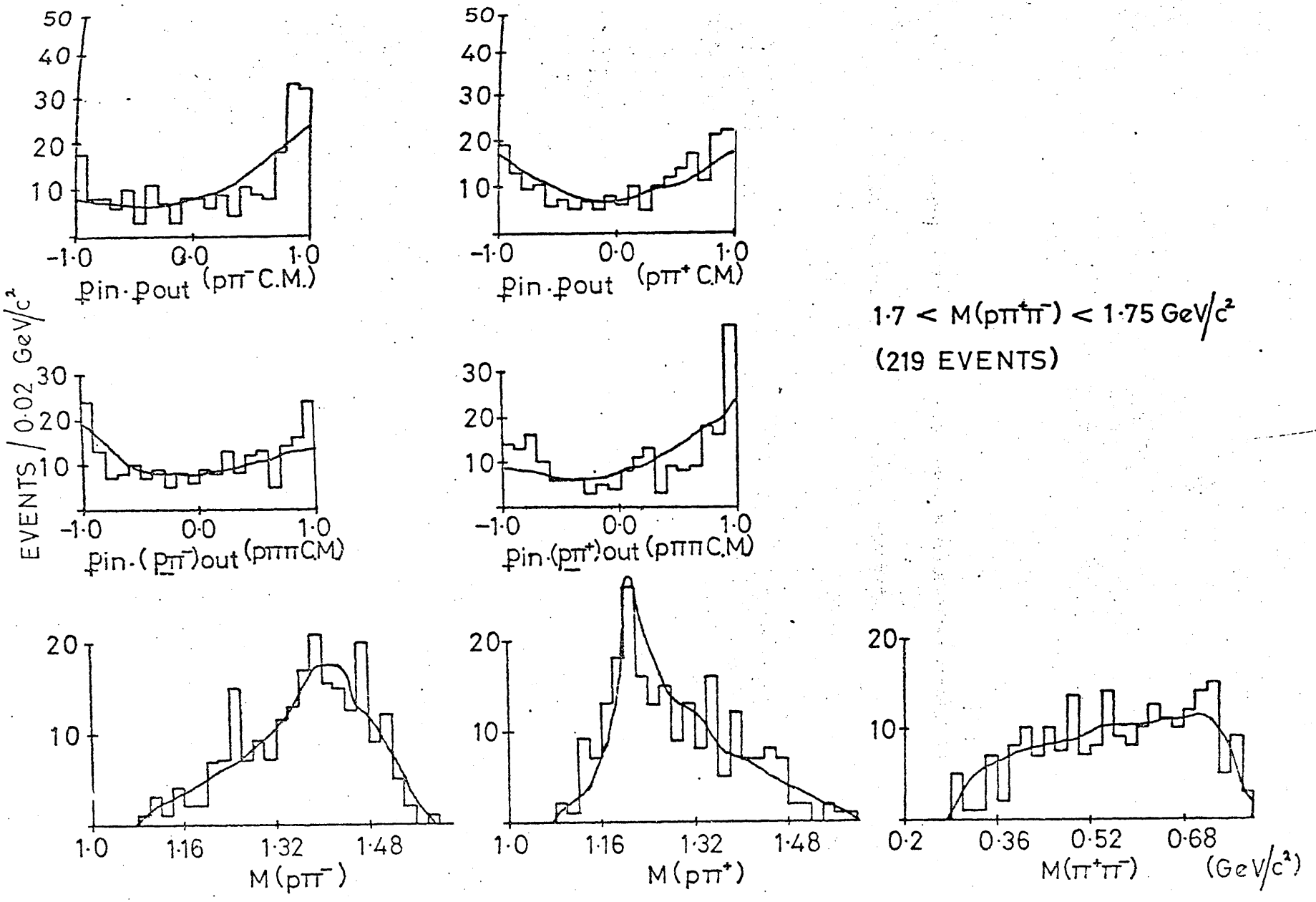
50
40
30
20
10
-1·0
0·0
1·0
p_in · p_out (pπ⁻ C.M.)
p_in · p_out (pπ⁺ C.M.)
EVENTS / 0·02 GeV/c²
p_in · (pπ⁻)_out (pππ C.M.)
p_in · (pπ⁺)_out (pππ C.M.)
1·7 < M(pπ⁺π⁻) < 1·75 GeV/c²
(219 EVENTS)
1·0
1·16
1·32
1·48
M(pπ⁻)
M(pπ⁺)
0·2
0·36
0·52
0·68
M(π⁺π⁻)
(GeV/c²)

FIGURE 3.16

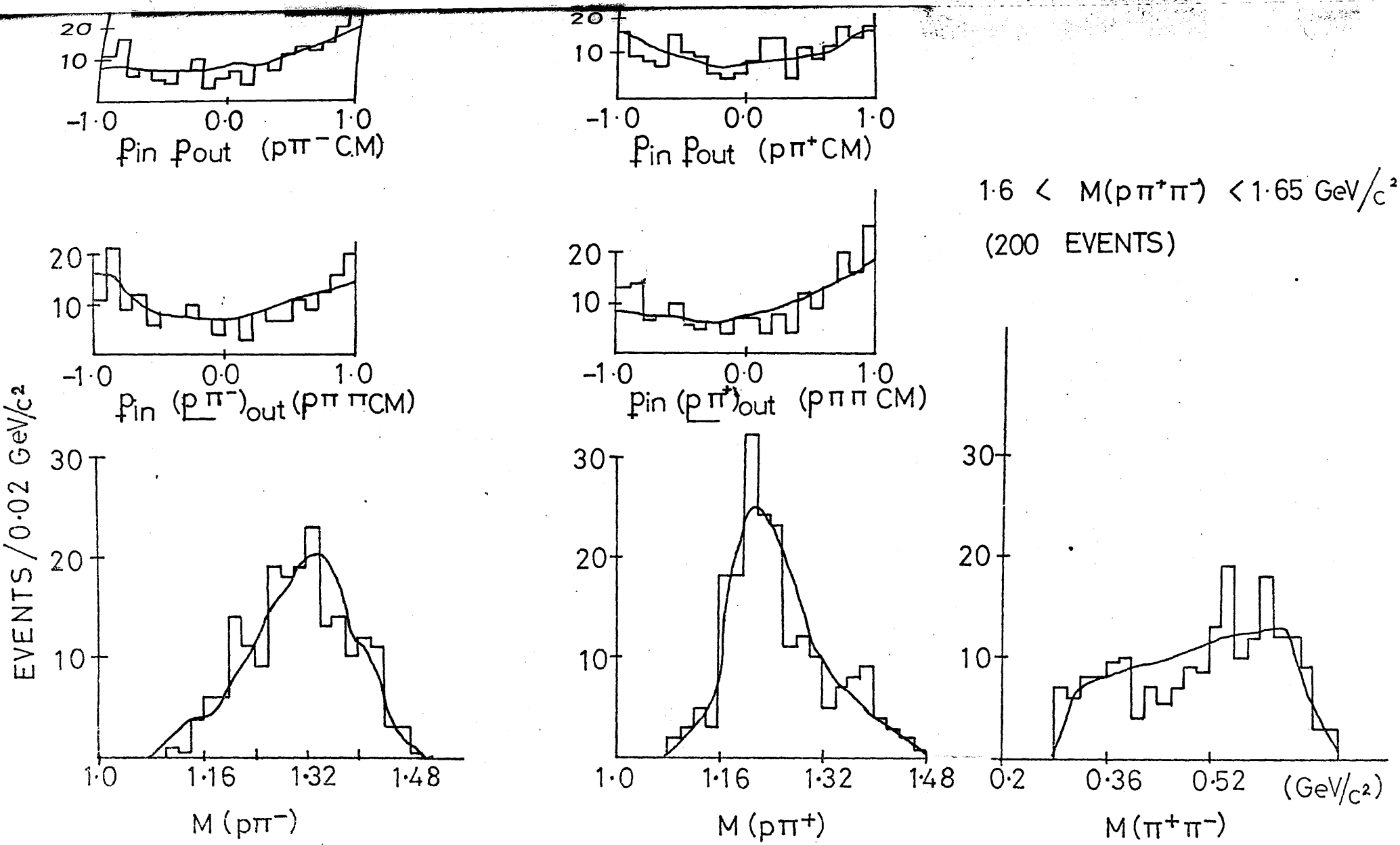
20
10
-1·0
0·0
1·0
p_{in} p_{out} ($p\pi^-$ CM)
p_{in} p_{out} ($p\pi^+$ CM)
p_{in} $(p\pi^-)_{out}$ ($p\pi\pi$ CM)
p_{in} $(p\pi^+)_{out}$ ($p\pi\pi$ CM)
1·6 < M($p\pi^+\pi^-$) < 1·65 GeV/c^2
(200 EVENTS)
EVENTS/0·02 GeV/c^2
30
20
10
1·0
1·16
1·32
1·48
M ($p\pi^-$)
M ($p\pi^+$)
0·2
0·36
0·52
(GeV/c^2)
M($\pi^+\pi^-$)

Fig. 3.17

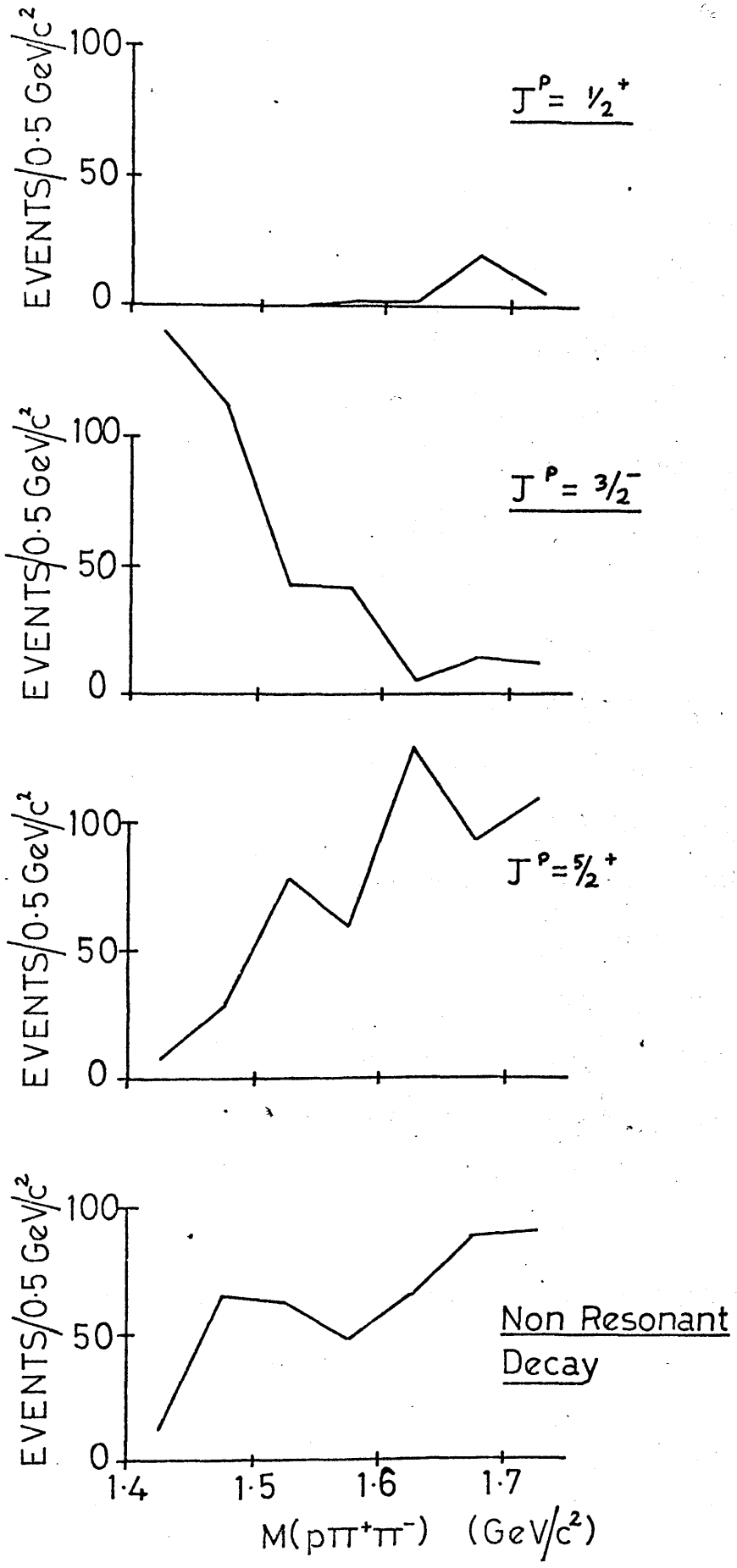
EVENTS/0·5 GeV/c²
100
50
0
$J^P = 1/2^+$
EVENTS/0·5 GeV/c²
100
50
0
$J^P = 3/2^-$
EVENTS/0·5 GeV/c²
100
50
0
$J^P = 5/2^+$
EVENTS/0·5 GeV/c²
100
50
0
Non Resonant
Decay
1·4
1·5
1·6
1·7
M(pπ⁺π⁻) (GeV/c²)

Fig. 3.18

CHAPTER IV

$\Delta^{++}(1900)$ Production.

IV.1 Introduction

Several doubly charged baryon resonances with masses higher than the well established $\Delta(1236)$ have been inferred from phase shift analyses, including two with masses in the 1670 MeV/c^2 region, and three resonances of mass around 1900 MeV/c^2. The masses and widths of these resonances are not precisely known. The spins, masses, widths, and branching ratios of these resonances from formation experiments are summarised in Table 4.1, which is derived from ref. 4.1.

Production experiment data for the $I=3/2$ region around 1900 MeV/c^2 suffers from the inability to distinguish between the three resonances in this region. However, investigation of the reactions in which an enhancement is formed at 1900 MeV/c^2, and the determination of the relative branching ratios via inelastic channels, gives information which is not easily obtainable from phase shift analysis. Enhancements at 1900 MeV/c^2, attributed to $I=3/2$ resonances, have been seen in π^-p, π^+p, and pp bubble chamber experiments. (See refs. 4.2, 4.3, and 4.4). In the Birmingham-Glasgow-Oxford 10 GeV/c experiment, the author has studied the channels:

$$K^+p \longrightarrow K^+p\pi^+\pi^- \qquad (1)$$

$$K^+p \longrightarrow K^+p\pi^+\pi^-\pi^0 \qquad (2)$$

$$K^+p \longrightarrow K^+n\pi^+\pi^+\pi^- \qquad (3)$$

$$K^+p \longrightarrow K^+p\pi^+\pi^+\pi^-\pi^- \qquad (4)$$

for evidence of the process:

$$K^+p \longrightarrow K^+\pi^-\Delta^{++}(1900) \qquad (5)$$

with subsequent decay of the Δ^{++} via two body, three body, or four body modes.

The channels:

$$K^+p \longrightarrow K^0p\pi^+ \qquad (6)$$

$$K^+p \longrightarrow K^0p\pi^+\pi^0 \qquad (7)$$

$$K^+p \longrightarrow K^0p\pi^+\pi^+\pi^- \qquad (8)$$

where the reaction:

$$K^+p \longrightarrow K^0\Delta^{++}(1900) \qquad (9)$$

could occur, have also been investigated.

IV.2 Evidence for Existence of $\Delta^{++}(1900)$

The $p\pi^+$ mass spectrum for reaction (1) is shown in figures 4.1(a) and 4.1(b), where only events for which $\Delta^2(p/p\pi^+) < 0.5$ $(GeV/c)^2$ are included. $\Delta^{++}(1236)$ production dominates this mass spectrum. There is also strong evidence for an enhancement at 1.9 GeV/c^2 $p\pi^+$ effective mass.

The $p\pi^+\pi^0$ and $n\pi^+\pi^+$ mass spectra from reactions (2) and (3) are combined in figure 4.2. In addition to imposing the condition $\Delta^2(p/(N\pi\pi)^{++}) < 0.5$ $(GeV/c)^2$, events from reaction (2) which have $M(\pi^+\pi^0\pi^-)$ within the $\omega(780)$ band (0.74 - 0.82 GeV/c^2), or $M(K^+\pi^0)$ within the $K^*(890)$ band (0.84 - 0.94 GeV/c^2) have been omitted here, and in subsequent sections of this chapter. An enhancement at 1.9 GeV/c^2 is prominent.

The $p\pi^+\pi^+\pi^-$ mass plots were investigated in the six prong events of reaction (4). No clear enhancement was visible in the 1.9 GeV/c^2 region,* which places an upper limit on the cross-section for decay of the $\Delta^{++}(1900)$ via $p\pi^+\pi^+\pi^-$.

No evidence for a doubly charged baryon resonance at 1.9 GeV/c^2 was obtained from reactions (6), (7), and (8).

The production of the $\Delta^{++}(1236)$ in the reaction (1) includes a high proportion of events formed in the quasi-two-body reaction: (See ref. 4.5)

$$K^+p \longrightarrow K^*(890)\,\Delta^{++} \qquad (1')$$

An estimate for the proportion of events from reaction (1), proceeding via the (corresponding quasi-two-body) reaction (1') can be gained from figure 4.3. This shows a $K^+\pi^-$ effective mass plot obtained by subtracting the $K^+\pi^-$ mass distribution for two $p\pi^+$ guard bands from the $K^+\pi^-$ mass distribution for events in the $\Delta^{++}(1900)$ peak. (The $p\pi^+$ mass region corresponding to the $\Delta^{++}(1900)$ peak was taken here as a 300 MeV/c^2 wide band centred on a $p\pi^+$ mass of 1.915 GeV/c^2. The guard bands were each 150 MeV/c^2 wide.) The percentage of events in figure 4.3 in which

---

* The probabilty of observing the $\Delta^{++}(1900)$ in the $p\pi^+$ plots of reaction (4) is reduced by the following factors:

a) the subsample of film from which the data of reaction (4) was obtained is smaller than for the other reactions.

b) there are two combinations of $p\pi^+$ for each event.

$K^*(890)$ is formed is around 58% ($\pm$ 5%), compared with 47% ($\pm$ 5%) in the $p\pi^+$ guard bands.

A background subtraction, similar to the method outlined above, but for the $K^+\pi^+\pi^-$ mass distribution of reaction (1), has shown that the $\Delta^{++}(1900)$ peak is not a kinematic reflection of a $K^+\pi^+\pi^-$ resonance.

IV.3 Mass and Width of $\Delta(1900)$

The number of events in the $p\pi^+$ mass distribution of figure 4.1(b), from reaction (1), decreases rapidly with increasing $p\pi^+$ effective mass. The $p\pi^+$ effective mass distribution between 1.4 GeV/c^2 and 2.76 GeV/c^2 was fitted satisfactorily by a linear background term, plus simple Breit-Wigners to represent the $\Delta^{++}(1900)$, and the influence of the $\Delta^{++}(1236)$ on the background.

$$F = (a + bM)(1 + BW(\Delta^{++}(1900)) + BW(\Delta^{++}(1236)))$$

where $BW = \dfrac{\times \left(\frac{\Gamma}{2}\right)^2}{(M - M_0)^2 + \left(\frac{\Gamma}{2}\right)^2}$

The results of this fit were:

MASS = 1.915 GeV/c^2 ($\pm$16 MeV/c^2)

WIDTH = 190 MeV/c^2 ($^{+36}_{-30}$ MeV/c^2)

The fit is shown superimposed on the $p\pi^+$ effective mass distribution in figure 4.4.

A similar type of polynomial fit to the $\Delta^{++}(1900)$ enhancement formed in reactions (2) and (3) would have been of doubtful value, due to the shape of the background - a visual estimate of the central mass of the peak in figure 4.2 gives a value of 1.88 GeV/c^2. The width is difficult to estimate, again due to the behaviour of the background,

but appears slightly less than the value obtained for reaction (1).

IV.4 Cross-Sections and Decay Branching Ratios

The production processes for the Δ (1900) are identical in reactions (1), (2), (3), and (4), viz:

$$K^+p \longrightarrow K^+\pi^- \Delta^{++}(1900)$$

The branching ratios of the $\Delta^{++}(1900)$ which are observable in reactions (1) to (4) can thus be obtained directly by comparing the cross-sections in Table 4.2. The number of events in the $\Delta^{++}(1900)$ peak in reaction (1) was obtained by integrating the Breit-Wigner multiplied by the linear function used to parameterise the $\Delta^{++}(1900)$. The number of $\Delta^{++}(1900)$ events above background in figure 4.2 was obtained by subtracting guard bands 80 MeV/c^2 wide from either side of the peak (1.84 - 1.96 GeV/c^2) of the $(N\pi\pi)^{++}$ mass distribution.

From Table 4.2, the branching ratio

$$\Delta^{++}(1900) \longrightarrow \frac{(N\pi\pi)^{++}}{(N\pi)^{++}} \approx 60\,\%$$

with an error of the order 15%.

$$\Delta^{++}(1900) \longrightarrow \frac{(N\pi\pi\pi\pi)^{++}}{(N\pi)^{++}} < 10\,\%$$

The three body decay $\Delta^{++}(1900) \rightarrow p\pi^+\pi^\circ$ seen in reaction (2) includes the following possible decay processes:

$$\Delta^{++}(1900) \longrightarrow \begin{cases} \Delta^{++}(1236)\pi^\circ \longrightarrow p\pi^+\pi^\circ & \text{(a)} \\ \Delta^{+}(1236)\pi^+ \longrightarrow p\pi^\circ\pi^+ & \text{(b)} \\ p\rho^+(760) \longrightarrow p\pi^+\pi^\circ & \text{(c)} \\ p\pi^+\pi^\circ & \text{(d)} \end{cases}$$

In figure 4.5(a), the percentage of events from reaction (2), with $p\pi^+$ mass lying in the $\Delta^{++}(1236)$ band, is plotted for eleven 100 MeV/c^2 wide bands across the $p\pi^+\pi^0$ mass distribution. The smooth variation of this percentage below 2.1 GeV/c^2 suggests that, in evaluating the branching ratio of the $\Delta^{++}(1900)$ peak via $\Delta^{++}(1236)\pi^0$, a background subtraction is unnecessary, since the background and peak behave similarly. The percentage of events with $\pi^+\pi^0$ mass in the $\rho(765)$ region shows a peak for $M(p\pi^+\pi^0)$ around 1820 MeV/c^2 (see figure 4.5(b)): this will be discussed later.

We used the programme FOWL (ref. 2.10) to generate phase space events for the isotropic decay to $p\pi\pi\pi$ of a system of mass 1.9 GeV/c^2, and width 200 MeV/c^2. (FOWL run 'A'). We also generated events for the sequential decay:

$$\Delta(1900) \longrightarrow p\rho \longrightarrow p\pi\pi\pi \qquad \text{(FOWL run 'B')}$$

For this restricted region of $p\pi\pi\pi$ mass, the $p\pi$ effective mass distributions from run 'A' and run 'B' did not differ appreciably, indicating that the kinematic reflections of $\rho(765)$ production can be ignored when assessing the $\Delta(1236)$ contribution to the $p\pi$ mass distribution.

FOWL run 'C' corresponded to the sequential decay:

$$\Delta(1900) \longrightarrow \Delta(1236)\pi_1 \longrightarrow p\pi_2\pi_1$$

in which the $p\pi_2$ mass distribution was a Breit-Wigner representing the $\Delta(1236)$, while the $p\pi_1$ mass distribution was the kinematic reflection of the $\Delta(1236)$. (The $\pi_1\pi_2$ spectrum was almost identical to the $\pi\pi\pi$ pure phase space

spectrum from FOWL run 'A': thus, conversely, $\Delta(1236)$ reflections can be ignored when calculating the $\rho(765)$ cross-section from the $\pi\pi$ mass spectrum).

Finally, the programme FOWL was used for the fourth time (run 'D') to simulate the coherent decay:

$$\Delta^{++}(1900) \longrightarrow \sqrt{\tfrac{3}{5}}\,\Delta^{++}(1236)\pi^{0} - \sqrt{\tfrac{4}{15}}\,\Delta^{+}(1236)\pi^{+}$$
$$\Delta^{++}(1236) \hookrightarrow p\pi^{+} \qquad \Delta^{+}(1236) \hookrightarrow p\pi^{0}$$

where the $\Delta^{++}(1236)$ and $\Delta^{+}(1236)$ terms are related by I-spin. (The I-spin Clebsch-Gordon coefficients for the process are:

$$\Delta^{++}(1900) \xrightarrow{\sqrt{3/5}} \Delta^{++}(1236)\pi^{0} \xrightarrow{1} p\pi^{+}\pi^{0}$$
$$\Delta^{++}(1900) \xrightarrow{-\sqrt{2/5}} \Delta^{+}(1236)\pi^{+} \xrightarrow{\sqrt{2/3}} p\pi^{0}\pi^{+}$$
$$\Delta^{+}(1236)\pi^{+} \xrightarrow{\sqrt{1/3}} n\pi^{+}\pi^{+}$$

).

The two one-dimensional $p\pi^{+}$ and $p\pi^{0}$ exponential mass distributions, for the events from reaction (2) in the $\Delta^{++}(1900)$ region ($1.8 < M(p\pi^{+}\pi^{0}) < 2.0$ GeV/c^{2}), were fitted simultaneously, to the function S_1 given by:

$$S_1(M_1, M_2) = N\left(X F_D(M_1, M_2) + (1-X) F_A(M_1, M_2)\right)$$

where M_1, M_2 are $p\pi^{+}$, $p\pi^{0}$ effective masses respectively

N is the number of events

F_D is the $p\pi^{+}$ - $p\pi^{0}$ mass distributions from FOWL run 'D'

F_A is the $p\pi^{-}$ - $p\pi^{+}$ phase space distribution from FOWL run 'A'

X is the fraction of $\Delta(1236)\pi$.

The χ^2- fit, over 18 bins of the $p\pi^{+}$ and $p\pi^{0}$ effective mass histograms, is shown by the dotted curves in figure 4.6. The fit to the $p\pi^{+}$ mass histogram is good, but the amount

of $\Delta^+(1236)$ in the $p\pi^\circ$ mass plot is overestimated. A second χ^2- fit, in which the relative amounts of $\Delta^{++}(1236)\pi^-$ and $\Delta^+(1236)\pi^+$ were allowed to vary independently, is shown as the dashed curve. The function S_2 fitted to the experimental histograms can be written:

$$S_2(M_1,M_2) = N\left(X_1 F_c(M_1,M_2) + X_2 F_c(M_2,M_1) + (1-X_1-X_2)F_B(M_1,M_2)\right)$$

where F_c is the $p\pi_2$ - $p\pi_1$ mass distribution from FOWL run 'C'

X_1 is the fraction of $\Delta^{++}(1236)\pi^\circ$

X_2 is the fraction of $\Delta^+(1236)\pi^+$

The second curve is a better fit to the data. The percentage of events going via $\Delta(1236)\pi$ to $p\pi^+\pi^\circ$ is 37% by the first estimate, and 28% by the second method. The overestimate of $\Delta^+(1236)\pi^+$ production produced by the coherent decay model perhaps may be caused by the crudeness of applying pure three body phase space as a background term to describe a $p\pi^+\pi^\circ$ system formed in 10 GeV/c [illegible] interactions. The lower value of 28% via $\Delta(1236)\pi$ gives the better fit.

The percentage of events from the $\Delta^{++}(1900)$ peak which have $\pi^+\pi^\circ$ effective mass in the $\rho^+(765)$ region varies rapidly above ρ threshold (see figure 4.5). A simple background subtraction method to obtain the branching ratio of the $\Delta^{++}(1900)$ would not be reliable. Instead, phase space $\pi\pi$ effective mass distributions, formed in the three body isotropic decay of a $p\pi\pi$ system

were simulated using the programme FOWL. Three such distributions were used: one corresponded to the $\Delta^{++}(1900)$ region ($1.8 < M(p\pi\pi) < 2.0$ GeV/c^2), while the other two were for 100 MeV/c^2 wide guard bands on either side. These phase space distributions, normalised appropriately, were compared with the experimental $\pi^+\pi^\circ$ effective mass histograms for the same $p\pi^+\pi^\circ$ mass regions (see figure 4.7). An estimate of $\rho(765)$ production was obtained for each of the three regions. The guard band figure were then subtracted from the central region, and this gave an estimate of less than 16% for the percentage of events in the $\Delta^{++}(1900)$ peak going via $\rho^+(765)p$.

Table 4.3 contains a summary of the information on branching ratios evaluated in this section.

The differential cross-section for production of the $p\pi^+$ combination in reaction (1) was also investigated. The four-momentum-transfer-squared distribution from the target to the $p\pi^+$ system, for 100 MeV/c^2 wide $p\pi^+$ mass regions, using events from reaction (1), was fitted to an exponential of the form $A\exp(-b\Delta^2)$ over the range $0.1 < \Delta^2(p/p\pi^+) < 0.5$ $(GeV/c)^2$. The exponent, as a function of $p\pi^+$ effective mass, is plotted in figure 4.8. The $\Delta^{++}(1236)$ is produced peripherally. The 1.9 GeV/c^2 differential cross-section falls as $\exp(-2.5\,\Delta^2)$.

IV.5 Conclusions

A doubly charged baryon enhancement occurs at 1.9 Gev/c^2 in the final states $K^+\pi^-\pi^+p$ and $K^+\pi^-(N\pi\pi)^{++}$ corresponding to the reaction:

$$K^+p \longrightarrow K^+\pi^- \Delta^{++}(1900)$$

There is good evidence for the quasi-two-body reaction:

$$K^+p \longrightarrow K^{*\circ}(890)\,\Delta^{++}(1900)$$

The enhancement at 1.9 GeV/c^2 has not been identified in reactions of the type:

$$K^+p \longrightarrow K^\circ\,\Delta^{++}(1900)$$

This may suggest that the enhancement is formed in a pion exchange process. Pion exchange is forbidden at the kaon vertex of this last reaction. Branching ratios for the $\Delta^{++}(1900)$ show that the elasticity of the resonance is not higher than 60%. Roughly 30% of the three body decay to $p\,\pi^+\pi^\circ$ proceeds via the $\Delta(1236)\pi$ intermediate state. The $p\rho^+$ branching ratio is small if it exists. Unique identification of the resonance is impossible, since the background is much too high for the resonance spin to be determined.

References

4.1 Particle Data Group

Reviews of Modern Physics 43 (1971) S1

4.2 Y.Y.Lee et al.

Physical Review 159,1156 (1967)

T.S.Yoon et al.

Physics Letters 24B, 307 (1967)

4.3 K.F.Galloway

Physics Letters 26B, 334 (1968)

4.4 W.Chinowsky

Physical Review 171,1421 (1968)

G.Alexander

Physical Review 154,1284 (1967)

4.5 I.Griffiths

Ph.D.Thesis Glasgow 1969 (see ref 2.3)

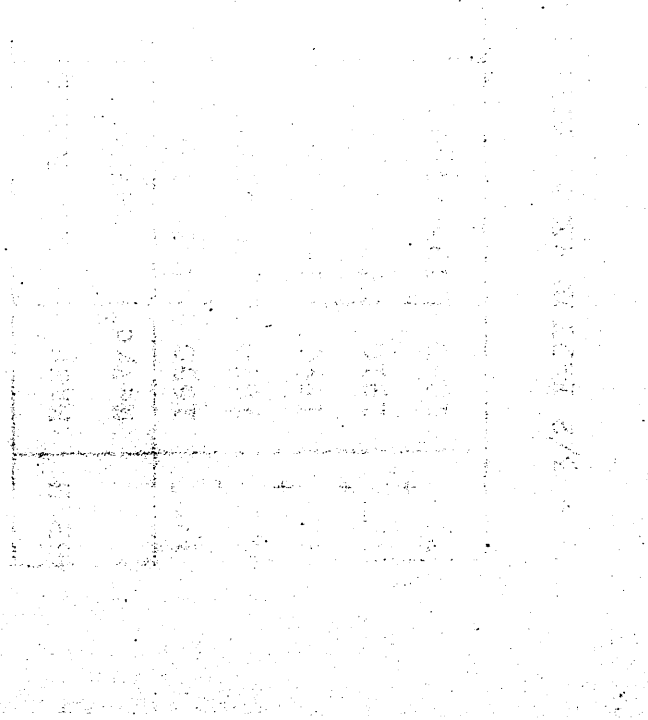

SPIN	MASS (MeV/c^2)	MASS RANGE MeV/c^2	WIDTH MeV/c^2	MAIN BRANCHING RATIOS (%)		
				$N\pi$	$N\pi\pi\pi$	$\Delta(1236)\pi$
$1/2^-$	1650	1615-1695	130-200	28	72	0
$3/2^-$	1670	1650-1720	175-300	15	-	-
$5/2^+$	1890	1840-1920	135-350	17	-	-
$1/2^+$	1910	1780-1935	230-420	25	-	-
$7/2^+$	1950	1930-1980	140-220	45	0	50

I = 3/2 BARYON RESONANCES (1650-1950 MeV/c^2) FROM REFERENCE 4.1

TABLE 4.1

	FINAL STATE	NUMBER OF EVENTS(1)	CROSS-SECTION(2) (MICROBARNS)	CROSS-SECTION FOR $\Delta^{++}(1900)$ PRODUCTION(3) (μb)
1	$K^+p\pi^+\pi^-$	14265	1317 (± 260)	26 (± 6.5)
2	$K^+p\pi^+\pi^-\pi^o$	7303	1115 (4)	15 (4)
3	$K^+\pi^+\pi^+\pi^-n$	1854	286 (4)	
4	$K^+p\pi^+\pi^+\pi^-\pi^-$	862	239 (± 50)	< 3

TABLE 4.2

(1) These figures apply after missing mass and probability cuts had been applied to the 1C channels.

(2) Events with final states 2 and 3, and 4, were obtained from subsets of the total data.

(3) This is the cross-section for the process $K^+p \rightarrow K^+\pi^-\Delta^{++}(1900)$ with $\Delta^2(p/\Delta^{++}) < 0.5\ (GeV/c)^2$.

(4) Due to the background in these channels and the need to make cuts to purify the sample we cannot quote a meaningful error on the cross sections.

Missing mass and probability cuts: Missing pion events accepted if missing mass squared lies between -0.05 and 0.10 $(GeV/c^2)^2$. Missing neutron events have missing mass squared between 0.70 and 1.05 $(GeV/c^2)^2$. In both types of missing neutral events, fits with probability less than 10% were rejected.

Figure Captions

4.1(a) The $p\pi^+$ effective mass spectrum from the final state. Events with $\Delta^2(p/p\pi^+) > 0.5$ $(GeV/c)^2$ omitted.

4.1(b) The same as figure 4.1(a), with a different vertical scale.

4.2 The $p\pi^+\pi^0$ effective mass spectrum from the $K^+p\pi^+\pi^-\pi^0$ final state (events with $0.74 < M(\pi^+\pi^0\pi^-) < 0.82$ GeV/c^2, and $0.84 < M(\pi^+\pi^0\pi^-) < 0.94$ GeV/c^2 antiselected), added to the $n\pi^+\pi^+$ spectrum from the $K^+n\pi^+\pi^+\pi^-$ final state. Events with $\Delta^2(p/(N\pi\pi)^{++}) > 0.5$ $(GeV/c)^2$ omitted.

4.3 $K\pi^-$ effective mass spectrum for $\Delta^{++}(1900)$ peak, with background subtracted.

4.4 The polynomial fit to the $p\pi^+$ effective mass spectrum, between 1.4 GeV/c^2 and 2.76 GeV/c^2.

4.5 Percentage of events for $K^+p\pi^+\pi^-\pi^0$ final state, with (a) $p\pi^+$ effective mass within $\Delta^{++}(1236)$ band
(b) $\pi^+\pi^0$ effective mass within $\rho^+(765)$ band.

4.6 Fits to (a) the $p\pi^+$, and (b) the $p\pi^0$ mass distributions from the decay of the $\Delta^{++}(1900)$ into $p\pi^+\pi^0$, via $\Delta(1236)\pi$ or three body phase space.

4.7 Phase space $\pi\pi$ distributions, compared with experiment, for the central $\Delta^{++}(1900)$ region ($1.8 < M(p\pi^+\pi^0) < 2.0$ GeV/c^2) and two 100 MeV/c^2 wide adjacent guard bands.

4.8 Four-momentum-transfer-squared from target to $p\pi^+$ system in $K^+p\pi^+\pi^-$ final state.

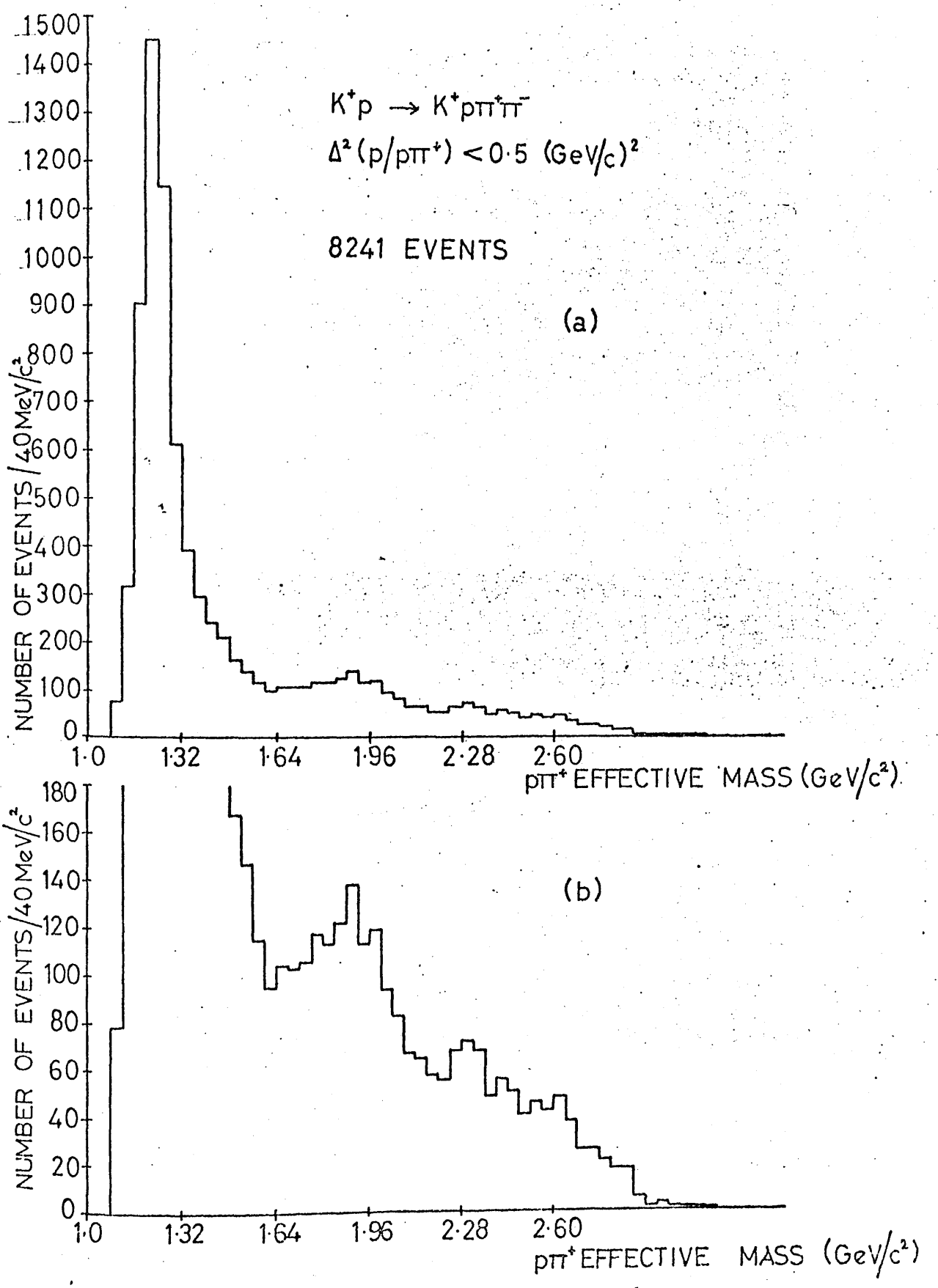

FIGURES 4.1(a) and (b)

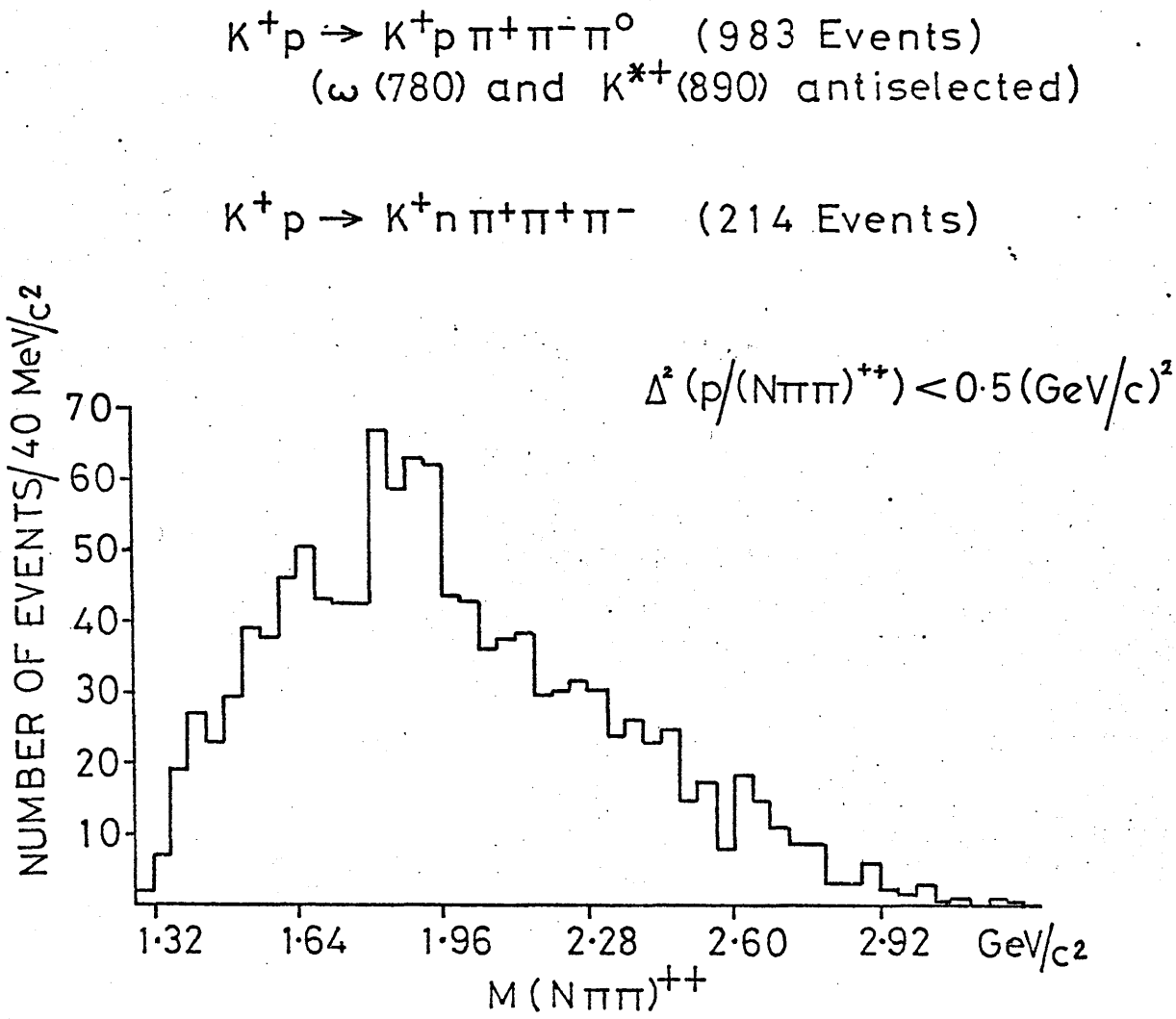
$K^+p \to K^+p\,\pi^+\pi^-\pi^0$ (983 Events)
(ω (780) and K^{*+}(890) antiselected)
$K^+p \to K^+n\,\pi^+\pi^+\pi^-$ (214 Events)
$\Delta^2(p/(N\pi\pi)^{++}) < 0.5\,(GeV/c)^2$
NUMBER OF EVENTS/40 MeV/c²
70
60
50
40
30
20
10
1·32
1·64
1·96
2·28
2·60
2·92
GeV/c²
M (Nππ)⁺⁺

FIGURE 4.2

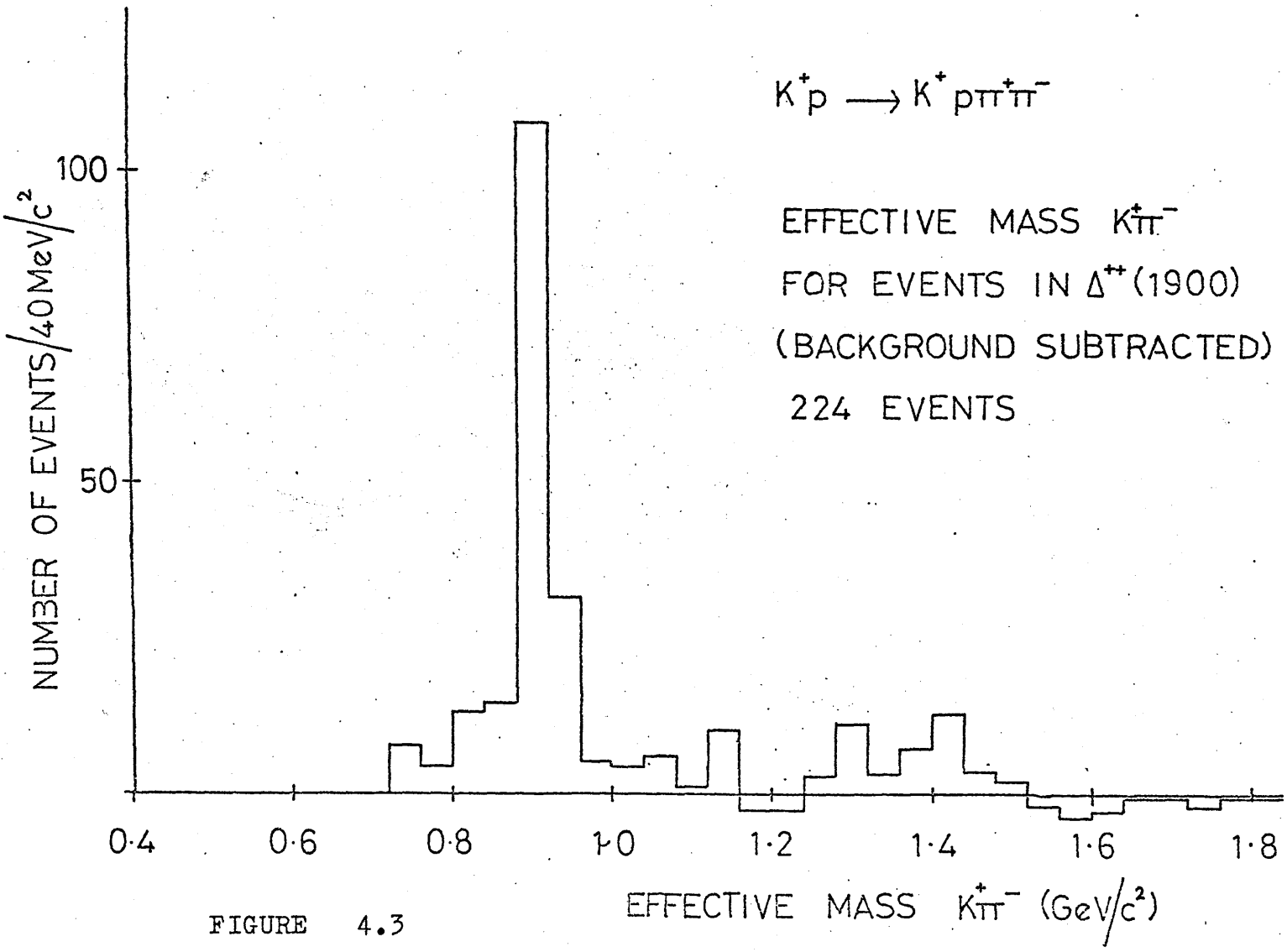
$K^+p \longrightarrow K^+p\pi^+\pi^-$
EFFECTIVE MASS $K^+\pi^-$
FOR EVENTS IN $\Delta^{++}(1900)$
(BACKGROUND SUBTRACTED)
224 EVENTS
NUMBER OF EVENTS/40MeV/c^2
100
50
0·4
0·6
0·8
1·0
1·2
1·4
1·6
1·8
EFFECTIVE MASS $K^+\pi^-$ (GeV/c^2)

FIGURE 4.3

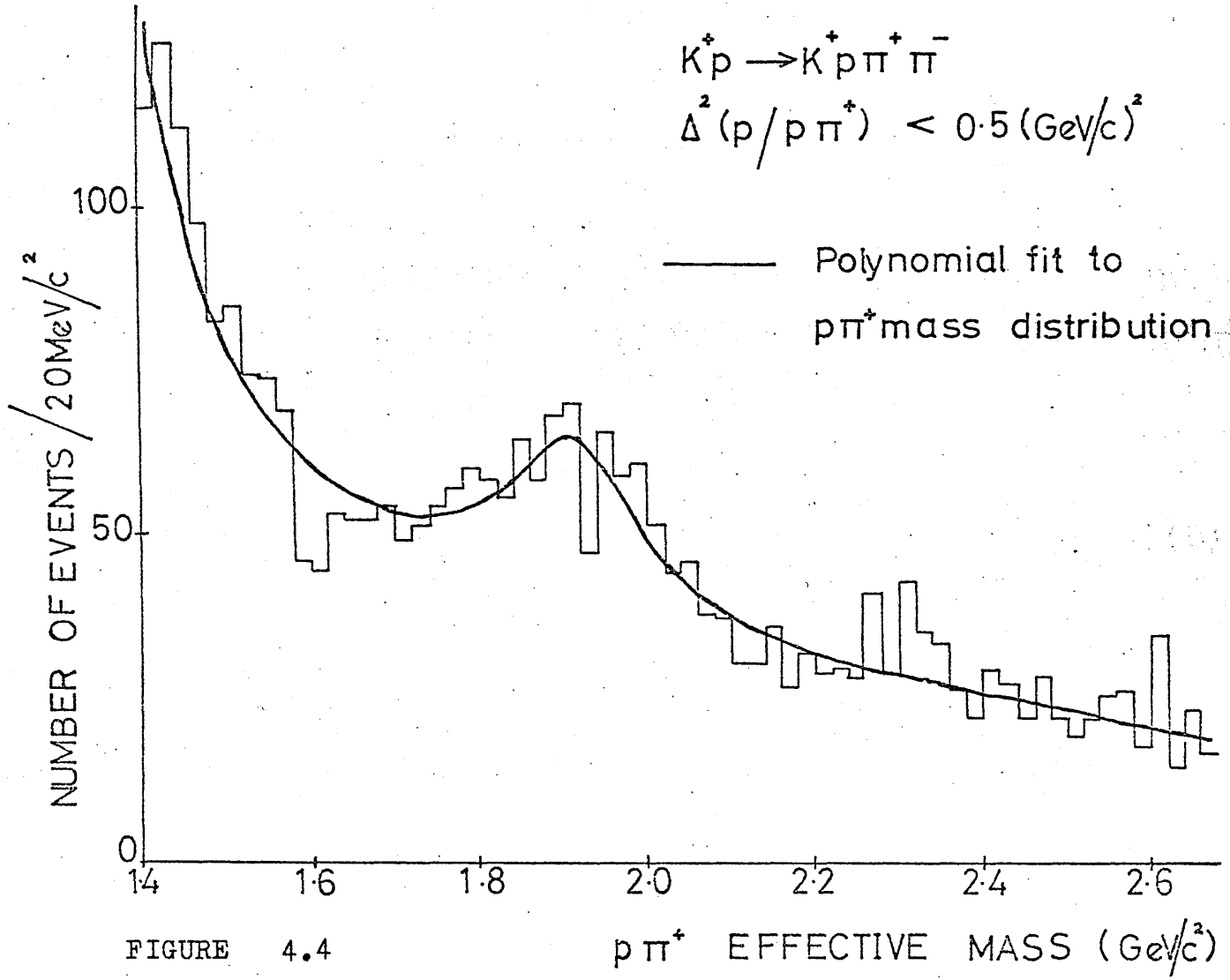
$K^+p \rightarrow K^+p\pi^+\pi^-$
$\Delta^2(p/p\pi^+) < 0.5\,(GeV/c)^2$
Polynomial fit to
$p\pi^+$ mass distribution
NUMBER OF EVENTS /20MeV/c^2
100
50
0
1·4
1·6
1·8
2·0
2·2
2·4
2·6
$p\pi^+$ EFFECTIVE MASS (GeV/c^2)

FIGURE 4.4

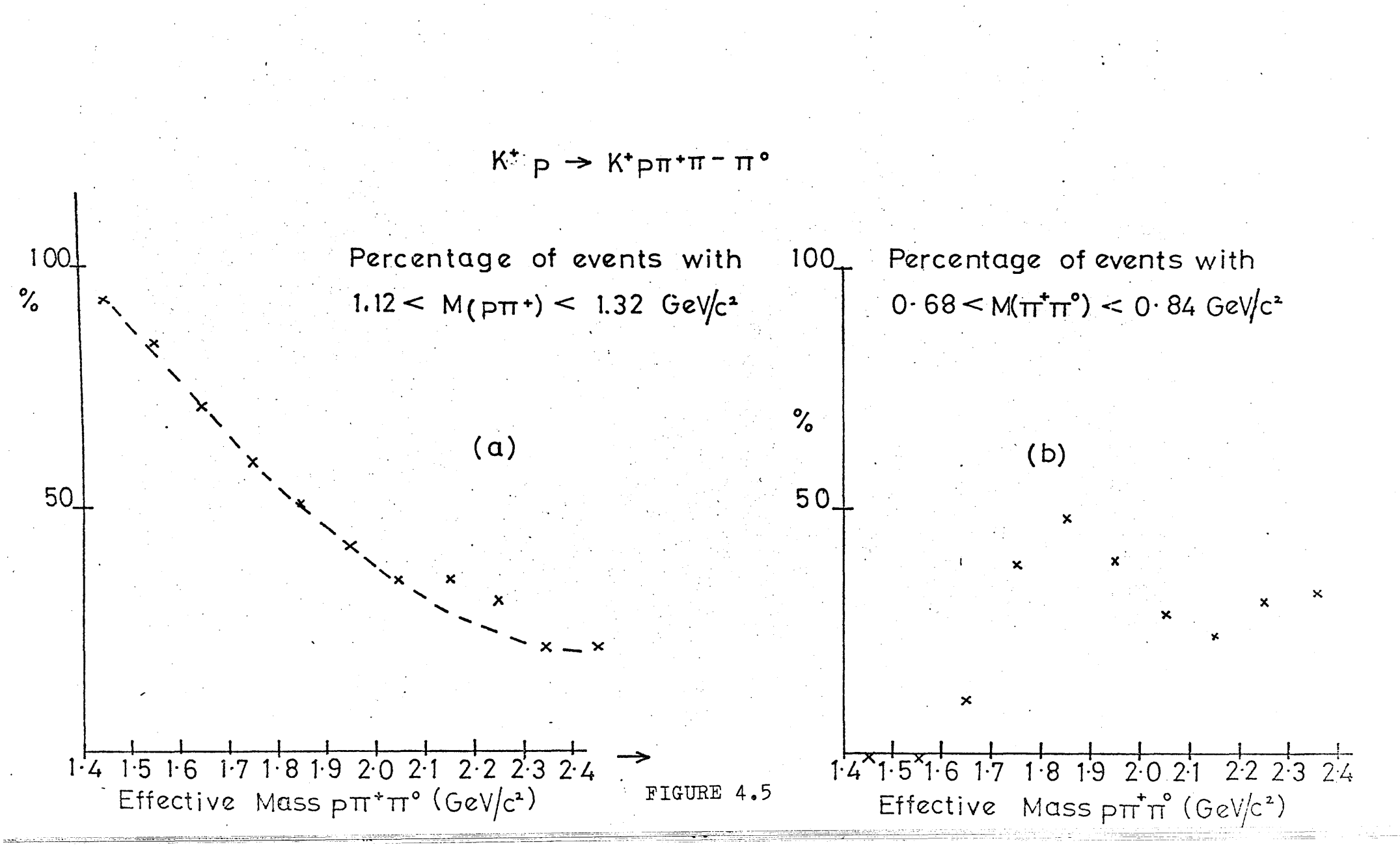
$K^+ p \rightarrow K^+ p\pi^+\pi^-\pi^\circ$
Percentage of events with
$1.12 < M(p\pi^+) < 1.32$ GeV/c²
(a)
100
%
50
1·4 1·5 1·6 1·7 1·8 1·9 2·0 2·1 2·2 2·3 2·4
Effective Mass $p\pi^+\pi^\circ$ (GeV/c²)
Percentage of events with
$0·68 < M(\pi^+\pi^\circ) < 0·84$ GeV/c²
(b)
100
%
50
1·4 1·5 1·6 1·7 1·8 1·9 2·0 2·1 2·2 2·3 2·4
Effective Mass $p\pi^+\pi^\circ$ (GeV/c²)

FIGURE 4.5

$K^+p \longrightarrow K^+p\pi^+\pi^-\pi^0$

$1.8\ GeV/c^2 < M(p\pi^+\pi^0) < 2.0\ GeV/c^2$ (235 EVENTS)

oooo FIT 1 ($\Delta^{++}(1236)$ and $\Delta^+(1236)$ PRODUCTION RELATED BY I-SPIN)

---- FIT 2 (NON-INTERFERING $\Delta^{++}(1236)$ and $\Delta^+(1236)$ PRODUCTION)

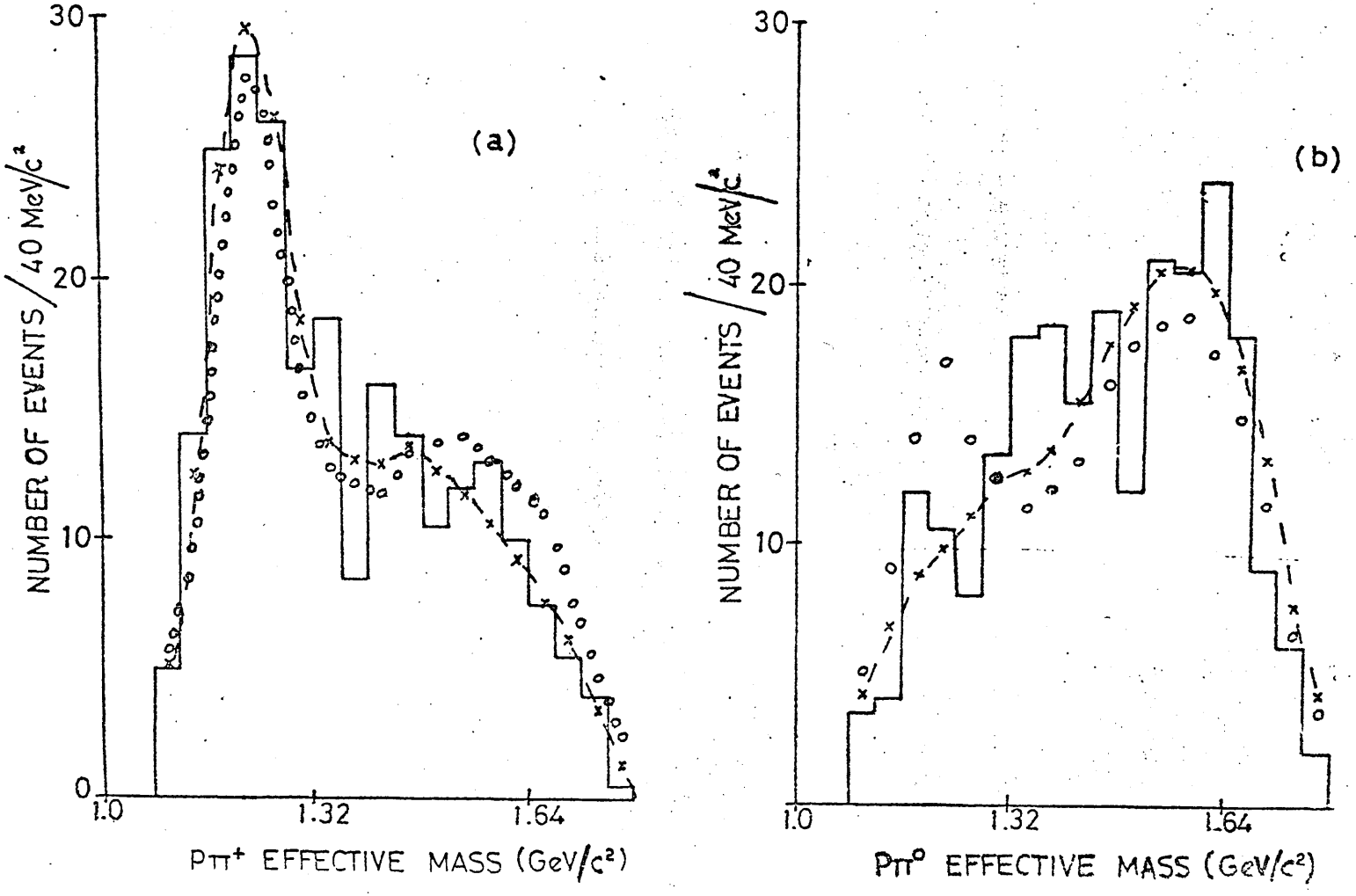

FIGURE 4.6

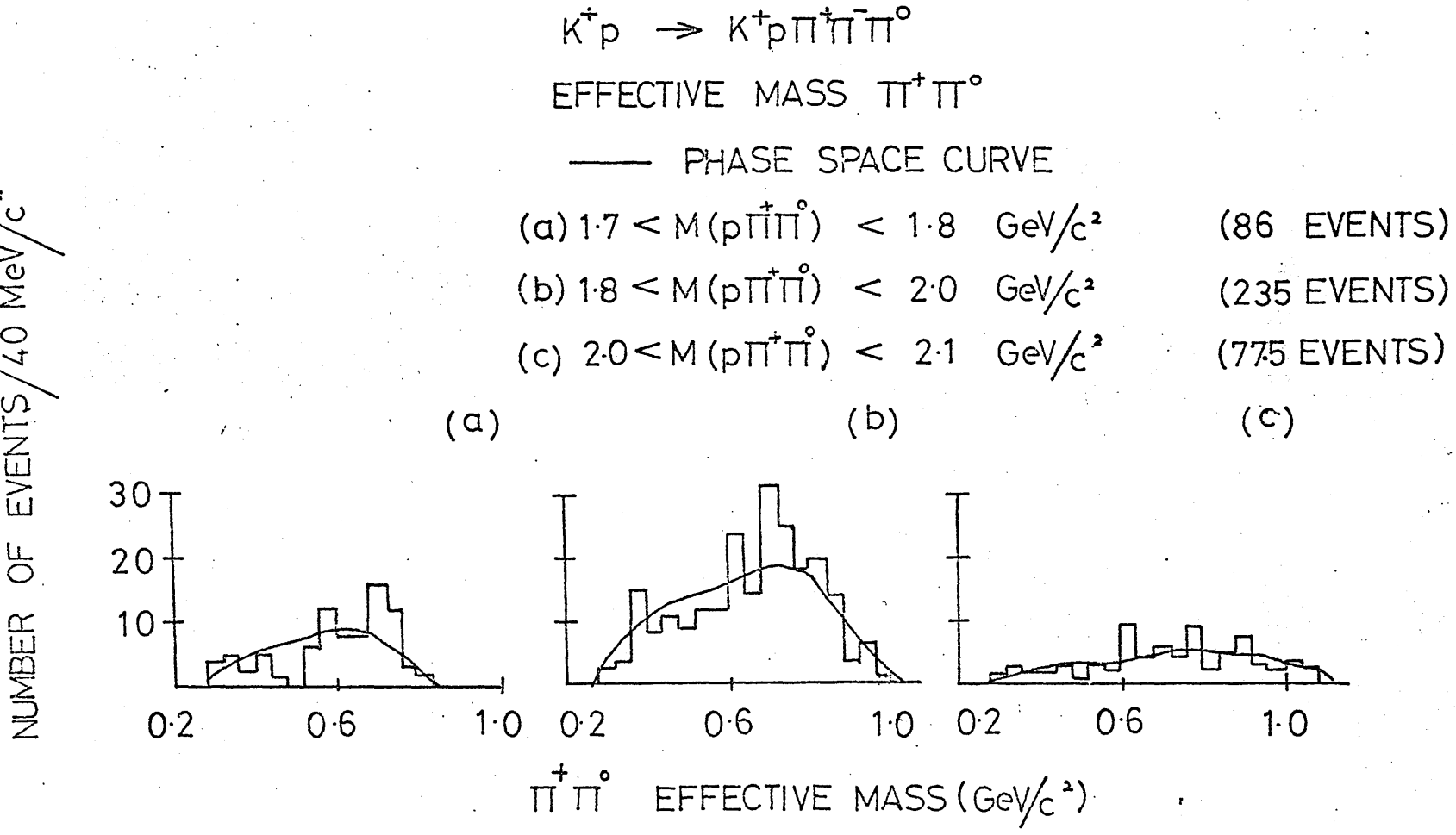
$K^+p \rightarrow K^+p\pi^+\pi^-\pi^\circ$
EFFECTIVE MASS $\pi^+\pi^\circ$
—— PHASE SPACE CURVE
(a) $1.7 < M(p\pi^+\pi^\circ) < 1.8$ GeV/c² (86 EVENTS)
(b) $1.8 < M(p\pi^+\pi^\circ) < 2.0$ GeV/c² (235 EVENTS)
(c) $2.0 < M(p\pi^+\pi^\circ) < 2.1$ GeV/c² (77.5 EVENTS)
(a)
(b)
(c)
NUMBER OF EVENTS/40 MeV/c²
30
20
10
0·2
0·6
1·0
$\pi^+\pi^\circ$ EFFECTIVE MASS (GeV/c²)

FIGURE 4.7

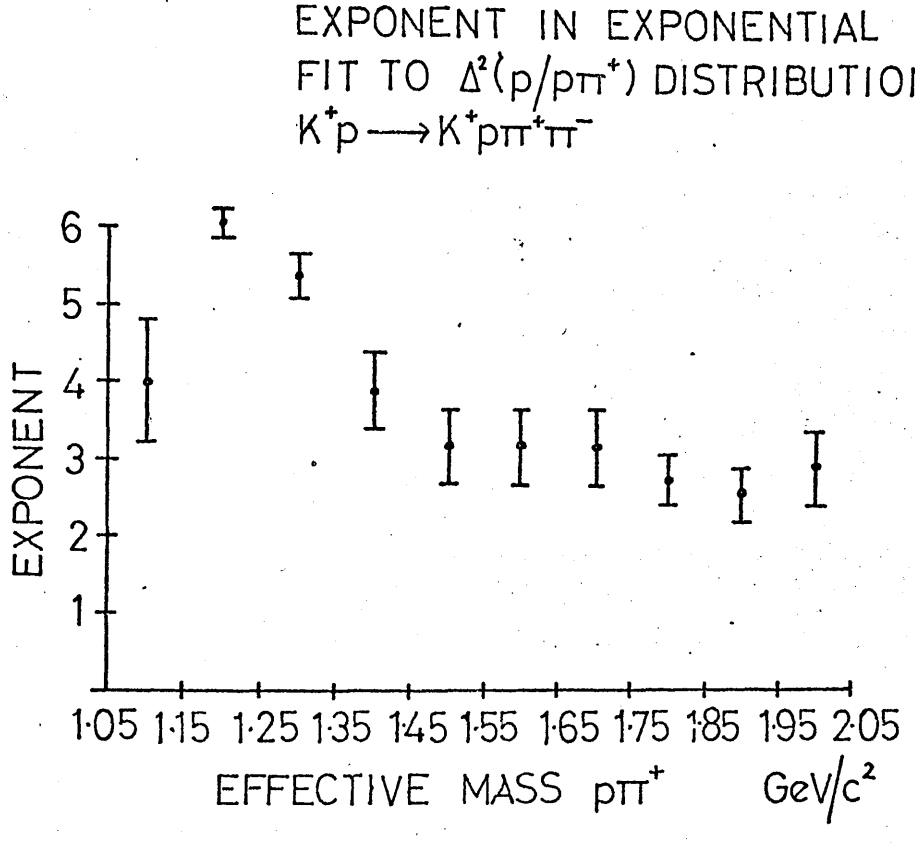
EXPONENT IN EXPONENTIAL
FIT TO $\Delta^2(p/p\pi^+)$ DISTRIBUTION.
$K^+p \longrightarrow K^+p\pi^+\pi^-$
EXPONENT
6
5
4
3
2
1
1·05 1·15 1·25 1·35 1·45 1·55 1·65 1·75 1·85 1·95 2·05
EFFECTIVE MASS $p\pi^+$ GeV/c^2

FIGURE 4.8

Chapter V

Single Particle Distributions

V.1 Introduction

In this chapter, single particle distributions in the 10 GeV/c K^+p experiment are investigated. K^+p experiments provide useful data for the study of momentum distributions, since each 'leading particle' can be identified after the reaction.

Momentum distributions for kaons, protons, and pions are investigated using data from events which have been kinematically fitted. Single particle distributions for neutral K-mesons and negative pions are obtained from the data from events in which the interaction vertex has not been fitted. These distributions correspond to the reactions:

$$K^+p \longrightarrow K^0X^{++} \qquad (1)$$

where the system X^{++} has the quantum numbers of an $I=3/2$ baryon system, and:

$$K^+p \longrightarrow \pi^-X^{+++} \qquad (2)$$

The single particle data is parameterised in terms of the four-momentum-transfer-squared from the incident kaon to the particle, and the effective mass of the system X, following the method of Beaupre et al. (ref. 5.1) which was applied to K^0 production in K^+p interactions at 5 GeV/c and 8 GeV/c. The K^0 results obtained at 10 GeV/c are compared with those of reference 5.1. The negative pion distributions are compared with published K^+p data at 12 GeV/c (ref. 5.2).

V.2 Fitted Momentum Distributions

The Peyrou plots of transverse momentum against longitudinal momentum in the overall centre-of-mass, shown in figure 5.1(a), contain data from the four-constraint reactions:

$$\begin{aligned} K^+p &\longrightarrow K^+p \\ &\longrightarrow K^+p\pi^+\pi^- \\ &\longrightarrow K^+p\pi^+\pi^+\pi^-\pi^- \end{aligned}$$

while figure 5.1(b) shows the data for the reactions with a visible K^o:

$$\begin{aligned} K^+p &\longrightarrow K^op\pi^+ \\ &\longrightarrow K^op\pi^+\pi^+\pi^- \\ &\longrightarrow K^op\pi^+\pi^+\pi^+\pi^-\pi^- \end{aligned}$$

The kaon and proton centre-of-mass longitudinal momenta are peaked in the same direction as the incident particles, as expected. The pions have low centre-of-mass longitudinal momentum. There is a forward tendency of the π^+ in figure 5.1(b) for K^o production (where $K^{*+}(890)$ production involving the π^+ is possible) relative to the isotropic distribution in figure 5.1(a).

The average transverse momentum for the protons and kaons (both charged and uncharged) is independent of multiplicity, but is greater than the average transverse momentum of the pions (which is also independent of multiplicity). The transverse momenta, averaged over the reactions above are:

PARTICLE	TRANSVERSE MOMENTUM (GeV/c)
Proton	0.44
Kaon	0.43
Pion(-ve)	0.34
Pion(+ve)	0.33

The variation with multiplicity of the longitidunal centre-of-mass momentum for kaons and protons is pronounced, and is shown in figure 5.2. The proton momentum decreases linearly with increasing multiplicity, independently of whether K^+ or K^o is produced in the reaction. This linear decrease of proton longitudinal momentum with increasing multiplicity (from two to seven prongs) has not been previously observed.

V.3 The Reaction $K^+p \rightarrow K^oX^{++}$

The data on this reaction uses the V^o events in which the decay vertex fits a K^o decay hypothesis. No attempt at fitting the interaction vertex was made. The data, therefore, includes events in which unseen neutral particles are produced. The chamber weighting, described in Chapter II, was used to correct for K^o's decaying outside the fiducial volume.

Table 5.1 shows the cross-section for K^o production along with two, four, six, and eight charged particles, and an undetermined number of unseen neutrals. The data at 10 GeV/c is from Chapter II, and the other data is from ref. 5.1.

The individual two, four, and six prong K^o cross-sections

vary considerably between 5 and 10 GeV/c, but the total cross-section for K^o production, which is the sum of these, remains remarkably constant around 5.7 mb, which is 1/3 of the total K^+p cross-section.

V.4 The Reaction $K^+p \rightarrow \pi^- X^{+++}$

The negative particles produced in a K^+p experiment yield a comparatively pure sample of negative pions. The contamination can be estimated by considering the cross-section for production of pairs of strange particles, relative to the cross-section for producing pion pairs, e.g. the reactions:

$$K^+p \longrightarrow K^+p\pi^+\pi^-$$
$$K^+p \longrightarrow K^+pK^+K^-$$

have cross-sections of 1317μb and 43μb (ref.2.4). Using data from negative tracks from unfitted events should give a sample of negative pions containing less than 5% contamination from negative kaons.

The total cross-section for negative pion production in 10 GeV/c K^+p interactions is 11.41 mb ($\pm$ 0.9). Data from four and six prong events was available. The cross-section for negative pion production from eight prong events is only 5.5% of the total cross-section (see Table 2.2), and so the omission of eight prong data from the distributions should not have an appreciable effect.

V.5 Parameterisation of Single Particle Data

The value of parameterising the data is that comparisons

between experiments at different energies can then easily be made, in order to investigate scaling behaviour of the variables involved. It is important that standard methods are used. Published data already exists for K^o distributions in K^+p experiments at 5GeV/c and 8.2 GeV/c (ref. 5.1) and for negative pion distributions in a K^+p experiment at 11.8 GeV/c (ref. 5.2)

To describe single particle production completely, two independent variables are required. The four-momentum-transfer-squared (t) from the incident particle to the single particle considered, and the effective mass (M) of the recoil system, is one such pair of variables. Alternatively, the longitudinal and transverse momenta (p_L and p_T) of the particle can be used.

V.6 Mass Distributions

The mass spectra for system X from the reactions (1) and (2) are illustrated in figure 5.3. Over most of the kinematically allowed region above about 2 GeV/c^2, the cross-section rises exponentially to its peak value. Fitting an exponential of the form:

$$\frac{d\sigma}{dM} = \sigma \exp(kM) \qquad (5.1)$$

to the range of the mass spectrum shown in figure 5.3 gives the curves of figures 5.4(a) and 5.5(a). Table 5.2 shows the fitted parameter values and errors, and the effect on the distributions of applying a cut on t' ($t' = |t - t_{MIN}|$) where t = the four-momentum-transfer-squared from the incident kaon, and t_{MIN} is the minimum possible |t|-value for the effective mass M. The values from reference 5.1 are included in Table 5.2 for comparison.

While the sharpness of the exponential peak of the mass distribution for reaction (1) decreases substantially between beam momenta of 5 GeV/c and 8.2 GeV/c, the values at 8.2 GeV/c and 10 GeV/c are, within experimental error, identical. The mass distribution for reaction (2) is more peaked than for reaction (1): in reaction (2), fragmentation of either the target proton or the incident kaon into the system X^{+++} (which has quantum numbers $B = 1, S = 1$) is suppressed (ref. 5.3). X^{+++} is therefore most likely to contain fragmentation products of both target and beam, which will be moving rapidly apart in the overall centre-of-mass system, and therefore the effective mass distributions will be peaked towards high values. In reaction (1), the system X^{++} ($B = 1, S = 0$) is a favoured fragmentation product of the target proton, and it is possible therefore that this system will sometimes contain fragmentation products of the proton only, which will tend to have lower effective mass. The same qualitative behaviour of the mass spectra would also be expected from a multi-Regge picture.

V.7 Four-Momentum-Transfer-Squared Distributions

The t' distributions ($t' = |t - t_{MIN}|$) from the incident kaon to the K^0 and π^- of reactions (1) and (2) are shown in figure 5.6. Figure 5.7 shows the t' distributions for three 500 MeV/c wide bands of X^{++} mass in reaction (1). The straight line represents an exponential fit, from $t' = 0$ to $t' = 1$ $(GeV/c)^2$, to each distribution. It can be seen that these fits also describe the data reasonably well out to

$t' = 2.0$ $(GeV/c)^2$. The t' distributions for events lying in narrow mass bands 100 MeV/c^2 wide over the range $2.1 < M(X^{++}) < 4.0$ GeV/c^2 (reaction (1)) and $3.0 < M(X^{+++}) < 4.1$ GeV/c^2 (reaction (2)) were fitted to exponential functions of the form:

$$\left(\frac{d\sigma}{dt}\right)_{M=const} = \sigma_t(M)\exp(-At') \qquad (5.2)$$

For reaction (1), the t' distribution out to $t' = 1$ $(GeV/c)^2$ was fitted, but for reaction (2), where the t' distribution is less sharply peaked, the fitted range extended to $t' = 2$ $(GeV/c)^2$. The slope parameter, A, is shown, as a function of mass, M, in figure 5.8, for both reactions. A function of the form:

$$A = CM^{-\alpha} \qquad (5.3)$$

was fitted to the slope parameter values for each reaction, as in reference 5.1. The experimental distribution from reaction (1) appears to have some structure, and so the fit represents only the average behaviour over the range. The values obtained for C and α are:

$K^+p \longrightarrow K^\circ X^{++}$ $\quad C = 32$ $\quad \alpha = 2.5$

$K^+p \longrightarrow \pi^- X^{+++}$ $\quad C = 3860$ $\quad \alpha = 6.4$

The values for the K° reaction agree with those quoted in reference 5.1, ($C = 26, \alpha = 2.3$), which were obtained from the combined data from the K^+p experiment at 8.2 GeV/c, and a K^-p experiment at 10.1 GeV/c.

The full parameterisation is obtained by combining expressions (5.2) and (5.3), which give the differential

The full parameterisation of the data in terms of M and t' can now be expressed as:

$$\frac{d^2\sigma}{dt'dM} = \sigma^- c M^{-\alpha} \frac{\exp[kM - cM^{-\alpha}t']}{1 - \exp(-cTM^{-\alpha})} \quad (5.4)$$

where $T = 1$ $(GeV/c)^2$ for reaction (1)

$T = 2$ $(GeV/c)^2$ for reaction (2)

M is the recoil effective mass

t' is the difference between the four-momentum-transfer-squared from the incident kaon to the particle, and the minimum possible four-momentum-transfer-squared for effective mass M.

The other parameters have been defined and evaluated previously.

This parameterisation is obtained by combining expressions (5.2) and (5.3), which give the differential t' cross-section for each mass value, with expression (5.1) containing the differential effective mass cross-section.

Formula (5.4) is valid over the ranges:

$0 < t' < 1$ $(GeV/c)^2$

$2.1 < M(X^{++}) < 4.0$ GeV/c^2 (reaction 1)

$0 < t' < 2$ $(GeV/c)^2$

$3 < M(X^{+++}) < 4.2$ GeV/c^2 (reaction 2)

The majority of events is contained within these ranges.

V.8 Longitudinal Momentum

The Feynman x variable ($x = \frac{2p_L}{\sqrt{s}}$) distribution for

reactions (1) and (2) is shown in figure 5.9. The distribution is peaked at x=0, as observed in other experiments. Exponential functions, exp (-B x),fit this distribution well, on either side of x = 0. The distribution is asymmetric, with a sharper fall towards negative values of x than towards positive values. The negative side of the distribution, from p_L= -1.0 to p_L= 0 (i.e. x= -0.448 to x = 0) gave the parameters:

41 mb (± 0.9), B = 9.30 (±0.16)

This compares with the values

$\sim$ 40 mb, B = 10.6 (±0.7)

from the fit to the backward π^- spectrum in K^+p data at 11.8 GeV/c (ref. 5.2). The corresponding fits for the forward part of the distribution (fitted from x = 0.0 to x = 0.448) are:

40 mb (±0.8), B=6.09 (±0.1)

compared with: $\sim$40 mb B=7.0 (±0.5) at 11.8 GeV/c

Comparing the numbers at 10 GeV/c (centre-of-mass energy 4.46 GeV) and at 11.8 GeV/c (centre-of-mass energy 4.8 GeV) indicates a trend towards stronger peaking of the π^- x-distribution about x=0 as beam momentum increases. For reaction (1), the K^o distribution peaks at around x = 0.2, and has a rounded maximum, rather than the sharp peak of the distribution in reaction (2). The sides of the K^o distribution (over the ranges $-1 < p_L \leq 0$, and $0.5 \leq p_L \leq 2.0$, or $-0.448 < x < 0.0$,

$0.224<x<0.896$) fitted to the exponentials gave the values:

$7.95\ (\pm 0.25)$mb, $B=6.65\ (\pm 0.18)$ for $x<0$ and

$19.3\ (\pm 0.68)$mb, $B=3.32\ (\pm 0.07)$ for $x>0$. The authors of reference (5.1) have not performed a similar fit to their data. However, superimposing a curve to represent the 10 GeV/c K^+p data on figure 4 of reference (5.1) gives an approximate comparison. The slight trend towards steeper exponential slopes which is discernable in figure 5.10 for the K^+p data at 8.2 GeV/c, compared with the 5 GeV/c data, continues when the beam momentum is increased to 10 GeV/c. The energy independence for $d\sigma/dx$ mentioned in references 5.1 and 5.2 does not, therefore, seem to hold accurately, at least in K^+p interactions between 5 and 11.8 GeV/c , for π^- and K° distributions. Comparison with data from the 16 GeV/c K^+p (ref. 5.4) experiment, when this becomes available, should help to clarify this.

The Feynman variable, $f(x, p_T)$, (see Chapter I) was also investigated. It was found that, as in reference (5.2), $\frac{df}{dx}(x, p_T)$ was not independent of p_T (i.e. $f(x,p_T)$ cannot be factorised into $g(x) \times h(p_T)$ for π^- or K° distributions. The $f(x,p_T)$ distributions for K° and π^- from reactions (1) and (2) are shown in figure 5.11, integrated over p_T. It was found that an exponential function of x did not fit these distributions satisfactorily. Confirmation of the scaling behaviour of x for the $f(x,p_T)$ distribution will depend on data at other beam momenta (in a suitable form for comparison) becoming available.

V.9 Conclusions

Momentum spectra from events which have been kinematically fitted, show that the 'leading particle' behaviour which is observed in longitudinal momentum distributions may also be exhibited, though in a much less pronounced way, in the transverse momentum distributions.

Inclusive data for π^- and K^o production in K^+p interactions at 10 GeV/c, when compared with π^- data at 11.8 GeV/c, and K^o data at 5 and 8.2 GeV/c, suggests that the distribution in the Feynman variable x is not energy independent at these energies.

The cross-section for K^o production in K^+p interactions is, however, constant within experimental error between beam momenta of 5 and 10 GeV/c, and equal to 1/3 of the total K^+p cross-section.

To establish the validity of Feynman's ideas mentioned in Chapter I, data at different beam momenta relating to the Feynman 'ϕ' variable is needed, presented in a manner which allows comparisons between different experiments.

References

5.1 J.V.Beaupre et al.

Nuclear Physics B30,381 (1971)

5.2 W.Ko and R.Lander

Physical Review Letters 26,1064 (1971)

5.3 S.Y.Lo and K.K Phua

University of Glasgow Preprint

'Selection Rules for Inclusive Reactions'

5.4 Birmingham-Bruxelles-CERN-IPN collaboration

	10 GeV/c	8.2 GeV/c	5 GeV/c
	mb	mb	mb
$\sigma_{TOT}(K^+p)$	17.3(±.1)	17.2(±.1)	17.2(±.2)
$\sigma_{INEL}(K^+p)$	14.0(±.4)	13.8(±.3)	13.6(±.3)
TOTAL X-SECTN. FOR K^o PRODUCTION	5.65(±.37)	5.76(±.33)	5.76(±.21)
2-PRONG WITHOUT K^o	5.50(±.11)	-	-
2-PRONG WITH K^o	2.86(±.21)	3.09(±.21)	4.24(±.20)
4-PRONG WITHOUT K^o	4.70(±.18)	-	-
4-PRONG WITH K^o	2.31(±.11)	2.40(±.15)	1.48(±.12)
6-PRONG WITHOUT K^o	1.45(±.09)	-	-
6-PRONG WITH K^o	.44(±.04)	.27(±.05)	0.04(±.01)
8-PRONG WITHOUT K^o	.18(±.02)	-	-
8-PRONG WITH K^o	.04(±.01)	.002(±.001)	-

Total and partial cross-sections for K^o production, and for events without K^o (where figures available) from 10 GeV/c K^+p, compared with data from reference 5.1 for K^+p at 8.2 GeV/c and 5 GeV/c

TABLE 5.1

REACTION	MASS RANGE GeV/c^2	t' RANGE $(GeV/c)^2$	σ $(\mu b/GeV/c^2)$	k $(GeV/c)^{-1}$
$K^+p \to \pi^- X^{+++}$	3.0-4.2	ALL	.0121($\pm$.006)	2.91($\pm$.14)
(10 GeV/c)		0.0-2.0	.0201($\pm$.005)	3.27($\pm$.07)
$K^+p \to K^o X^{++}$	2.08-3.76	ALL	10.1 ($\pm$1.5)	1.75($\pm$.04)
(10 GeV/c)		0.0-1.0	25.7 ($\pm$5.7)	1.31($\pm$.07)
$K^+p \to K^o X^{++}$	2.0-3.45	ALL	17.1 ($\pm$0.8)	1.70($\pm$.05)
(8.2 GeV/c)		0.0-1.0	44.3 ($\pm$2.1)	1.33($\pm$.05)
$K^+p \to K^o X^{++}$	2.0-2.5	ALL	40.6 ($\pm$2.0)	2.10($\pm$.05)
(5 GeV/c)		0.0-1.0	49.6 ($\pm$2.4)	1.81($\pm$.05)

Parameterisation and errors from fits to mass spectra of system 'X'.

The data at 8.2 GeV/c and 5 GeV/c are from reference 5.1

TABLE 5.2

Figure Captions

5.1 Peyrou Plots (transverse momentum against centre-of-mass longitudinal momentum) for:

(a) K^+, p, π^+, and π^- from two, four and six prong events without V^0

(b) As (a), but for events with associated K^0 decay.

5.2 Average centre-of-mass longitudinal momentum for kaons and protons for two, four and six prong four-constraint fits (with and without V^0), plotted against the number of secondary particles

In the following figure captions, reaction (1) refers to the reaction: $K^+p \rightarrow K^0X^{++}$

and reaction (2) is: $K^+p \rightarrow \pi^-X^{+++}$

5.3 Recoil effective mass for (above) reaction (1)
(below) reaction (2)

5.4 Exponential fits to recoil effective mass for reaction(1)
(above) for all events
(below) for events with $t'(K/K^0) < 1.0$ $(GeV/c)^2$

5.5 As for figure 5.4, but for reaction (2).

5.6 $t'(K^+/K^0)$ distribution for reaction (1) (above), and $t'(K^+/\pi^-)$ distribution for reaction (2) (below).

5.7 Exponential fits to $t'(K/K^0)$ distribution (reaction (1)) for three 500 MeV/c^2 wide recoil mass intervals.

5.8 Slope parameter from exponential fits to t' distributions for reactions (1) and (2), shown as functions of recoil effective mass. The straight lines represent the fits of equation (5.3) to the distributions.

5.9 Feynman 'x' ($=2p_L/\sqrt{s}$) distributions for reactions (1) and (2). The straight lines represent exponential fits to the data

5.10 The Feynman 'x' distribution from the Glasgow 10 GeV/c experiment (reaction (1)), shown as a smooth curve, superimposed on the data contained in figure 4 of reference 5.1. The right-hand diagram contains data from K^+p interactions at 5GeV/c, 8.2 GeV/c and 10 GeV/c, while the diagram on the left shows data from the K^+p experiments at 8 GeV/c and 10 GeV/c, and K^-p data at 10.1 GeV/c.

5.11 Feynman 'f' distribution for reactions (1) and (2)

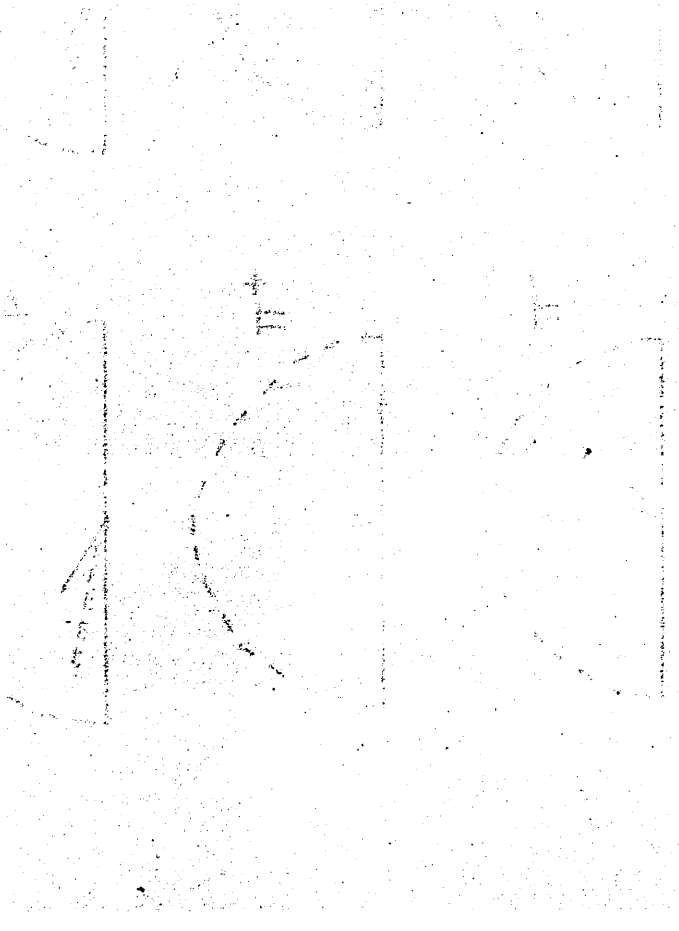

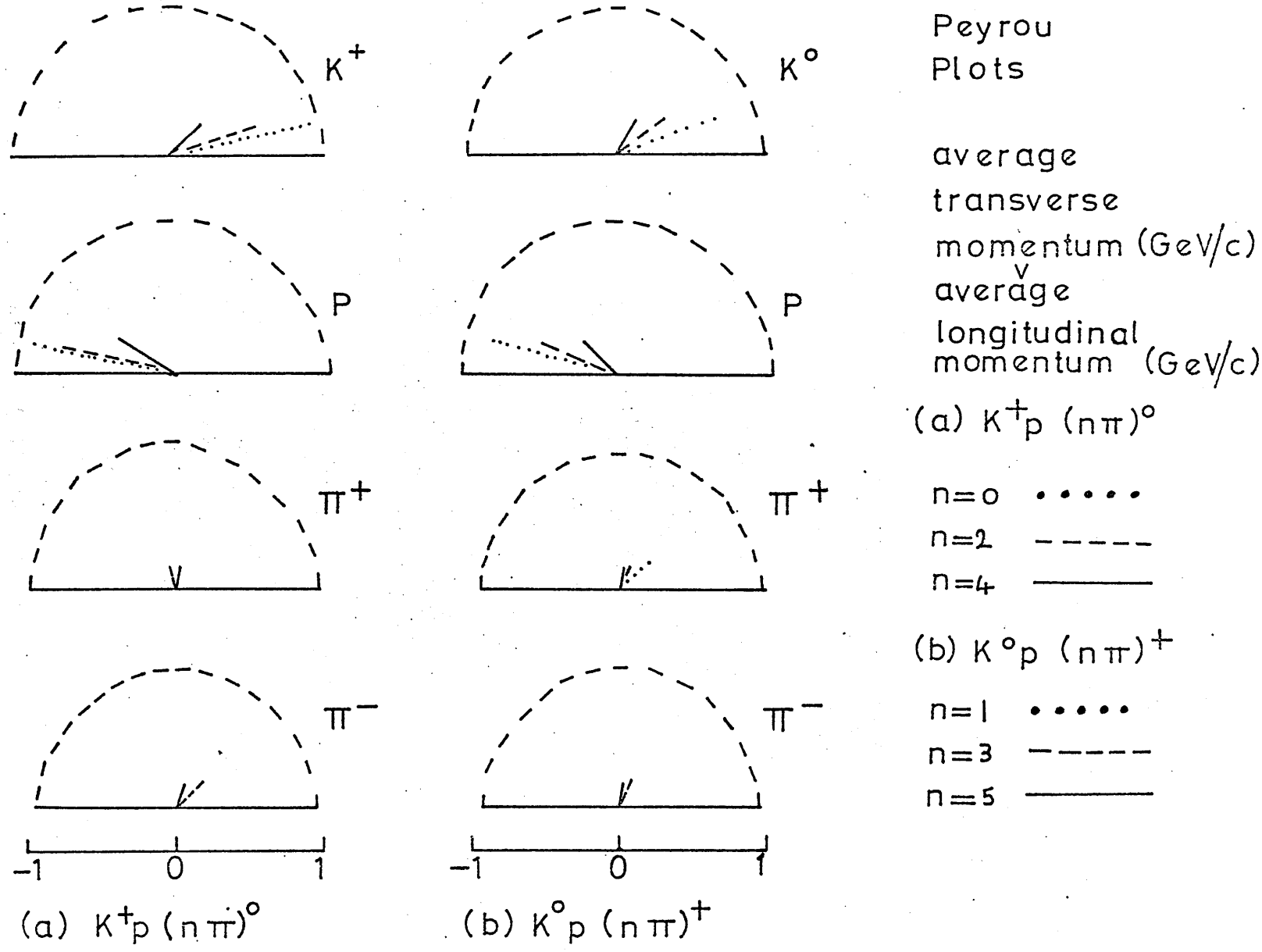
K+
K°
P
P
π+
π+
π−
π−
−1
0
1
−1
0
1
(a) K+p (nπ)°
(b) K°p (nπ)+
Peyrou
Plots
average
transverse
momentum (GeV/c)
average
longitudinal
momentum (GeV/c)
(a) K+p (nπ)°
n=0
n=2
n=4
(b) K°p (nπ)+
n=1
n=3
n=5

FIGURE 5.1

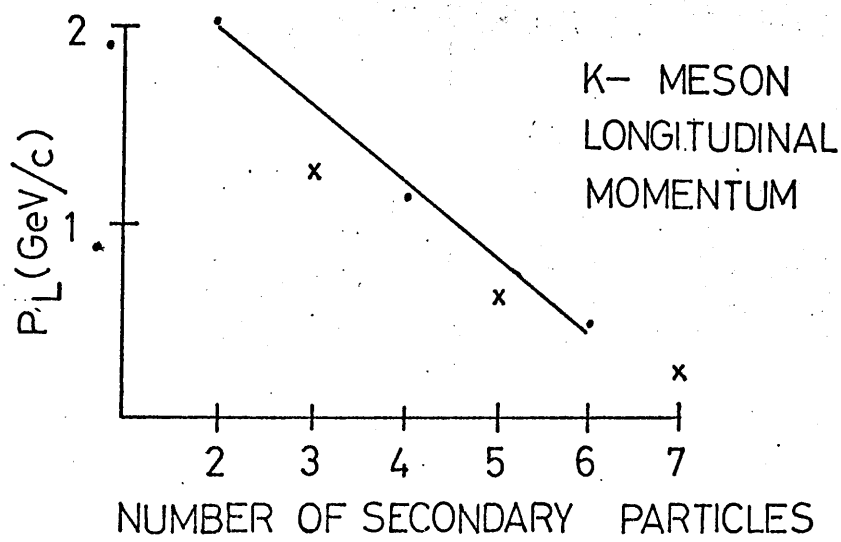

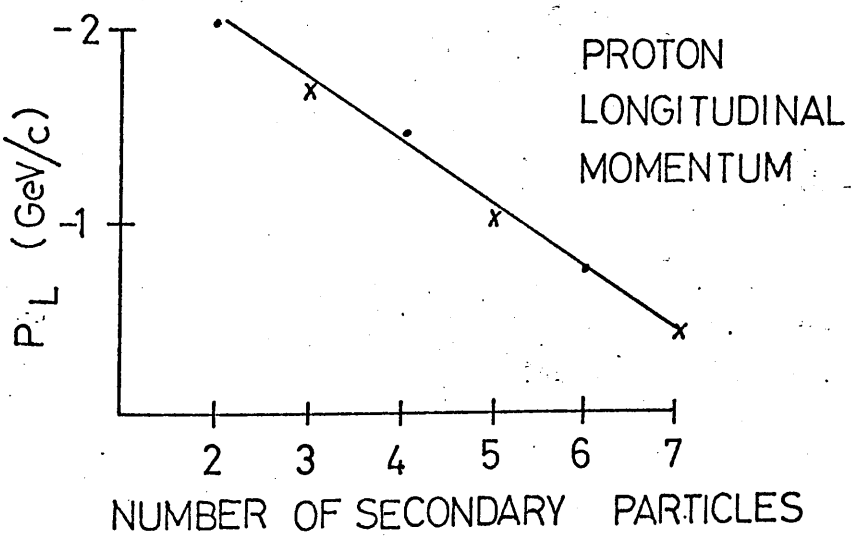

• FOUR CONSTRAINT EVENTS

x SEEN K° DECAY EVENTS

FIGURE 5.2

EFFECTIVE MASS DISTRIBUTIONS.

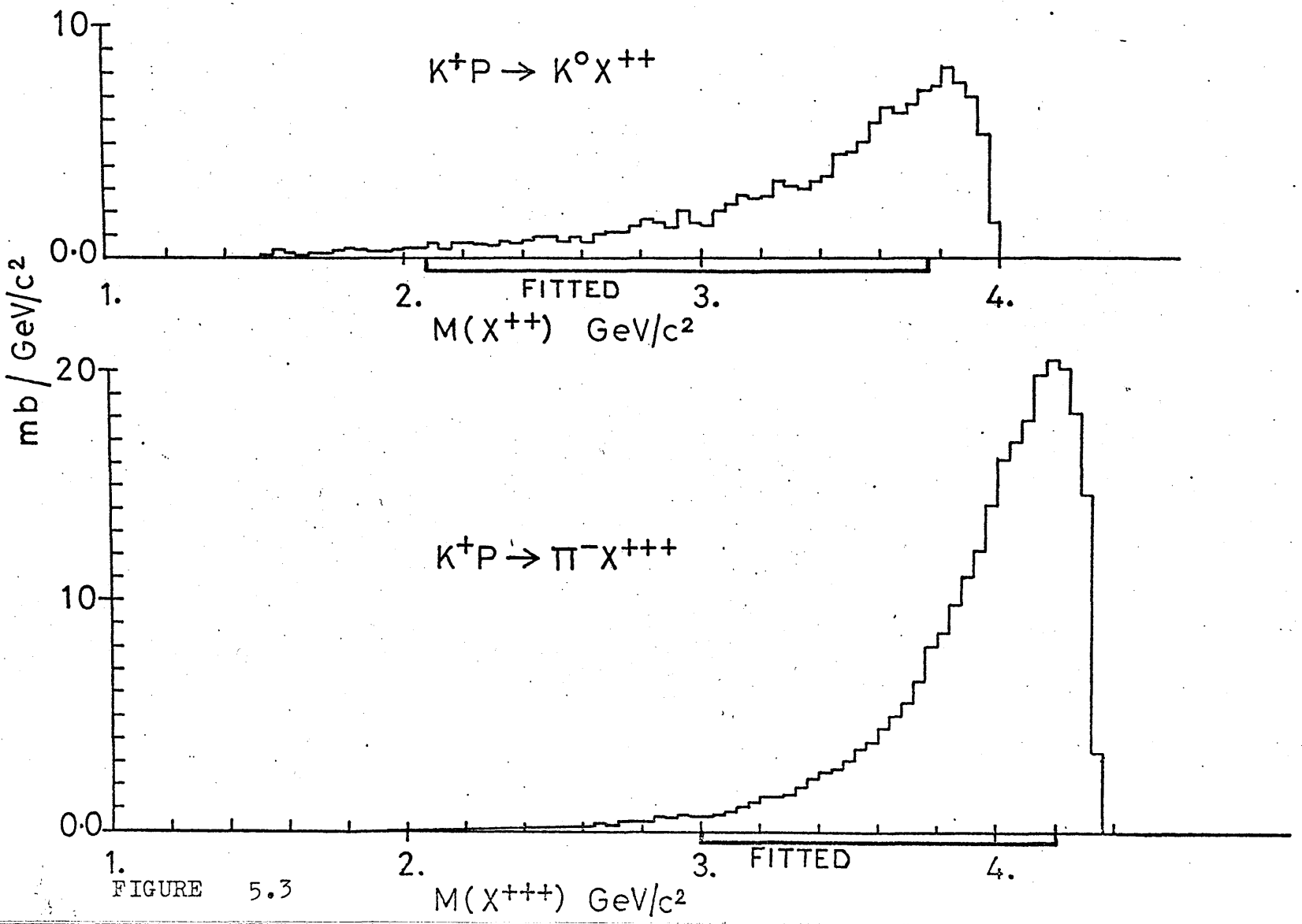

FIGURE 5.3

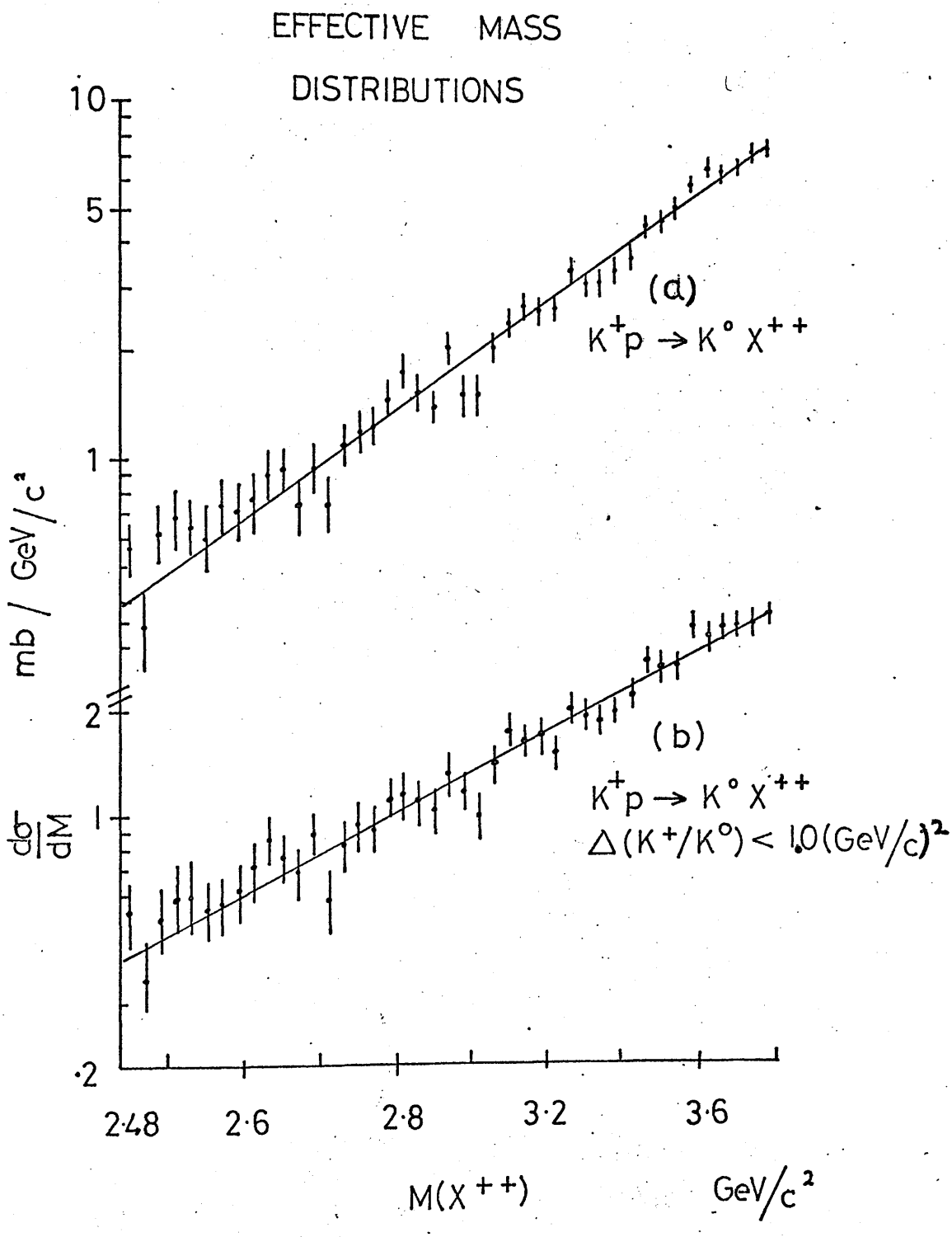
EFFECTIVE MASS
DISTRIBUTIONS
10
5
1
2
1
·2
mb / GeV/c²
dσ/dM
(a)
K⁺p → K° X⁺⁺
(b)
K⁺p → K° X⁺⁺
Δ(K⁺/K°) < 1.0 (GeV/c)²
2·48
2·6
2·8
3·2
3·6
M(X⁺⁺)
GeV/c²

FIGURE 5.4

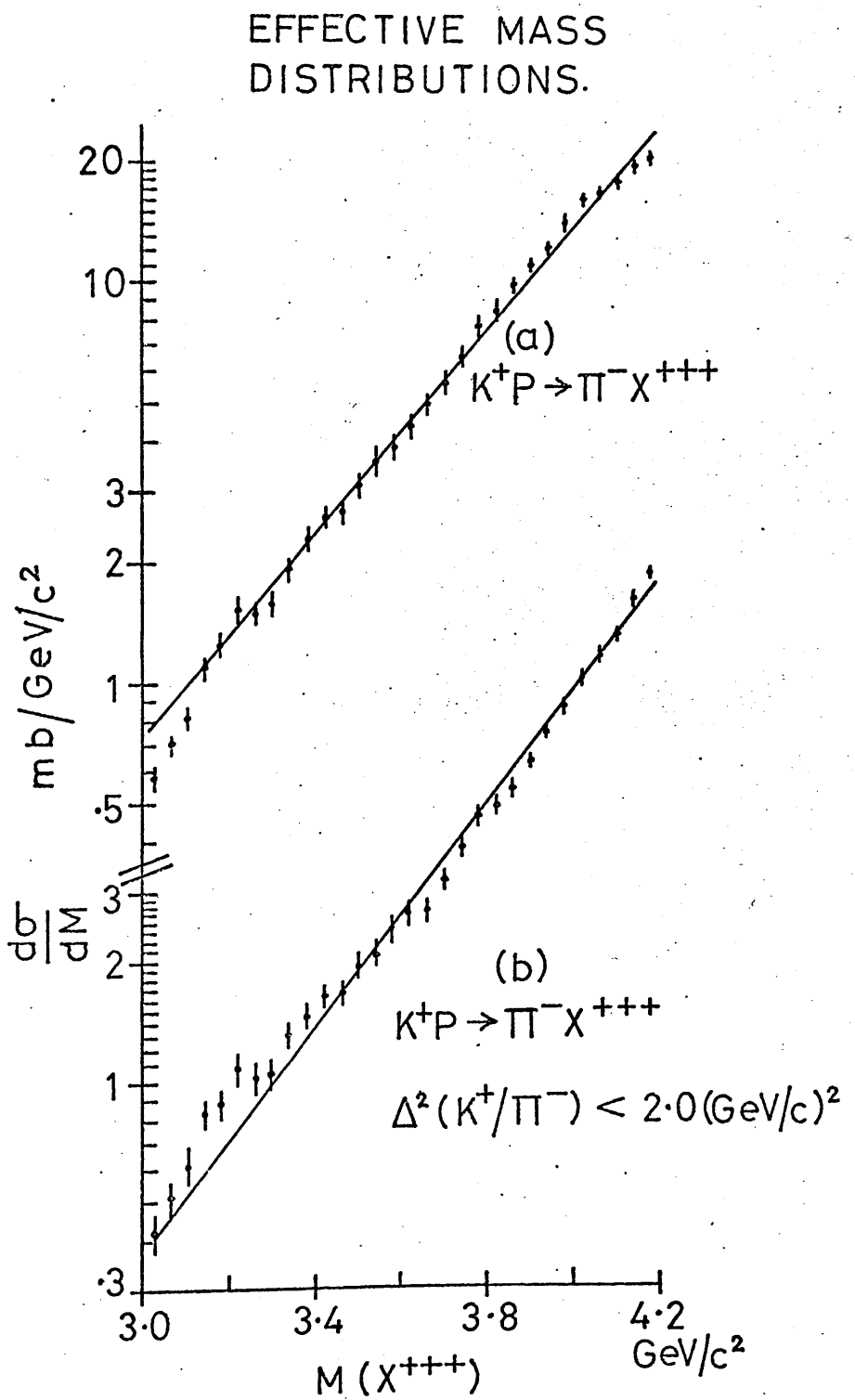
EFFECTIVE MASS
DISTRIBUTIONS.
20
10
3
2
1
·5
3
2
1
·3
mb/GeV/c²
dσ/dM
(a)
K⁺P → π⁻X⁺⁺⁺
(b)
K⁺P → π⁻X⁺⁺⁺
Δ²(K⁺/π⁻) < 2·0(GeV/c)²
3·0
3·4
3·8
4·2
GeV/c²
M(X⁺⁺⁺)

FIGURE 5.5

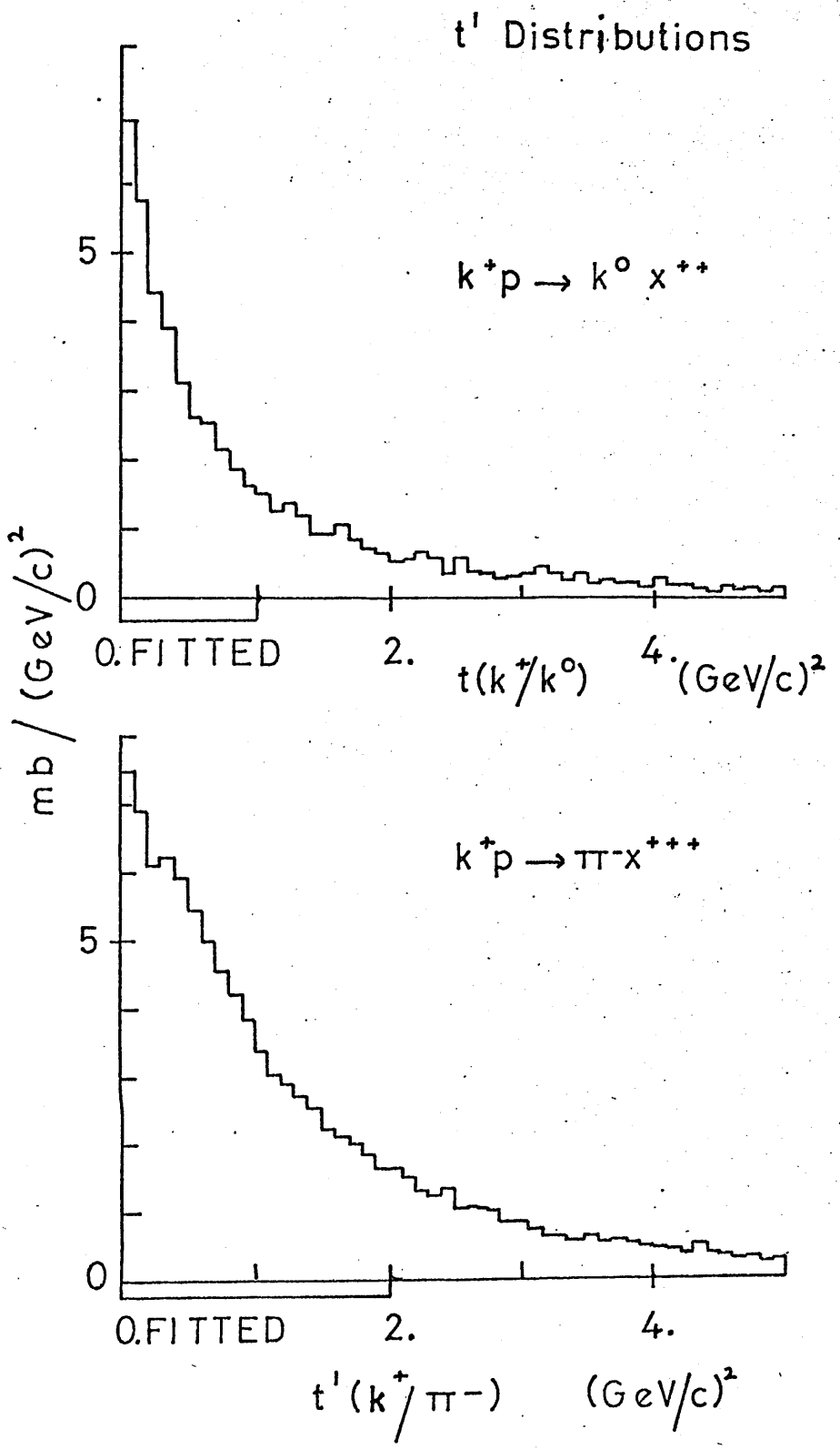
t' Distributions
$k^+p \rightarrow k^o x^{++}$
5
0
0. FITTED
2.
4.
$t(k^+/k^o)$ $(GeV/c)^2$
mb / $(GeV/c)^2$
$k^+p \rightarrow \pi^-x^{+++}$
5
0
0. FITTED
2.
4.
$t'(k^+/\pi^-)$ $(GeV/c)^2$

FIGURE 5.6

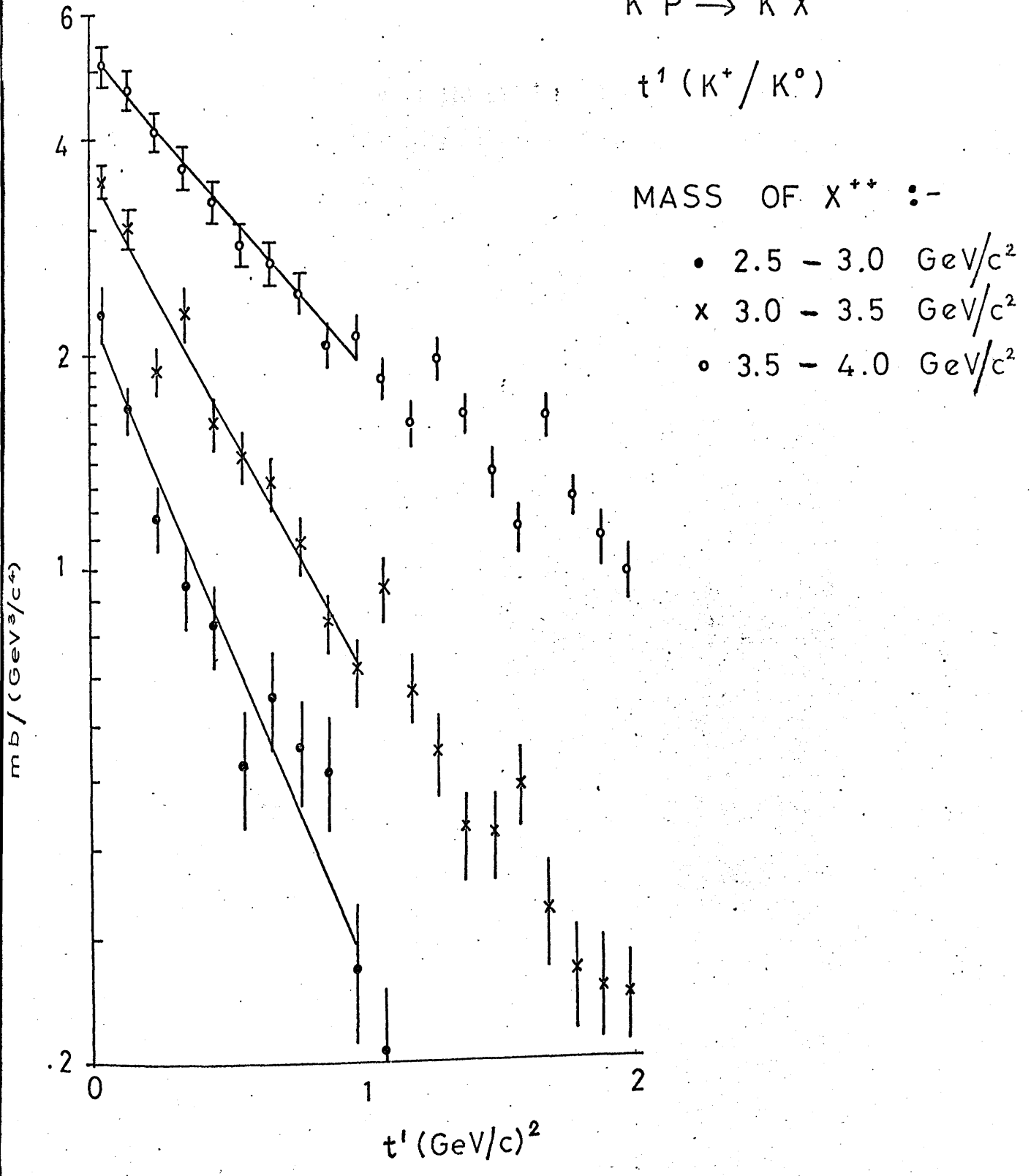
$K^+P \longrightarrow K^\circ X^{++}$
$t^1 (K^+/K^\circ)$
MASS OF X^{++} :-
• 2.5 – 3.0 GeV/c^2
x 3.0 – 3.5 GeV/c^2
o 3.5 – 4.0 GeV/c^2
6
4
2
1
.2
0
1
2
mb/(GeV³/c⁴)
t' (GeV/c)²

FIGURE 5.7

VARIATION OF SLOPE PARAMETER, A,
WITH EFFECTIVE MASS OF X.

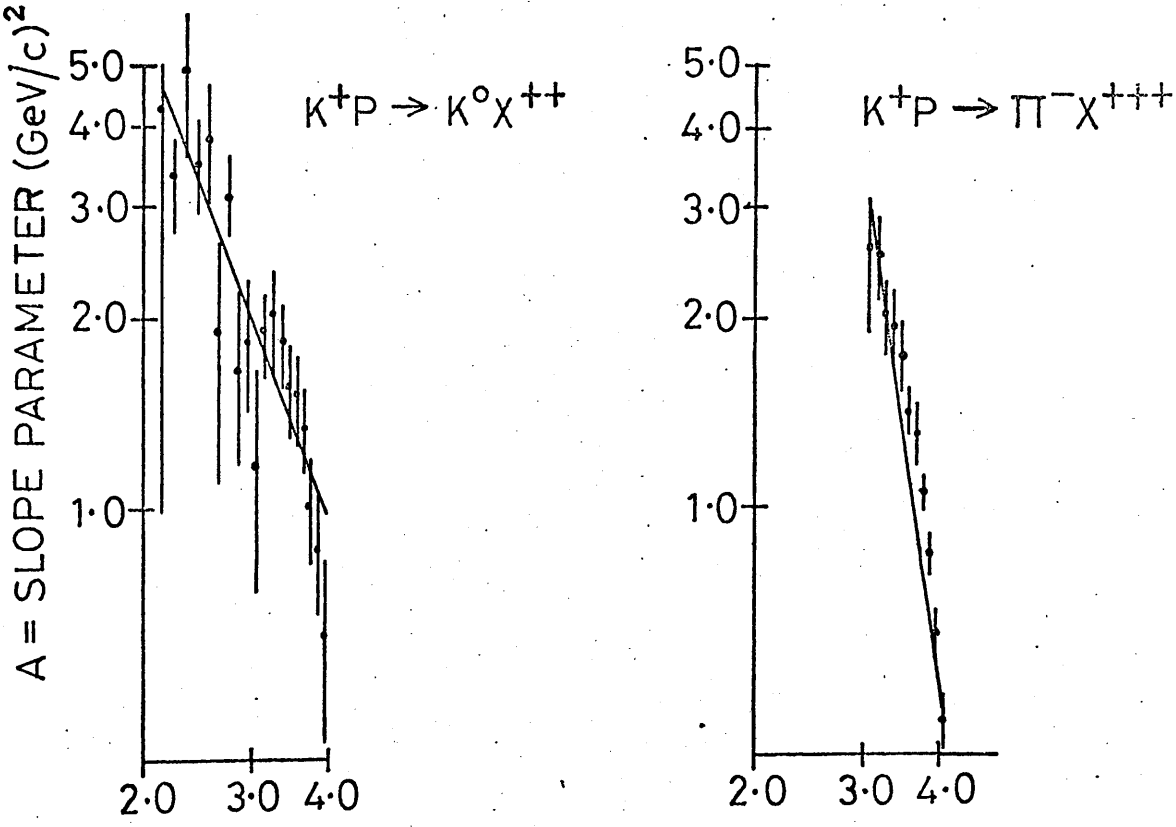

FIGURE 5.8

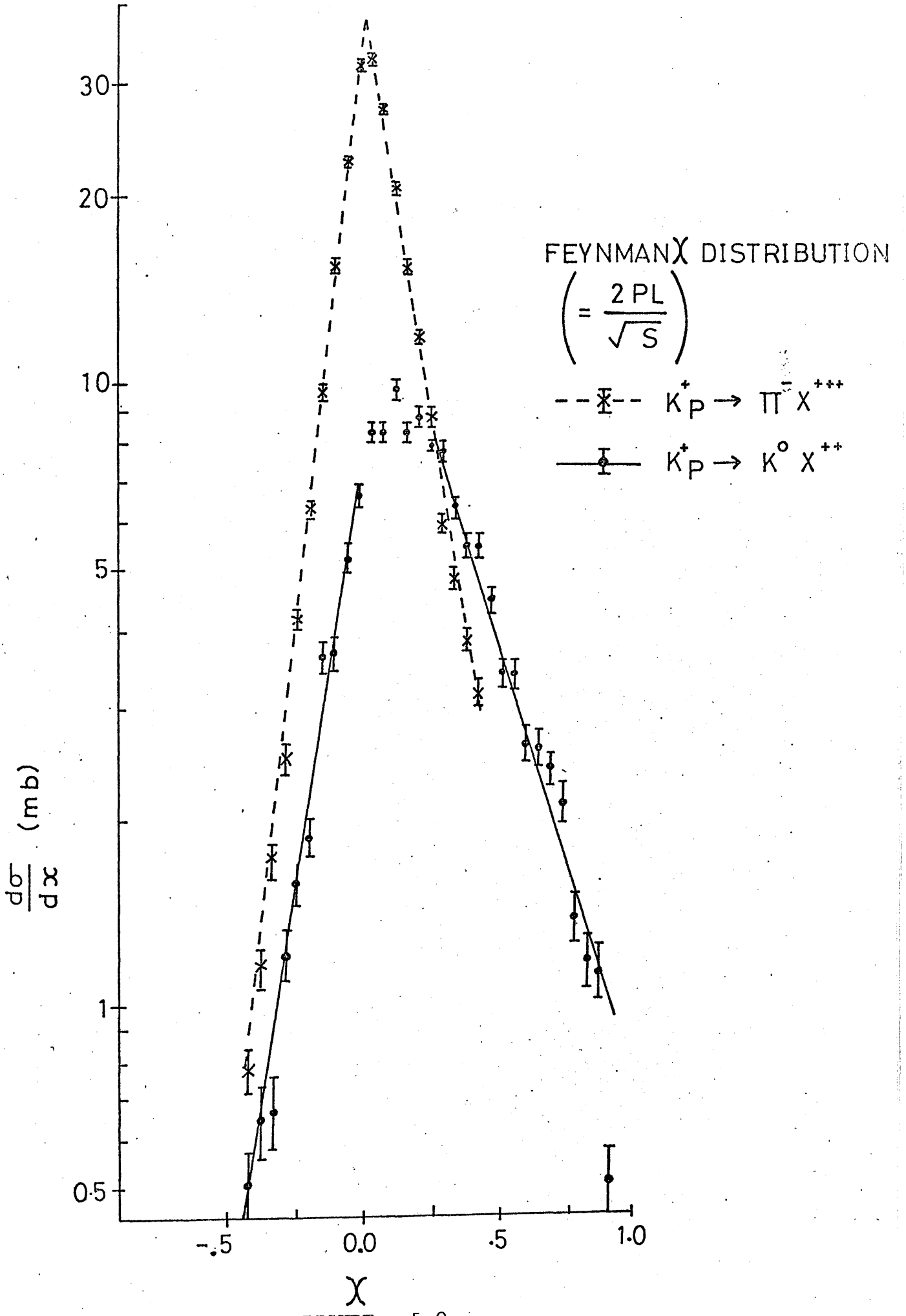
FEYNMAN X DISTRIBUTION
$\left(= \frac{2PL}{\sqrt{S}}\right)$
$K^+P \rightarrow \pi^- X^{+++}$
$K^+P \rightarrow K^\circ X^{++}$
$\frac{d\sigma}{dx}$ (mb)
30
20
10
5
1
0.5
-.5
0.0
.5
1.0
X

FIGURE 5.9

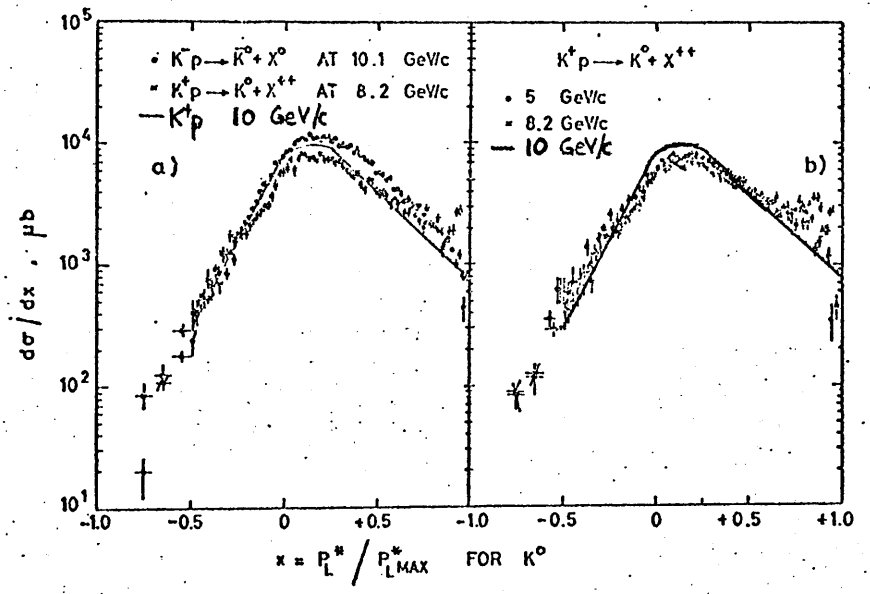
10^5
10^4
10^3
10^2
10^1
$d\sigma/dx$, μb
• $K^-p \rightarrow K^o + X^o$ AT 10.1 GeV/c
▪ $K^+p \rightarrow K^o + X^{++}$ AT 8.2 GeV/c
— K^+p 10 GeV/c
a)
$K^+p \rightarrow K^o + X^{++}$
• 5 GeV/c
▪ 8.2 GeV/c
— 10 GeV/c
b)
-1.0
-0.5
0
+0.5
+1.0
$x = P_L^* / P_{L\,MAX}^*$ FOR K^o

FIGURE 5.10

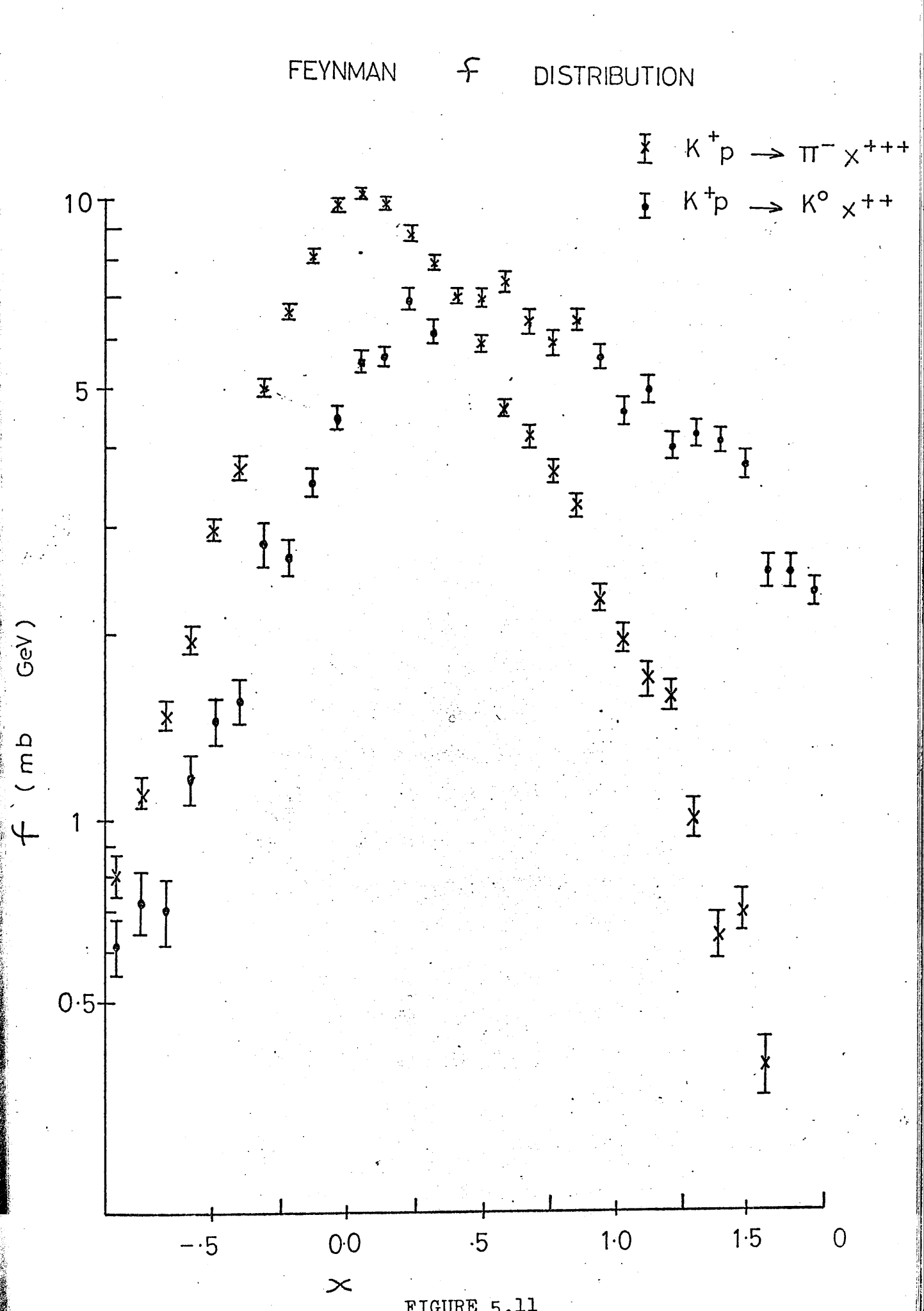
FEYNMAN f DISTRIBUTION
K+p → π− X+++
K+p → K° X++
10
5
1
0·5
f (mb GeV)
−·5
0·0
·5
1·0
1·5
0
x

FIGURE 5.11

Chapter VI

Polly at Glasgow

VI.1 Introduction

The vast increase in the amount of film from bubble chambers in the last decade has necessitated a matching increase in automation of the data handling systems. Several on-line film measuring systems have been developed. Some of these are computer controlled, requiring operator intervention only in certain circumstances, while others are operator guided and use the on-line computer to record and check the measurements.

VI.2 S.M.P. System

The Scanning and Measuring Projector (S.M.P.) was devised in 1960. These machines require an operator, who guides a rotating periscope system (see figure 6.1) along track images projected onto a flexible opaque white blind. The moving track image is detected by a photomultiplier below the bench mark plate, and the position of the track segment obtained by adding the periscope co-ordinates (R,θ) vectorially to the bench mark position. The measuring rate attainable with an S.M.P. machine is of the order of 12 or 13 events per hour. The overall accuracy of the S.M.P. system is of the order of 2 microns on film (ref. 6.1). The 'least count' accuracy for one individual digitising is around 5 microns.

The main disadvantage of the S.M.P. system is the lack of bubble density information. Also, the area of film which can be measured is limited by the area of the bench mark plate.

The digitising periscope is guided by hand, and so the pattern recognition problems in, for example, finding associated charged decays of neutral particles do not occur to the same extent as with computer guided machines.

VI.3 H.P.D. System

The H.P.D. is a fast high precision digitiser. The flying spot, which is produced mechanically from a fixed light source (see figure 6.2), is around 10 to 15 microns in diameter - much smaller than can be obtained from a C.R.T. spot without de-magnification. The film is digitised by moving the film stage perpendicular to the spot trajectory, and measuring the position of the stage after each flying spot line.

The small spot gives high accuracy digitisings, correct to less than 2 microns on film. The overall accuracy of H.P.D. measurements is about one micron. The measuring rate is much higher than for operator dependent machines like the S.M.P.'s - 100 events per hour being the order of magnitude (ref. 6.2).

The main disadvantage is that the tracks must be pre-digitised fairly accurately before measurement, in order that the large number of digitisings obtained from each view may be reduced to those points lying within "roads" which are around 400 microns wide along the tracks of interest. Several scanners and scan tables are devoted to providing pre-digitisings for one H.P.D, and the processing rate for each scan table (roughly ten events per hour) is comparable with the measurement rate of the S.M.P.

The amount of information obtained from digitising one view is large, and therefore a large amount of computer storage is needed to hold this data before the filter programme can reduce it. This problem is particularly acute with the DAPR system, in which all the information from each view from the H.P.D. is stored as input for the pattern recognition programme.

VI.4 P.E.P.R.

The Precision Encoder and Pattern Recognition Device (PEPR) utilises a high precision C.R.T. in which the spot is defocused to form a line segment up to 2mm long. Both the position and direction of tracks can be obtained from P.E.P.R. data.

The measurement rate for P.E.P.R. is roughly of the same order of magnitude as the H.P.D. rate, although as many as 400 events per hour have been measured (on film containing two prong events with vertices pre-digitised, ref. 6.3).

One disadvantage of the line segment sweep in the P.E.P.R. system is the impossibility of extracting ionisation information from the data. A separate scan, in which the C.R.T. spot is focused on the film, is necessary to obtain the bubble density.

VI.5 Polly

Polly is, in concept, similar to P.E.P.R., except that the focused CRT spot is used to scan the film, instead of the line segment used in P.E.P.R. A high precision CRT produces a circular spot which can be deflected to any of 4096 × 4096 major deflection spots on the CRT screen. The spot performs 'slice scans', consisting of up to 128 parallel scan lines, in

any of 32 directions. Digitisings from these scans give the position and width of the track images on film. The Polly software uses the information from previous scans to follow tracks across the film until a vertex is found. The region around the vertex is then searched for tracks radiating out from that point. Secondary tracks are then followed outwards from the vertex. The origional Polly machine (ref. 6.4) at Argonne used pre-scanned film, with vertices pre-digitised to 1mm accuracy. Polly II at Argonne has successfully measured unscanned film ($\bar{p}p$ 2.3 GeV/c film, measuring 2, 4, 6, and 8 prongs) at a rate of between 70 and 100 events per hour (ref. 6.5). The Glasgow Polly will also measure unscanned film, requiring operator assistance only for difficult events. The operation of Polly is slower than P.E.P.R. or H.P.D., due in part to slower hardware. On the other hand, the elimination of pre-scanning and digitising of the film is an important advantage.

Distortions introduced by the use of a C.R.T. must be corrected as far as possible in Polly. This is done in Polly by pincushion correction in the deflection logic, and residual distortion is corrected for by scanning a rectangular grid and fitting a fifth order polynomial correction factor to the measurements of the grid.

The accuracy is estimated at around 2 microns on film for the Argonne Polly machines.

VI.6 Polly at Glasgow

The Polly measuring machine at Glasgow is based on the Polly II device at Argonne, with some alterations. These were necessitated by the following factors:

(a) Pictures from the CERN 2m HBC are larger than the film being measured at Argonne.

(b) At CERN, the three views of the bubble chamber necessary for geometrical reconstruction of the tracks are mounted on separate rolls of film, while in Argonne the views are mounted sequentially on one roll.

(c) Argonne Polly is linked to a Sigma 7 computer, while the Glasgow Polly shares an IBM 360/44 machine, and an IBM 2250 display unit.

A brief account of the following topics, which are relevant to the work done by the author, is included below:

(a) Optical System

(b) Measuring System

(c) CRT Spot Deflection Logic

(d) Operator - Computer Communication

(e) Filtering of Output Signal

VI.7 Optical System

A diagram of the Glasgow Polly is shown in figure 6.3. There are two main optical systems using common components. The light from the CRT spot passes through the CERN 3 lens and is divided into two rays by the splitting prism. One ray is imaged onto the film (with a magnification of 0.68

approximately) , passes through the condenser lens, and is reflected into the signal photomultiplier. The other ray passes from the splitting prism along an identical light path (but without film), to the reference photomultiplier. The pulses from the signal photomultiplier are measured relative to the reference photomultiplier level, and are therefore independent of variations in phosphor response across the C.R.T. surface.

The other optical system produces an enlarged picture (X 8.9) of the film view for the operator. When the rotating mirror (see figure 6.3) is in the alternative position, light from a quartz iodine lamp passes through the splitting prism, and one ray is focused by the optical projection lens onto a translucent screen in front of the operator. The two systems are interlocked to switch the photomultipliers off while the optical picture is displayed.

VI.8 Measurement System

The Glasgow Polly has two measuring modes - a slice scan mode, and a raster scan mode, which can be called to digitise a larger area of the film in order to produce a computer re-constructed view on the IBM 2250 display unit. The raster scan mode is normally used only for difficult events, although it could also be used as a substitute for pre-scanning if, for example, only events of a certain topology are to be measured.

VI.9 C.R.T. Spot Deflection Logic

The method of measuring the film consists of deflecting the C.R.T. spot to the desired major deflection point, which

can be any point on a square array of 4096x4096 points across the C.R.T. face. (The array of major deflection points measures 128x128 mm. on the film, with the major deflection divisions measuring 31.25 microns.) The spot then can scan along a short line from the major deflection point (or scan line 'master point') in any one of 32 directions. The x- and y- deflection currents to produce these short scan lines consist of ramp currents which rise with constant speed. For directions which make 45° or less with the x (or y) deflection direction, the projection of the spot on the x (or y) axis moves with the constant speed of 8 microns per microsecond. The velocity of the spot (the vector sum of the x and y motions) therefore varies as $V/\cos\theta$, where θ is the angle between the direction of motion and the x- or y-axis direction (whichever gives the smaller value of $|\theta|$). After completion of one scan line, the spot is moved to the major deflection point nearest to the first scan line master point (in a direction orthogonal to the scan line direction), so as to be positioned to move along a second scan line, parallel to the first line. Up to 127 parallel scan lines, covering a rectangular area on film, constitutes a 'slice scan' (see figure 6.4).

The Argonne hardware logic to generate the slice scans was found to be unnecessarily complicated. The author redesigned this logic completely, using a less expensive series of logic modules.

This hardware logic consists of two sections:

(a) Slice Scan Direction Logic, and

(b) Edge Count Logic

(a) Slice Scan Direction Logic

The binary codes for the 32 possible slice scan directions are illustrated in figure 6.5 The sequence of master points for a series of scan lines is generated in the x- and y- master point position counters. For scan lines in the first half of the first quadrant, the x- and y- master point position counters work by adding one to the x-counter, and advancing the y-counter by a fraction appropriate to the slice direction. For example, the '1 in 4' direction (direction code 00001) is generated as in figure 6.6 for an initial master point at (70,100), say.

For slice directions in the other quadrants where subtracting $\frac{1}{4}, \frac{1}{2}$ or $\frac{3}{4}$ to one of the counters is involved, the fractional bits are subtracted from the position counters, but the position count is not decremented until the fractional bit equals one. The ' -1 in 2 ' line (direction 11110), for example, is illustrated in figure 6.7

A five bit register specifies the direction of the slice scan. The slice direction decoding logic is designed to enable the correct sequence of master points to be generated from the direction register, using a pulse from the computer which signifies the beginning of a new line. Logic circuits, using DEC 'M' Series Modules (ref 6.6), were designed by the author to generate the master points. These have now been built and tested (ref. 6.7)

and perform successfully in Polly.

(b) Edge Count Logic

The position of the C.R.T. spot, relative to the master point for each scan line, is measured at any time by counting the number of oscillator clock pulses which have elapsed since the spot left the master point (the 'edge count').(The least count from this oscillator is equivalent to $\frac{1}{4}$ of the time taken to move the spot between two adjacent major deflection points. It is convenient to approximate the major deflection division size on film, 31.25 microns, to 32 microns. One micron then equals 1.023 'Polly microns', and the least count from the oscillator corresponds to between 8 and $8\sqrt{2}$ Polly microns, depending on the scan line direction). However, the master points for the scan lines in one slice scan are not usually colinear (see figures 6.5 and 6.6). To simplify the calculation of position on the film the edge counter is designed to modify the number of pulses recorded, to compensate for this non-colinearity, so that effectively the position of the spot is measured from the side of the slice scan, rather than from the non-colinear master points. The exact edge count modification for each scan line in a block of four is, generally, a non-integral number of clock pulses (the relative position of the edge of the slice scan,and the scan line master points,for slice scan directions in the 1st quadrant, are shown in figure 6.8). Using the nearest integral value of clock pulses to the required exact modification integers is considered in Table 6.1 From symmetry, only the

five slice scan directions '00000' to '00100' require to be considered, and since directions '00000' and '00100' need no correction, only 3 slice scan directions are included in Table 6.1. Choosing the edge count modification as the integral value nearest to the exact desired modification gives the lowest error for directions '00001' and '0011', while for direction '00010' the alternative set of integers (third column in table 6.1) reduces the residual error. The effect of increasing the clock pulse frequency so that 8 or 16 clock pulses elapse while the spot crosses one major deflection division was also investigated and is illustrated in Table 6.1. Doubling the clock pulse frequency does not change the residual error appreciably, while four times the frequency gives a decrease in error (averaged over the three directions) from 0.51 microns to 0.17 microns. However, multiplying the clock frequency by four would mean increasing the edge counter from seven to nine bits: this would not then conveniently fit into the byte structure of the computer, which has an 8 bit byte. Alternatively, one could increase the edge counter to eight bits and half the width of a slice. The increase in accuracy would not make either of these possibilities worthwhile. The residual error can be corrected in the programme.

Figure 6.9(a) is a truth table for edge count modification. NL05 and NL06 are the two least significant bits of the 'number of lines' counter. These are used to determine whether a particular line is the first, second,

third, or fourth of a block of four. The sequence recycles after four lines, so only these two bits need be examined. An example of the final logic drawings is illustrated in figure 6.10 . This is the edge counter control derived from the truth table of figure 6.9.

VI.10 Operator - Computer Communication

In the original Argonne Polly I system, a T.V. scan of the film on a monitor oscilloscope was provided by a system which was separate from the precision measuring system and a cursor on the monitor could be positioned by the operator to indicate to the computer regions of the film which were to be measured. In Polly II at Argonne, a computer positioned optical cursor on an optical projection of the film replaces the monitor oscilloscope and cursor, allowing the operator to see which region of the film is being measured. An I.D.I. display C.R.T. displays the slice scan information to the operator, and allows operator communication with the computer whenever necessary.

The Glasgow Polly does not have the optical cursor facility on the optical projection of the picture because early tests on the Argonne Polly indicated that for most events the optical marker was not essential. (Initial experience with the machine has, however, led us to believe that with more difficult film the optical marker will be of such advantage that we intend to add this facility to our machine). An alternative facility included in the Glasgow Polly is the raster scan. This is produced by the same C.R.T.

and electronics as the precision measuring slice scan mode, and can be used, when necessary, to digitise one view in six or seven seconds. The spacing between the lines of the raster scan is eight times larger than the slice scan lines, and the scan line length is also longer. The data from the raster scan consisting of the line number and centre co-ordinate of each signal pulse, is reconstructed on the I.B.M. 2250 visual display unit by a programme written by the author.

The raster scan programme allows the operator to communicate with the computer via the '2250' display keyboard and track ball to indicate, for example, where the vertex lies. This is done by positioning a cross on any point on the picture, using the track ball. The '2250' picture can also be enlarged by the operator about any point of interest, by selecting an option on the programme function keyboard.

The number of points which can be displayed on the '2250' screen is limited by the size of the '2250' buffer. For a typical frame, only about one quarter of the raster scan digitisings can be reconstructed on the screen.

VI.11 Filtering of the Photomultiplier Output Signal

The photomultiplier output voltage is passed through a filter, to reduce high frequency noise. As mentioned previously, Glasgow Polly is designed to measure film from the 2m CERN H.B.C., which, with an image size of 128mm × 50mm is approximately double the length of the film dimension specification for the Argonne Polly machines. The Glasgow Polly design involved doubling the scale of the Argonne machines. Thus the scan speed, deflection currents, and

optical components are twice the size at Glasgow, and so the filter likewise required modification to deal with the higher frequency signals produced by the 8m/sec C.R.T. spot speed.

The filter used in the Argonne circuitry is a sine-squared filter. To obtain the desired doubling of frequency cut-off, it was decided to decrease the capacitors and decrease the inductances by a factor of approximately two(the actual factor being dependent on the values commercially available) from the Argonne values. The author simulated the frequency characteristics of the new filter by using the programme ECAP (electronic circuit analysis programme - ref 6.8). The ECAP prediction of the filter output (for a sine wave input) is compared with the actual output obtained in figure 6.12. The frequency characteristics (from ECAP calculations), and filter design are illustrated in figure 6.11. The phase lag varies linearly with frequency ($\phi = kf$, say, where $k = \pi/(1.9\times10^{5})$). The attenuation can be described fairly accurately below 400kc/s by the function:

$$0.5(\cos(f/F) + 1), \qquad \text{where } F = 4\times10^{5}/\pi$$

and f = frequency.

The simplicity of these analytic forms for the frequency characteristics make possible in the next chapter an investigation of the output pulse shape and duration obtained from Polly hardware for various film and C.R.T. spot conditions.

References

6.1 R.I.Hulsizer et al.

Methods of Computational Physics Vol 5

Academic Press Inc. (1966)

6.2 P.V.C.Hough

Bubble and Spark Chambers, Vol 2

Academic Press Inc. (1967)

6.3 J. Berge et al.

Proceedings of Cambridge International Conference on

Data Handling Systems in High Energy Physics (1970)

6.4 R.Barr et al.

Argonne National Laboratory

ANL/HEP 6806 (1968)

6.5 W.W.M.Allison et al.

Argonne National Laboratory

ANL/HEP 7007 (1970)

6.6 Digital Logic Handbook

Digital Equipment Corporation, Massachusetts

6.7 The hardware construction and testing was carried

out by Dr.C.J.Robinson and Mr.R.Benetta.

6.8 ECAP, Electronic Circuit Analysis Programme

Glasgow 360/44 User Notice 26

J.M^{C}Cormick

I.B.M. S/360 General Program Library 11620-EE-02X

TABLE 6.1 - Edge Count Modification

Number of clock pulses per major deflection division		4 clock pulses			8 clock pulses			16 clock pulses		
		a	b	c	a	b	c	a	b	c
1 in 4	Line 1	0.94	1	-	1.88	2	2	3.76	4	-
	Line 2	1.88	2	-	3.76	4	4	7.52	8	-
	Line 3	2.83	3	-	5.66	6	5	11.32	11	-
	Sum of errors*		0.35	-		0.70	-.30		0.40	-
	Mean error*		0.70	-			0.30		0.20	-
2 in 4	Line 1	1.6	2	2	3.2	3	-	6.4	6	6
	Line 2	0	0	0	0	0	-	0	0	0
	Line 3	1.6	2	1	3.2	3	-	6.4	6	7
	Sum of errors*		0.8	-0.2		0.4	-		-0.8	0.2
	Mean error*			0.4		0.4	-			.11
3 in 4	Line 1	1.9	2	-	3.84	4	-	7.7	8	8
	Line 2	1.28	1	-	2.56	3	-	5.1	5	5
	Line 3	0.64	1	-	1.28	1	-	2.6	3	2
	Sum of errors*		0.16			0.3			0.6	-.4
	Mean error*		0.39			0.39				0.22

Column 'a' : Edge count modification (in clock pulses) indicated from figure 6.8

Column 'b' : Nearest integral value to required modification.

Column 'c' : Alternative set of integral values to those shown in column 'b', which give a lower average error than those of column 'b'.

* : The sum of errors for lines 1,2 and 3 is in clock pulses. The mean error is the average error (in microns) over the set of four scan lines in the sequence. In cases where an alternative set of integers exist, it corresponds to the lower error.

Figure Captions

6.1 S.M.P. periscope and photomultiplier system.

6.2 H.P.D. spot generator.

6.3 Glasgow Polly optical system (from 'Progress on Polly at Glasgow', see list of Publications)

6.4 Diagram of the slice scan concept. The parallel lines represent the C.R.T. spot path crossing a series of bubbles (shown dotted).

6.5 The 32 possible slice scan directions, with corresponding binary codes.

6.6 C.R.T. spot path for successive scan lines for '1 in 4' slice scan. The master point generation for the slice scan lines is shown in figure 6.6(b).

6.7 As figure 6.6, but showing '-1 in 2' direction.

6.8 Relation between the master points for four slice scan directions, and the 'edge' of the slice scan. The correction required for each line is the distance between the master point, and the 'edge'.

6.9 The edge count modification. The left-hand column contains the binary code for the slice scan direction. The centre columns show the modifications required for lines 2,3 and 4 of each sequence of four lines, and the right-hand column shows the fractional count ($\frac{1}{4}$,$\frac{1}{2}$ or $\frac{3}{4}$) by which the X- (or Y-) counter is incremented after each scan line.

6.10 Logic diagram to generate the edge count modification shown in figure 6.9 . QC, HC and TQC are the fractional

counts (as above), NLO5 and NLO6 are the line count least significant bits, and CDO2 is the third most significant bit of the slice scan direction counter (i.e. CDO2 is FALSE for slice scans in the first half of each quadrant, and TRUE for the second half). IEC1, DEC1 etc. denote the number of counts to be added to (or subtracted from) the edge count.

6.11 Frequency characteristics of Glasgow Polly photomultiplier output signal filter, calculated from ECAP (ref. 6.8). The filter design is shown (inset).

6.12 Square wave input pulse response from filter, (below) photographed on a CRT screen, and (above), as predicted by ECAP.

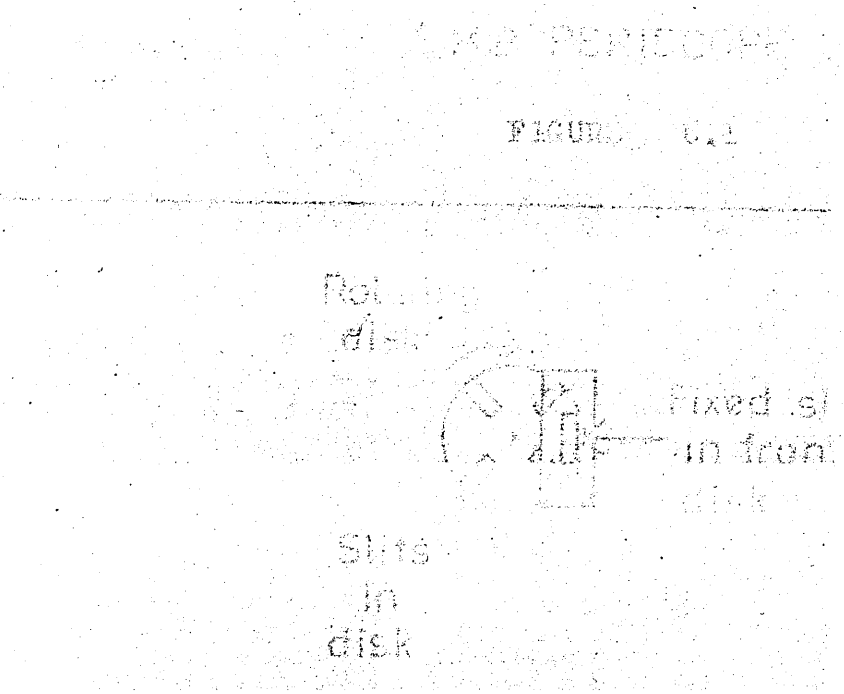

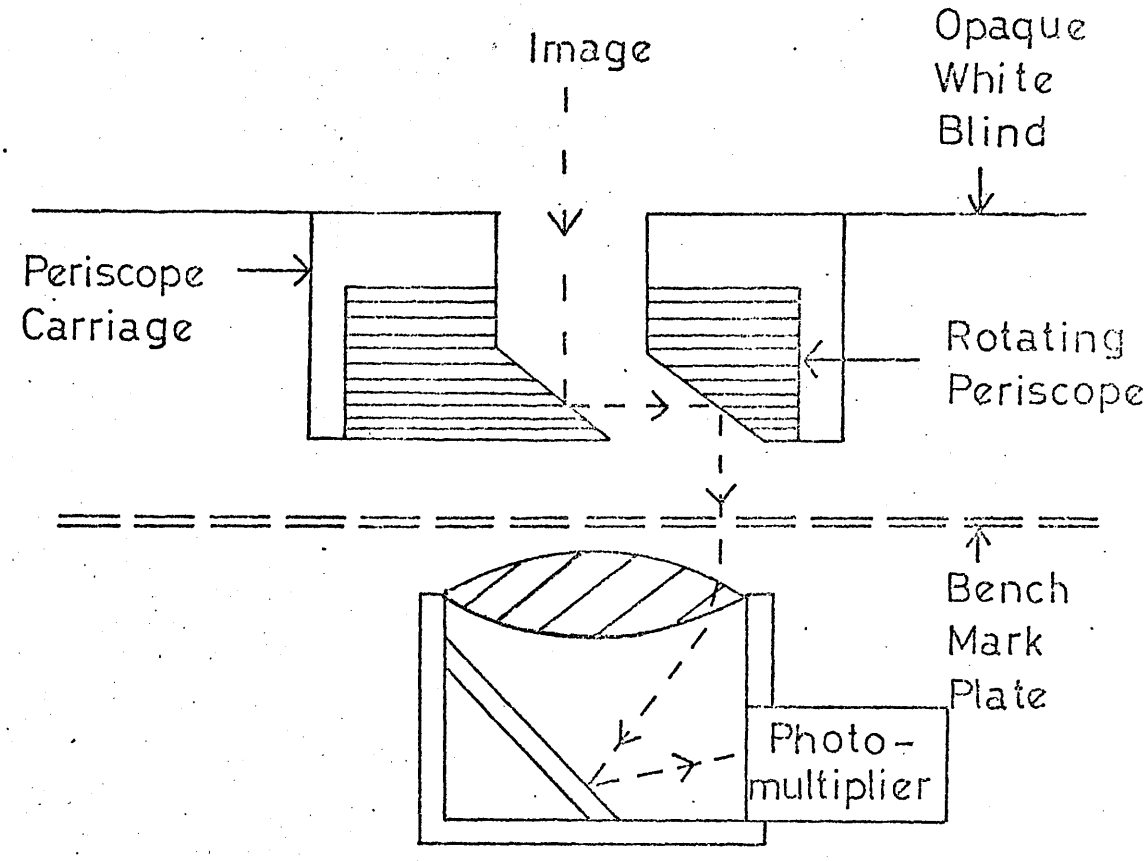

SMP PERISCOPE SYSTEM

FIGURE 6.1

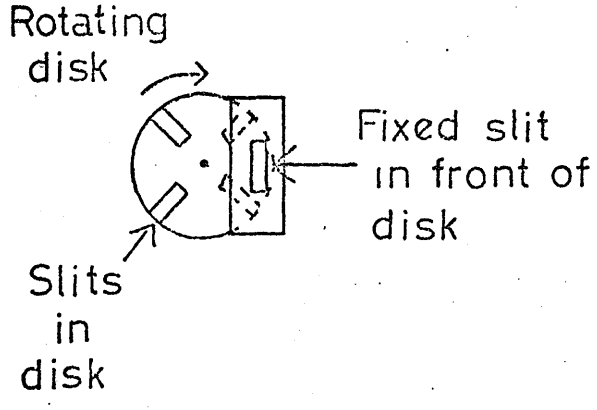

H P D SPOT GENERATION

FIGURE 6.2

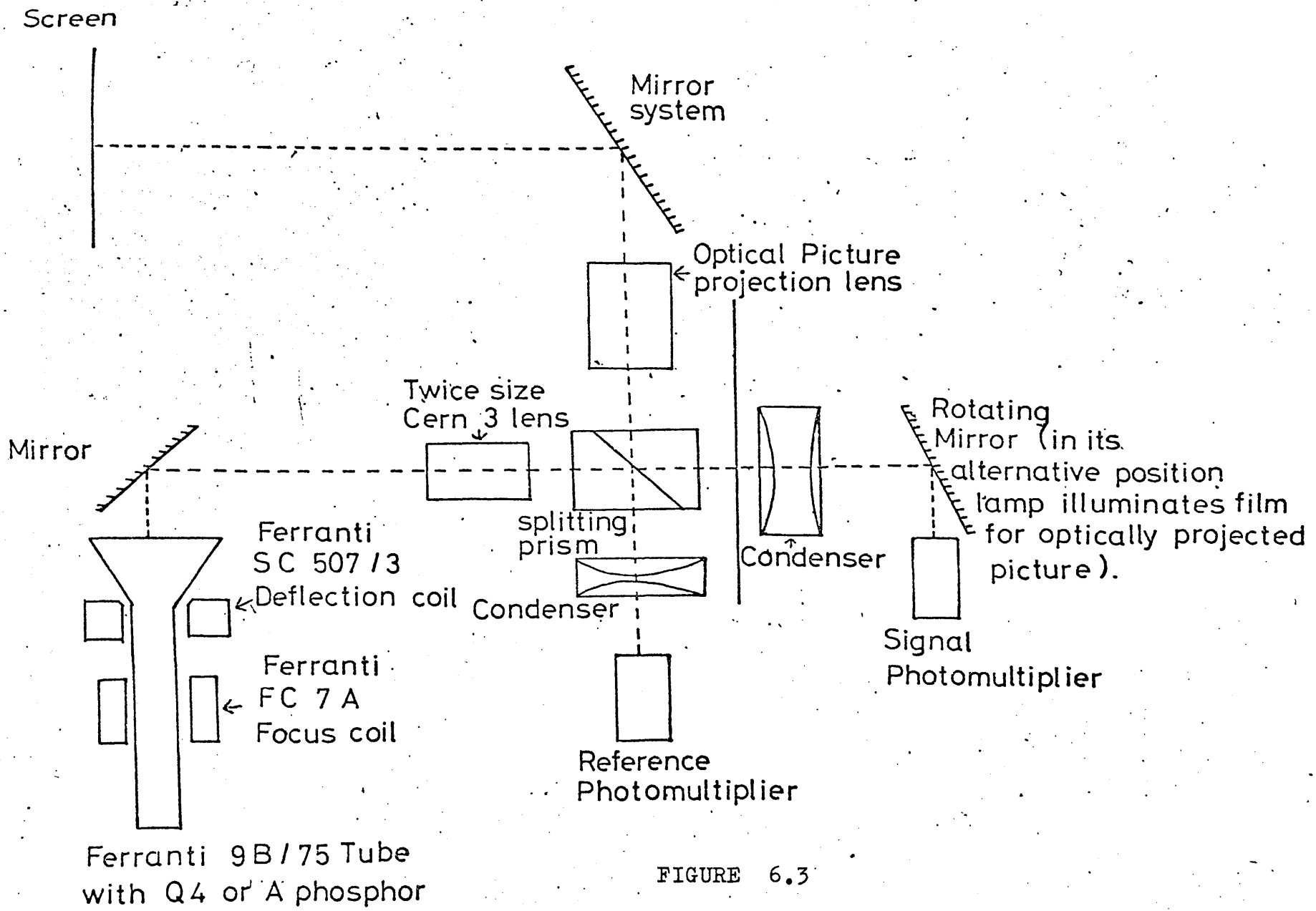
Screen
Mirror system
Optical Picture projection lens
Twice size Cern 3 lens
Mirror
Rotating Mirror (in its alternative position lamp illuminates film for optically projected picture).
splitting prism
Condenser
Condenser
Ferranti SC 507/3 Deflection coil
Ferranti FC 7A Focus coil
Signal Photomultiplier
Reference Photomultiplier
Ferranti 9B/75 Tube with Q4 or A phosphor

FIGURE 6.3

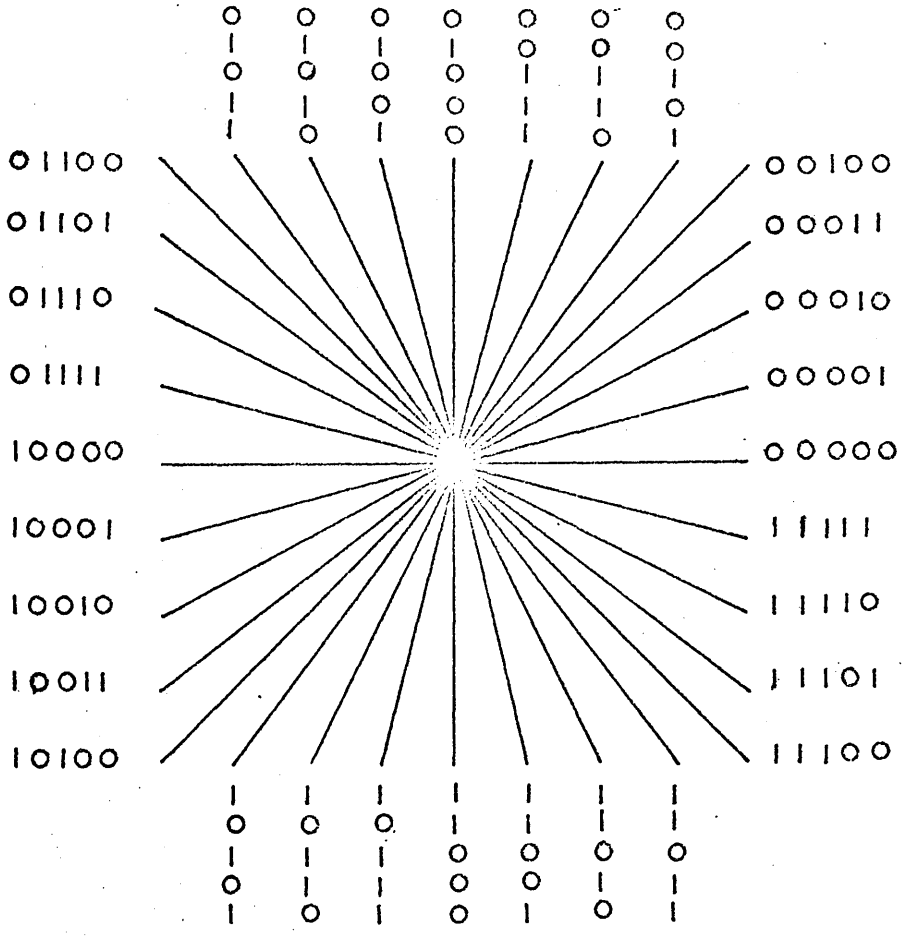

32 POSSIBLE SLICE SCAN DIRECTIONS

Line separation 32μ

Maximum 127 lines

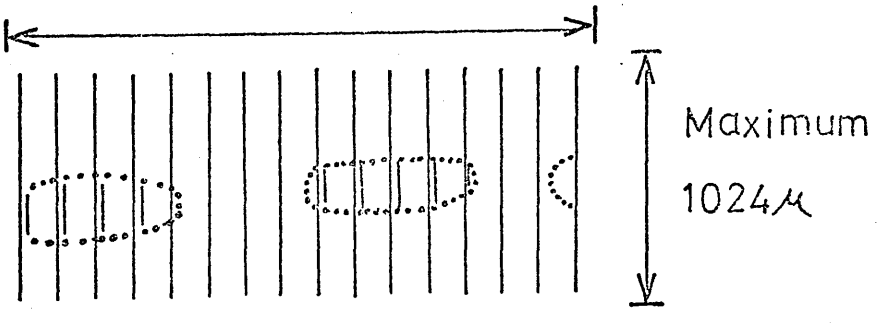

A SLICE SCAN (DIRECTION 00000)

FIGURE 6.4 (below)

FIGURE 6.5 (above)

	X-COUNTER	Y-COUNTER	MASTER POINT
	70	100	(70, 100)
ADD	71	100¼	(71, 100)
1 to X	72	100½	(72, 100)
¼ to Y	73	100¾	(73, 100)
	74	100	(74, 100)

MASTER POINT GENERATION
(FOR SLICE DIRECTION 00001)

(b)

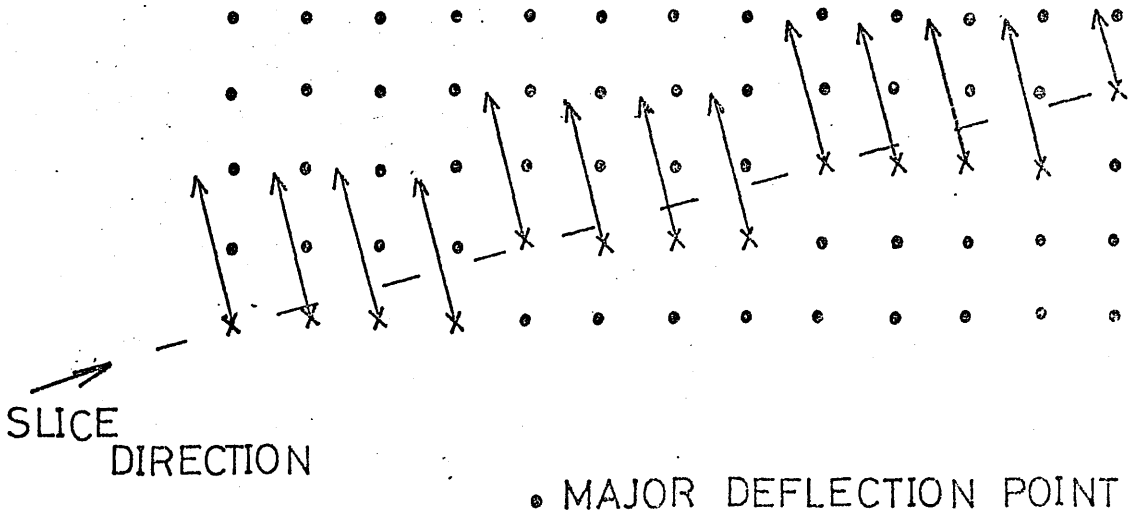

PART OF SLICE SCAN (DIRECTION 00001)

(a)

FIGURE 6.6

	X COUNTER	Y COUNTER	MASTER POINT
	150	90	(150, 90)
ADD	151	90½	(151, 90)
1 to X	152	89	(152, 89)
-½ to Y	153	89½	(153, 89)
	154	88	(154, 88)

MASTER POINT GENERATION
(FOR SLICE DIRECTION 11110)

(b)

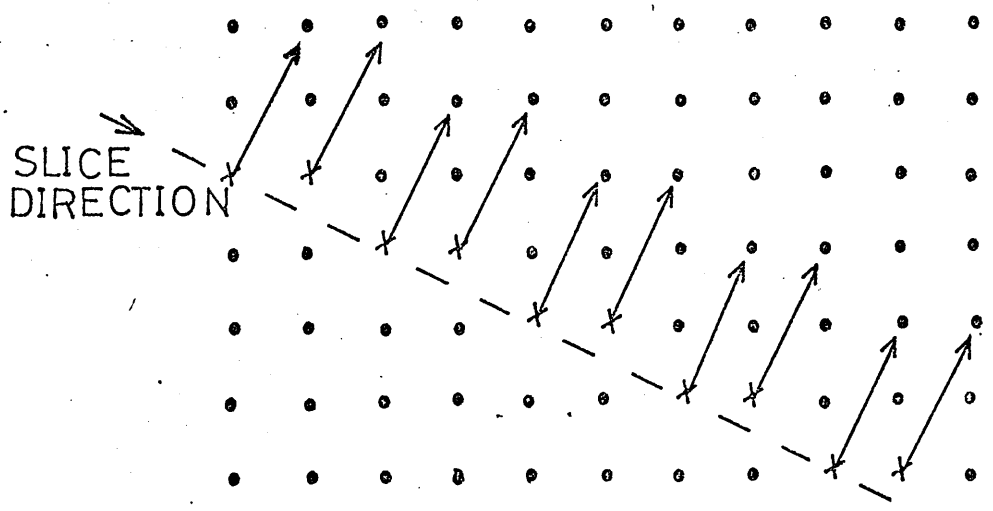

• MAJOR DEFLECTION POINT

X SCAN LINE MASTER POINT

→ SCAN LINE DIRECTION

PART OF SLICE SCAN (DIRECTION 11110)

(a)

FIGURE 6.7

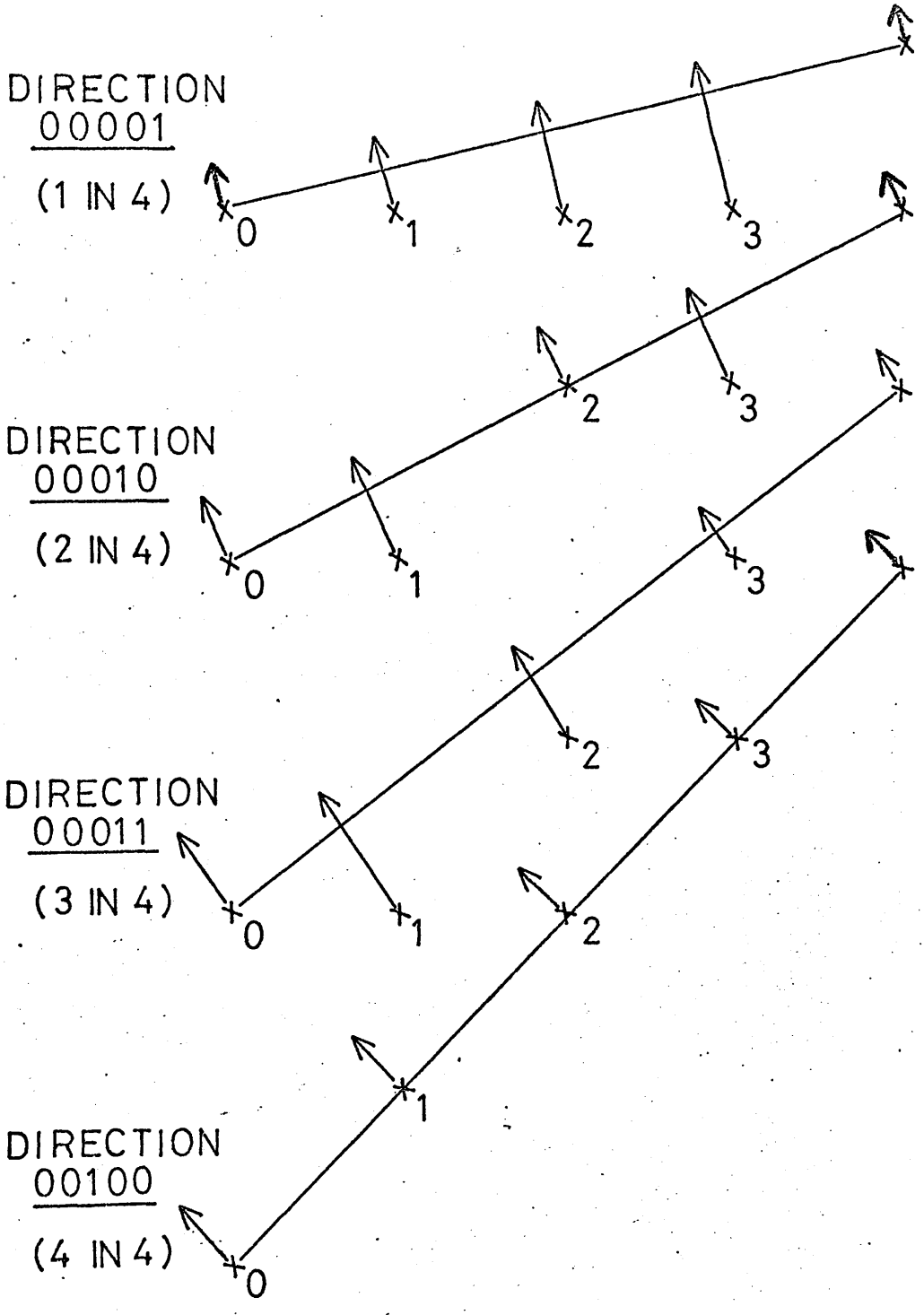

SLICE SCAN MASTER POINT SEQUENCES FOR FOUR SLICE SCAN DIRECTIONS.

FIGURE 6.8

DIRN	COUNTS ADDED			CORRESPONDING FRACTIONAL COUNT
	$(\overline{NLO5}.NLO6)$	$(NLO5.\overline{NLO6})$	(NLO5.NLO6)	
00001	-1	-2	-3	QC
00010	-2	0	-1	HC
00011	-2	-1	-1	TQC
00100	0	0	0	-
00101	+2	+1	+1	TQC
00110	+2	0	+1	HC
00111	+1	+2	+3	QC
01000	0	0	0	-
01001	-1	-2	-3	QC
01010	-2	0	-1	HC
01011	-2	-1	-1	TQC
01100	0	0	0	-
01101	+2	+1	+1	TQC
01110	+2	0	+1	HC
01111	+1	+2	+3	QC
10001	-1	-2	-3	QC
10010	-2	0	-1	HC
10011	-2	-1	-1	TQC
10100	0	0	0	-
10101	+2	+1	+1	TQC
10110	+2	0	+1	HC
10111	+1	+2	+3	QC
11000	0	0	0	-
11001	-1	-2	-3	QC
11010	-2	0	-1	HC
11011	-2	-1	-1	TQC
11100	0	0	0	-
11101	+2	+1	+1	TQC
11110	+2	0	+1	HC
11111	+1	+2	+3	QC

EDGE COUNT MODIFICATION

FIGURE 6.9

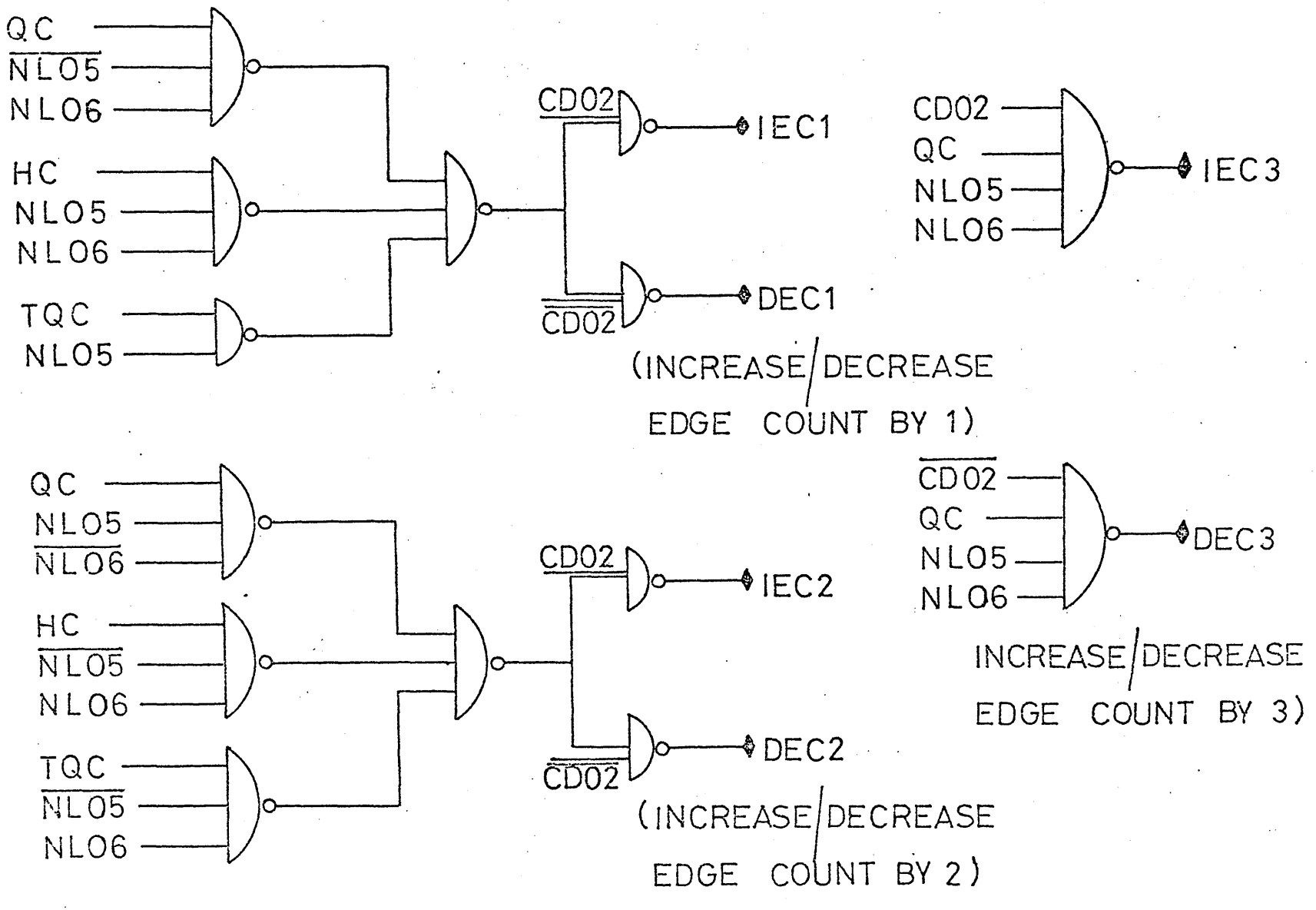

FIGURE 6.10 EDGE COUNTER CONTROL

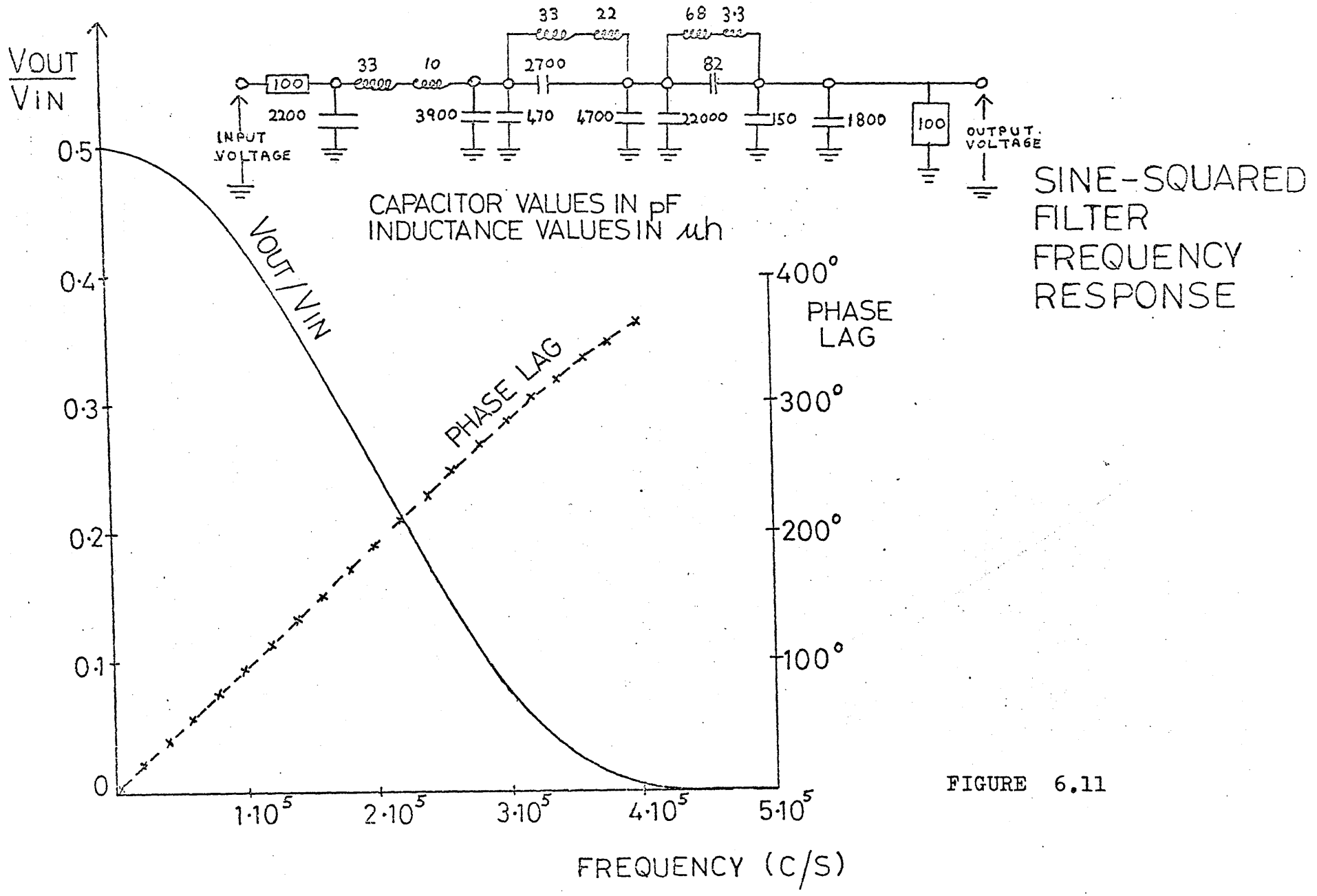
VOUT/VIN
0·5
0·4
0·3
0·2
0·1
0
1·10^5
2·10^5
3·10^5
4·10^5
5·10^5
FREQUENCY (C/S)
VOUT/VIN
PHASE LAG
400°
300°
200°
100°
PHASE LAG
100
2200
33
10
3900
470
33
22
2700
4700
68
3·3
82
22000
150
1800
100
INPUT VOLTAGE
OUTPUT VOLTAGE
CAPACITOR VALUES IN pF
INDUCTANCE VALUES IN μh
SINE-SQUARED FILTER FREQUENCY RESPONSE

FIGURE 6.11

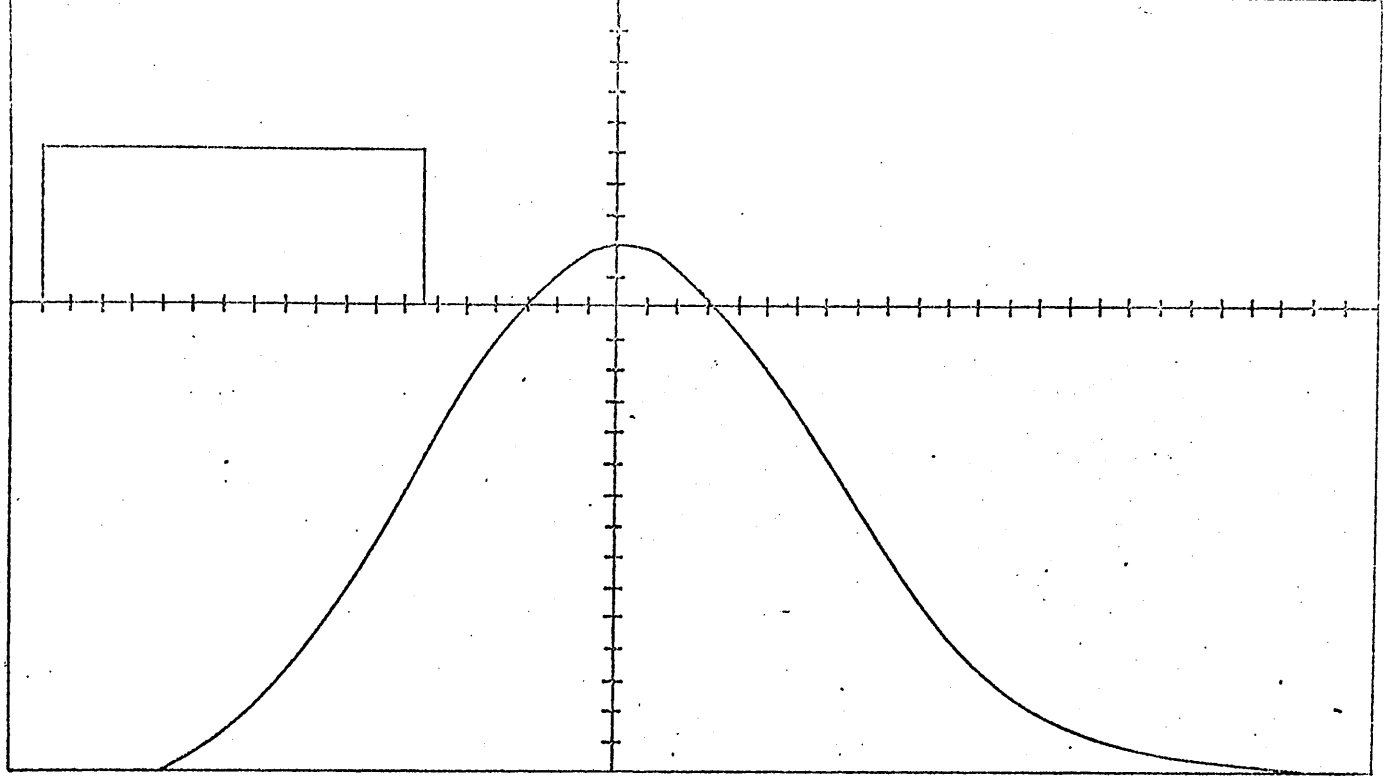

ECAP CALCULATION OF FILTER OUTPUT

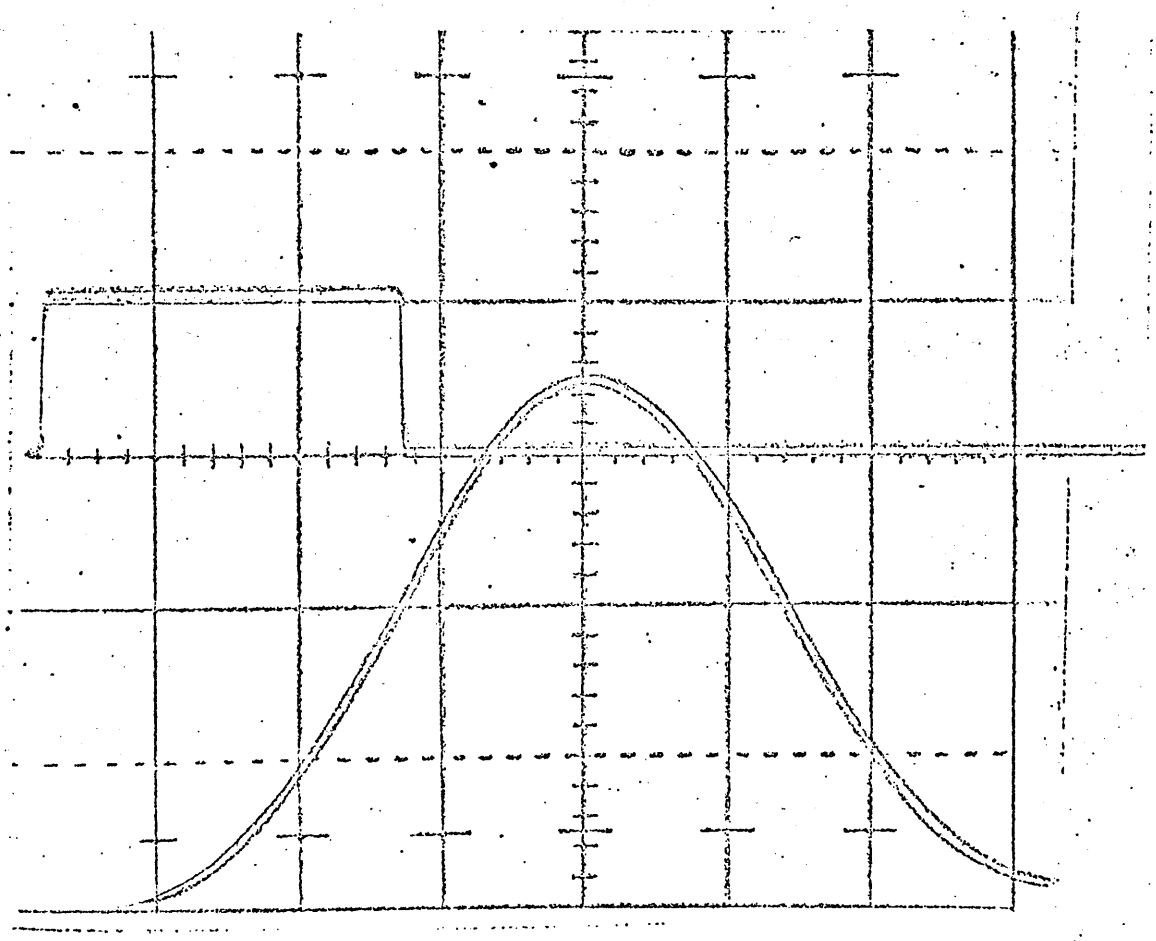

Photograph of filter output and square wave input displayed on a C.R.T. face.

FIGURE 6.12

CHAPTER VII

Ionisation Information from Polly

VII.1 Introduction

The provision of reliable ionisation information is a most important consideration for any film measuring device. The ionisation along a track of given momentum depends on the particle mass, and in many cases this resolves kinematic ambiguities in the post measurement analysis of an event. The information obtained from Polly is particularly suitable for ionisation calculations. In addition to the usual 'hit or miss' information, the width of each track crossing is also measured.

The Argonne Polly software uses a semi-empirical formula for the bubble density(ref 7.1). The Argonne formula uses the number of misses (M), the number of hits (H), and the average track width ($\overline{W}$) for a track. The ionisation (b) is given by:

$$b = \frac{k}{\overline{W}} \text{ LOG } \frac{H+M}{M} \qquad (7.1)$$

where 'k' is a constant for one view. (A glossary of the symbols used frequently in this chapter is included at the end of the chapter). The basis for this formula is the theory of gap length distributions in a bubble chamber track(ref 7.2). The distribution of gaps of length 'ℓ' in a track of bubble density 'b' is:

$$G(\ell) = b \exp(-b(a+\ell)) \qquad (7.2)$$

The constant 'a' is the minimum resolution distance, which is the smallest distance between adjacent bubble centres

for which a gap between the bubbles can be discerned. The lacunarity (L) is the average fraction of track consisting of gaps, and, from (7.2), this is:

$$L = \exp(-ba) \qquad (7.3)$$

For the Polly measurements, the lacunarity L, and the average track width $\bar{W}$ are given by:

$$L = \frac{M}{H+M} \qquad \bar{W} = v\bar{T}$$

where $\bar{T}$ is the average pulse length, and 'v' is the velocity of the C.R.T. spot image on the film. The formula (7.1) then follows directly from (7.3) if it is assumed that the average pulse length ($\bar{T}$) multiplied by the spot image velocity (v) is proportional to the mean resolution distance (a), with the same constant of proportionality throughout one view. In the following sections, the validity of relation (7.1) is investigated, and it is shown that better agreement with the data can be achieved using a modified formula.

VII.2 Photomultiplier Output Signal

The light input to the photomultiplier is reduced as the image of the C.R.T. spot, travelling across the film, crosses a bubble image. The shape and duration of the light variation is determined by:

(i) bubble image size, and distribution of silver grains on the film within the bubble image.

(ii) the size and velocity of the image on film of the C.R.T. spot, and the distribution of light intensity in the image.

(iii) the opacity of the bubble image, and of the surrounding film.

The filtered output signal depends also on the frequency responce of the filter. The output pulse length is counted from whenever the output signal falls below a certain voltage (the discrimination level).

Bubble Image and Size

Two bubble images, chosen from a minimum ionising beam track, were examined using an oil objective microscope with overall power 900. The silver grain density at different points along a central section across the bubble was estimated: histograms of the results are shown (figure 7.1). It can be seen that, rather precisely, the grain density follows a Gaussian distribution across the bubble image.

Since the bubble image has no abrupt edges, any measure of bubble diameter depends on judging when the visual contrast falls below a certain level. To relate the 'diameter' of a bubble image (as measured from the optical projection of the film in a conventional measuring machine) to the standard deviation of the silver grain Gaussian distribution, a paper model was constructed. The model was made of suspended layers of translucent paper: the number of layers at any point on the XY plane was approximately proportional to the Gaussian function, $\exp(-(x^2+y^2)/2\sigma^2)$. This was illuminated from various positions, and a paper screen positioned so that the shadow cast by the model fell on the screen. Measurement of the estimated 'diameter' of this shadow was made by

several people. The mean value of these estimates indicated that the 'diameter' of the Gaussian was roughly three times the standard deviation. The following arguments do not depend critically on this relation.

Two methods were used to measure bubble diameters on a beam track(a 10GeV/c K^+ beam track from the 2m Cern HBC was measured). In the first, the positions of each end of each bubble were measured as accurately as possible. A histogram of bubble radii obtained from these measurements is shown in figure 7.2. The main peak of the histogram occurs at bubble radius of around 14 microns, with the 'standard' deviation' of the distribution around 4 microns. A second smaller peak at around 25 microns could have been caused by double bubble images: when two images coalesce, the measured diameter of the composite image will be equal to or less than the sum of the diameters of the two individual bubbles.

Bubble centre separation also provides a method of assessing bubble image diameter. The distribution of bubble centre separations greater than x, say, is $n\exp(-gx)$ where n is the total number of bubbles. (See reference7.2).

A graph of the variation of the logarithm of the number of bubble centre separations greater than x, as a function of x, should be linear. However if the distance between the two bubble centres is less than the sum of their radii, these bubbles will not be resolved, and the graph should deviate from linearity when 'x' equals

twice the bubble radius. Figure 7.3, which contains data from the same track as figure 7.2, gives an estimate of bubble radius by this method in the range 7.5 to 15 microns.

Using the approximate relation between bubble 'diameter' and standard deviation mentioned previously, the standard deviation of the bubbles in the beam track measured range between 6 and 12 microns.

CRT Spot Size

The author measured the CRT spot size in Polly by constructing a series of square wave gratings of different wavelengths, which were photographed and measured. The technique used is outlined in reference 7.3. By measuring the modulation of the signal obtained by scanning the spot across several different wavelength gratings, the standard deviation of the spot (which is assumed to have a Gaussian distribution of intensity on the CRT face) was obtained. The value for the Polly spot was 16 microns scanning along the 0 direction.

The spot size was also estimated travelling in the 45° direction, when the velocity is higher. The standard deviation in this case was 19 microns. The values of the spot standard deviation will depend on the precise focus conditions, and the portion of the cathode ray tube face. We can, however, conclude from the figures that the spot size is of the same order of magnitude as the bubble size.

VII.3 Filtered Output Signal

An analytic expression for the output signal for the Gaussian spot crossing a Gaussian bubble is obtainable

using the frequency characteristics of the filter listed in the previous chapter.

The intensity of light, I, reaching the point (x,y) on film when the spot image is centred at point (D,E), say, is:

$$I = \frac{1}{2\pi\sigma_s^2} \exp\left[-\frac{(x-D)^2+(y-E)^2}{2\sigma_s^2}\right] \qquad (7.4)$$

where σ_s is the standard deviation of the spot.

The fraction of light transmitted, T, when a bubble image of standard deviation σ_b is centred at the origin, and (1 - A) is the transmission factor at the centre of the bubble, is:

$$T = 1 - A\exp\left[-\frac{x^2+y^2}{2\sigma_b^2}\right] \qquad (7.5)$$

The light reaching the photomultiplier is:

$$\int_{-\infty}^{\infty}\int IT\,dx\,dy = 1 - B\exp\left[-\frac{D^2+E^2}{2(\sigma_s^2+\sigma_b^2)}\right] \qquad (7.6)$$

$$\text{where } B = A\left(\frac{\sigma_b^2}{\sigma_s^2+\sigma_b^2}\right)$$

For the spot moving in the y-direction, with velocity v and passing through point (D,0), the photomultiplier light input, V_i say, is:

$$V_i(t) = 1 - B\exp\left(-\frac{t^2}{2s^2}\right)\exp\left(-\frac{D^2}{2s^2v^2}\right) \qquad (7.7)$$

where t is the time and $s = \sqrt{\sigma_s^2+\sigma_b^2}/v$

The input signal can be expressed in terms of its frequency (ω) components:

$$V_i(t) = 1 - \frac{sBd}{\sqrt{2\pi}}\int_{-\infty}^{\infty}\exp\left[-\frac{\omega^2s^2}{2}\right]\cos\omega t \qquad (7.8)$$

$$\text{putting } d = \exp\left[-D^2/(2s^2v^2)\right]$$

The filtered output voltage is (using the frequency characteristics of the filter):

$$V_o(t) = \frac{1}{2} - \frac{sBd}{4\sqrt{2\pi}}\int_{-\infty}^{\infty}\left[1+\cos\left(\frac{\omega}{8.10^5}\right)\right]\exp\left[-\frac{\omega^2s^2}{2}\right]\cos\omega(t-k)\,d\omega \qquad (7.9)$$

where 'wk' is the phase delay introduced by the filter for a signal of frequency w.

Thus $$V_0(t+k) \doteq \frac{1}{2} - \frac{Bd}{4}\left(\exp\left[-\frac{t^2}{2s^2}\right] + \frac{1}{2}\exp\left[-\frac{(t+g)^2}{2s^2}\right] + \frac{1}{2}\exp\left[-\frac{(t-g)^2}{2s^2}\right]\right) \quad (7.10)$$

where g = 1.25 microsec.

The pulse consists of three superimposed Gaussian functions of equal standard deviation, but displaced in time from each other by 1.25 microseconds.

To simplify the following calculations, the author approximated the above expression to a function of the form: $$V_0'(t+k) = dC\exp\left(-\frac{t^2}{2u^2}\right) \quad (7.11)$$

with C and u functions of σ_s and σ_b, valid for all values of t, and for a range of spot and bubble standard deviations.

To obtain functional forms for C and u, sensible conditions to impose appeared to be that

(a) $V_1'(0)$ must equal $V_0(0)$

(b) the integral under the two curves $V_0(t+k)$ and $V_0'(t+k)$ over the more important central region of the pulse ($t+k = -2s$ to $t+k = 2s$, say) must be equal i.e.

$$\int_{x=-2s}^{x=2s} V(x)\,dx = \int_{x=-2s}^{x=2s} V'(x)\,dx$$

Applying criterion (a) gives

$$C = \frac{B}{4}\left[1 + \exp(-g^2/2s^2)\right] \quad (7.12)$$

and (b) gives

$$\frac{1}{y}\,\mathrm{erf}(\sqrt{2}y) = \frac{\left(\mathrm{erf}(\sqrt{2}) + \frac{1}{2}\left[\mathrm{erf}(\sqrt{2}+g/(\sqrt{2}s)) + \mathrm{erf}(\sqrt{2}-g/(\sqrt{2}s))\right]\right)}{(1+\exp(-g^2/(2s^2)))} \quad (7.13)$$

where y = s/u.

For the useful range of spot and bubble standard

deviations considered (from 9 to 30 microns) the right side of equation 7.13 was nearly constant (varying from 1.04 for s = 1.75 to 0.97 for s = 5.15). Choosing y = 0.95 gives equality in equation 7.13. The approximation for the voltage pulse is:

$$V_o(t+k) = \frac{Bd}{4}\left[1 + \exp\left(-\frac{g^2}{2s^2}\right)\right]\exp\left(-\frac{t^2}{2(s/0.95)^2}\right) \qquad (7.14)$$

The accuracy of approximation of equation 7.14 to equation 7.10 is better than 3% for all values of time, and for all bubble and spot deviations between 9 and 30 microns. Curves representing these voltage pulse equations for one value of spot and bubble standard deviation are shown in fig. 7.5.

VII.4 Average Discriminated Pulse Length

If the discrimination level is 'Z' volts below clear film level, then the discriminated pulse length ('T') will be:

$$Z = C\exp\left(-\frac{(T/2)^2}{2U^2} - \frac{D^2}{2S^2v^2}\right) \qquad (7.15)$$

The maximum pulse length, which occurs for the spot crossing a bubble centre, is:

$$T_{MAX} = 2\sqrt{2U^2 \log(C/Z)} \qquad (7.16)$$

and the maximum distance of closest approach of the spot to the bubble which will give a pulse below the discrimination level is:

$$D_{MAX} = v\sqrt{2S^2 \log(C/Z)} \qquad (7.17)$$

The average value of pulse length is obtained using the fact that all values of 'D' are equally probable:

$$\bar{T} = \frac{2\int_0^{D_{MAX}} \sqrt{2U^2}\left[\log(C/Z) - x^2/(2S^2v^2)\right]^{1/2} dx}{\int_0^{D_{MAX}} dx}$$

$$= D_{MAX}\, U\pi/(2Sv) \qquad (7.18)$$

i.e. $v\bar{T} = D_{MAX}$

since the ratio 'u/s' is constant, from the previous section. D_{MAX} can be taken as a measure of the minimum resolution

distance, and so, according to (7.18), the bubble density is given correctly by the Argonne formula (7.1). This result is independent of discrimination level, film transmission factor, and the spot and bubble sizes of the section of track.

The main factors which have been omitted in the above calculations are:

(i) Phosphor rise and fall time. It is assumed that the spot shape is Gaussian. However, the spot shape (and size) may vary with scanning velocity.

(ii) There is a cut-off on pulse length accepted by the Polly software, to reduce noise. Pulses below this cut-off are ignored.

(iii) It is assumed that bubbles are a uniform size, whereas there is a spread of bubble radii (see figure 7.2)

(iv) Bubbles on dense tracks coalesce to form clusters, in which the individual bubbles cannot be resolved.

VII.5 Agreement with Data

To check the validity of (7.1) experimentally, the author took readings of average track width ($\bar{W}$) and lacunarity (L) for several slice scans along a segment of track, at different discriminator settings and CRT focus currents (F). From (7.1) and (7.18), the graphs of $\log L$ against $\bar{W}$ shown in fig. 7.5 should be straight lines, passing through the point $L = 1$, $\bar{W} = 0$. For each focus current, the experimental points lie on straight lines, but the lines have intercepts on the $\bar{W}$ axis varying between 10 and 25 microns. This suggests that

we must consider the effects of points (i) to (iv) above, since formulae 7.1 and 7.14 are clearly not accurate. (The Argonne Polly software divides the bubble density given by (7.1) by a purely empirical factor, cos θ, which increases the bubble density of a track inclined at 'θ' to the x- (or y-) axis of the Polly coordinate system.)

VII.6 Corrections to the Bubble Density Expression.

In this section we will consider the effects of factors (i) to (iv), mentioned previously, on the bubble density expression (7.1).

(i) Phosphor Rise and Fall Time

The finite time of response of the CRT phosphor may change the shape of the output voltage signal. An equation which describes the behaviour of the phosphor layer on the CRT face is:

$$\frac{dN}{dt} = I(x,t) - \lambda N \qquad (7.19)$$

where N(x,t) is proportional to the number of excited phosphor molecules at time t, position x, and λ is a decay constant associated with the phosphor. I(x,t,) is the intensity of current hitting the phosphor layer.

For a square wave pulse of incident current, this equation predicts an exponential rise and fall of light output, as is observed experimentally. This gives confidence that it is reasonable to apply equation (7.19) to a more complex current distribution.

For a moving Gaussian current distribution, equation (7.19) becomes:

$$\frac{dN}{dt} = \frac{1}{\sqrt{2\pi\sigma_s^2}} \exp\left(-\frac{(x-vt)^2}{2\sigma_s^2}\right) - \lambda N \qquad (7.20)$$

The solution at $t=\tau$ to this equation is:

$$N(x,\tau) = \frac{\exp(-\lambda\tau)}{\sqrt{2\pi\sigma_s^{-2}}} \int_{-\infty}^{\tau} \exp(\lambda t) \exp\left(-(x-vt)^2/(2\sigma_s^{-1})\right) dt \qquad (7.21)$$

and the lightoutput at $t = T$ for the film transmission factor given in (7.5) is:

$$1 - \frac{\sqrt{\pi}}{2} p \exp(-\lambda\tau) \operatorname{erfc}(q\lambda - \tau/(2q)) \qquad (7.22)$$

with $q = s/\sqrt{2}$ and $p = \sqrt{2}\lambda s B \exp\left(\frac{s\lambda}{\sqrt{2}}\right)^2$

The signal output from the filter is:

$$V(t+k) = \frac{1}{2} - \frac{p}{4\sqrt{\pi}} \left(h(t) + \frac{1}{2}\left[h(t+g) + h(t-g)\right]\right) \qquad (7.23)$$

where $h(t) = \exp(-\lambda t) \operatorname{erfc}(q\lambda - \tau/(2q))$

The value of λ for the phosphor used, with the normal range of CRT cathode current of between 2 and 4 μa, and a circular spot of standard deviation 15μ, is $\lambda = 5.5\ \mu sec^{-1}$ The curve represented by equation (7.23) was computed as a function of time, with different values of spot and bubble diameter. The results obtained show that the phosphor rise and fall time introduces a time lag of order half a microsecond to the voltage pulse, relative to the pulse expression obtained by neglecting the effect. The shape of the pulse, however, is almost the same (see fig 7.7) and so the previous results are not invalidated by this effect.

(ii) Cut-off on Pulse Length

Equation (7.18) was derived assuming that all pulses could be detected. However, pulses of one clock pulse duration or less are rejected by the Polly software, to reduce noise. This corresponds to a lower limit of between 12 and 17 microns, depending on spot velocity, and on the

track width $\bar{W}$. (The programme which was used to obtain the results for figure 7.6 rejected all pulses of two clock pulses or less.) Denoting the cut-off pulse length by T_{CUT} the maximum value of D (cf 7.17) becomes:

$$D_{CUT} = V\sqrt{2S^2(\text{LOG}(c/2) - T_{CUT}^2/(8U^2))} \qquad (7.24)$$

$$= V\left(\frac{S}{U}\right)(1-m^2)^{1/2}T_{MAX}/2$$

where $m = T_{CUT}/T_{MAX}$

The average pulse length is now:

$$\bar{T} = 2\int_0^{D_{CUT}} \sqrt{2r^2}\left[\text{LOG}(c/2) - x^2/(2S^2v^2)\right]^{1/2} dx \Big/ \int_0^{D_{CUT}} dx$$

$$= T_{MAX}\left[m(1-m^2)^{1/2} + \cos^{-1}(m)\right]/\left(2(1-m^2)^{1/2}\right) \qquad (7.25)$$

A 'corrected' pulse length, T', can be defined such that $\bar{W} = vT'$ gives the correct bubble density in (7.1):

$$T' = f(m)\bar{T} \qquad (7.26)$$

where $$f(m) = \frac{\left[(1-m^2)^{1/2}m + \cos^{-1}m\right]}{2(1-m^2)} \times \frac{4}{\pi} \qquad (7.27)$$

The correction $\bar{T}$-T' is graphed in figure 7.8C as a function of $\bar{T}$.

(iii) Distribution of Bubble Sizes

We have assumed that the bubble density for data from a series of slice scans will be given correctly by considering all the bubbles to be of equal radius. Figure 7.2 illustrates that the distribution of bubble radii about the mean radius ($\sim 14\mu$) has a 'standard deviation' of around 4μ, giving a ratio:

$$\frac{r_0}{\sigma} \sim 3 \qquad (7.28)$$

Taking the distribution of bubble radii as approximately Gaussian,

$$N(r) = \frac{N}{\sqrt{2\pi\sigma^2}} \times \exp\left(-\frac{(r-r_0)^2}{2\sigma^2}\right) \times 2 \Big/ \text{erf}\left(\frac{r_0}{\sigma}+1\right) \qquad (7.29)$$

where r = bubble standard deviation

r_0 = most probable value of bubble standard deviation

and where the error function is to ensure normalisation over the physical region of bubble radii from $r=0$ to $r=\infty$ The dependence of C (equn. 7.12) on the bubble and spot sizes means that small bubbles (for which $C<Z$, equn. 7.15) cannot be detected. This results in the bubble density being underestimated by an amount which depends on the discrimination level. If the smallest bubble detectable is r_{MIN} , the number of bubbles lost is:

$$N_{LOST} = \int_{r=0}^{r_{MIN}} N(r)\,dr$$

$$= \frac{N}{\operatorname{erf}\left(\frac{r_o}{\sigma}+1\right)}\left[\operatorname{erf}\left(\frac{r_o}{\sqrt{2\sigma^2}}\right) \pm \operatorname{erf}\left(\frac{|r_{MIN}-r_o|}{\sqrt{2\sigma^2}}\right)\right] \qquad (7.30)$$

the $\pm$ depending on whether $r_{MIN} \gtrless r_o$.

The average bubble standard deviation $\bar{r}$, will then be (for $r_o > r_{MIN}$):

$$\bar{r} = \frac{\int_{r_{MIN}}^{\infty} r\,N(r)\,dr}{\int_{r_{MIN}}^{\infty} N(r)\,dr} = \frac{\frac{\sigma}{\sqrt{2\pi}}\exp\left(-\frac{(r_{MIN}-r_o)^2}{2\sigma^2}\right) + \frac{r_o}{2}\left(\operatorname{erf}\left(\frac{r_o-r_{MIN}}{\sqrt{2\sigma^2}}\right)+1\right)}{1-\frac{N_{LOST}}{N}} \qquad (7.31)$$

The bubble standard deviation r must be related to pulse lengths for use to be made of the above relations. The general relation between maximum pulse length and standard deviation (equn. 7.16) involves discriminator level and spot size, but if we take a first order linear relation between bubble standard deviation and pulse length, for a given discriminator level:

$$T = f(Z) \times r$$

formulae 7.29 and 7.30 can be expressed directly in terms of T_o (the pulse length corresponding to r_o), the ratio $\frac{T_o}{\sigma_T}$ and the cut-off pulse length T_{CUT} .

Using a ''corrected' pulse length, T', as in section (ii) above, the correction factor $\bar{T} - T'$ is graphed in figure 7.10 as a function of $\bar{T}$. The central curve corresponds to $\frac{T_e}{\sigma_T} = 3$ (as in 7.28) and the upper 'error bar' shows the effect of this ratio reaching 3.8, while the lower error bar corresponds to 2.2. It is clear that the correction varies rapidly when the ratio takes larger values. This dependence of the correction on the ratio, and also the non-rigour of the linear approximation between bubble radius and pulse length, means that accurate correction for this factor by this method is not possible in Polly. Fortunately the correction necessary in the normal operating region of Polly is very small (less than 5% at 5 clock pulses), and so a very approximate correction is sufficient.

(iv) Cluster Formation

So far we have derived formulae which apply to the CRT spot image crossing isolated bubbles. We must take account of bubble images merging to form continuous clusters. The effect of cluster formation on equn. 7.1 can be calculated only if some assumption is made about the behaviour of bubble images in this situation. A sensible assumption appears to be that a cluster of bubbles, which cannot be individually resolved by Polly, gives rise to a string of pulses which, away from the ends of the cluster, are each of length T (the maximum pulse length obtained by scanning across the centre of an isolated bubble). (See figure 7.4).

The average number of gaps >a (the resolution distance) is

$$b \exp(-ba) = bL \qquad (7.32)$$

So the number of clusters is bL. The total blob is 1 - L. Thus the average measured pulse length, taking cluster formation into account, is :

$$\bar{T}_{blob} = \frac{bLa\bar{T} + (1 - L - bLa)\, T_{MAX}}{1 - L} \qquad (7.33)$$

Using $b = \frac{1}{a} \log \frac{1}{L}$, (7.33) becomes:

$$\bar{T}_{blob} = \frac{-L(\log L)\,\bar{T} + (1 - L + L \log L)\, T_{MAX}}{1 - L}$$

$$= \left[1 + \frac{(1 - \frac{\pi}{4})\, L \log L}{1 - L}\right] \frac{4}{\pi} \times \bar{T}$$

(since $\bar{T} = \frac{\pi}{4} T_{MAX}$, from 7.16, 7.17, and 7.18).

This correction factor is graphed, as a function of lacunarity, in figure 7.9. As expected, the correction predominates at low lacunarities (dense tracks).

VII.7 Agreement of Corrected Bubble Density Expression with Data

The corrections discussed above are shown superimposed on the data in figure 7.9. For the spot in focus ((focus current, F, around 4.75 or 4.95 units), the corrected points lie on straight lines which do approximately pass through the point ($L = 1.0, \bar{W} = 0$) as desired. The corrected points which correspond to low track widths (where the approximate correction from section (iii) becomes appreciable) tend to deviate from the straight line. (Points with uncorrected $\bar{W}$ less than 25 microns have been omitted from the corrected

graphs, since the correction from section (iii) is large for these). When the spot is badly defocused ($F = 4.25$) the corrections do not improve the results appreciably, and the points no longer lie on a straight line. Some of the formulae (e.g. 7.14) depend on the bubble- spot size ratio lying within a certain range. If the spot becomes very large, through defocusing, the formulae will become less accurate.

Figure 7.11, which includes all the corrected and uncorrected points from figure 7.6 (with the exception of the defocused region, $F = 4.25$) illustrates that using different discrimination levels and spot sizes gives a spread of points about a straight line which, for the corrected points, passes near the point $(L = 1, \bar{W} = 0)$. The spread of average track width on either side of the line, for a fixed lacunarity, is about 5 microns in the lower half of the curve ($\bar{W}$ greater than 30μ), where Polly will normally operate. This gives confidence that bubble densities obtained for a section of track with different discriminator settings and focus conditions will be reliable to within 15%.

No production data from the Glasgow Polly has, at the time of writing, passed through the chain of post-measurement analysis programmes, and so the bubble density from Polly cannot be compared with the momentum of tracks which have been unambiguously identified by the KINEMATICS programme. However, the author measured a two prong event which had been previously measured on the SMP system. The corrections

were applied to the Polly measurements, and the bubble density estimate from Polly compared with the predictions from the KINEMATICS programme, (based on the SMP measurements) and also from direct measurements of the bubble density using a microscope (see Table 7.1). From table 7.1, it is clear that equn. 7.1 seriously underestimates the bubble density of the secondary tracks: the corrected bubble densities agree much better with the bubble density values from the KINEMATICS programme, and the microscope estimates.

VII.8 Conclusion

Despite the assumptions which had to be made in the previous sections to obtain the corrections to the bubble density formulae, these corrections appear to agree sufficiently well with data from Polly. For normal Polly production running, with the cut-off on pulse lengths of one clock pulse duration, a formula for bubble density of the form:

$$b = \frac{k}{v\,(\bar{T} - 0.375)} \times \frac{-1}{\left[\frac{1}{\text{Log}\,L} + \frac{(1-\pi/4)\,L}{1-L}\right]}$$

should give the corrected bubble density. (Here we have used the fact that, above a pulse length of around 4 clock pulses, the combined correction from figures 7.8 and 7.10 is approximately constant, at around $\frac{3}{8}$ of a clock pulse.)

Frequently Used Symbols

A : Fraction of light absorbed by film.

B : $A\left(\frac{\sigma_b^2}{\sigma_s^2 + \sigma_b^2}\right)$

C : $\frac{B}{4}\left[1 + \exp\left(-\frac{g^2}{2s^2}\right)\right]$

D : Distance of closest approach of CRT spot to bubble.

D_{MAX} : Maximum distance between CRT spot, and bubble, for which bubble is still detected.

F : CRT focus current.

H : Number of 'hits'.

L : Lacunarity.

M : Number of 'misses'.

T_{MAX} : Pulse length when CRT spot crosses centre of bubble.

$\bar{T}$: Average pulse length.

T_{CUT} : Minimum pulse length accepted by Polly software.

V : Voltage.

$\bar{W}$: Average track width ($= v\bar{T}$).

Z : Discriminator level.

a : Minimum resolution distance.

b : Bubble density.

d : $\exp\left(-\frac{D^2}{2s^2v^2}\right)$

g : Filter dependent constant (= 1.25 μsec).

k : Time delay introduced by filter.

m : $\frac{T_{CUT}}{T_{MAX}}$

r : Standard deviation of bubble.

s : $\frac{\sqrt{\sigma_s^2 + \sigma_b^2}}{v}$

t : Time.

u : Standard deviation of Gaussian output pulse from

filter, for a Gaussian input pulse of standard deviation r.

v : Velocity of spot image on film.

ω : Frequency.

σ_s : CRT spot standard deviation.

σ_b : Bubble standard deviation.

Track	(1)	(2)	(3)
KINEMATICS PROGRAMME BUBBLE DENSITY	1.35	1.78	2.18
POLLY BUBBLE DENSITY (CORRECTED)	1.35	1.59	2.07
POLLY BUBBLE DENSITY (UNCORRECTED)	1.35	1.45	1.67
MICROSCOPE GAP COUNT BUBBLE DENSITY	1.35	1.9	2.14

(1) Beam Track

(2) Secondary track

(3) Secondary track

The ionisations are in each case normalised to a beam track bubble density of 1.35, which was the KINEMATICS programme estimate.

TABLE 7.1

References

7.1 Argonne National Laboratory Report ANL/HEP 7007

7.2 W.Barkas, Physical Review 124(3),897 (1961)

7.3 P.E.P.R. Engineering Note Number 24
(M.I.T. Internal Report)

Figure Captions

7.1 Density of silver grains across image of two bubbles on film.

7.2 Histogram showing the distribution of bubble radii along a beam track.

7.3 Bubble centre separations, obtained from the same data as figure 7.2. N(x) is the number of separations greater than 'x'.

7.4 Diagrammatic representation of a cluster of unresolved bubbles used in the derivation of equation 7.33.

7.5 Comparison of predicted photomultiplier output (after passing through filter) from equations 7.10 (solid line) and 7.14 (crosses).

7.6 Lacunarity plotted against average track width for data points corresponding to six C.R.T focus currents. The straight lines are visual fits to the data points. In the case of the corrected points, shown as crosses, points corresponding to low average track widths are not included in the fits (see Chapter VII, section 7)

7.7 Effect of phosphor rise and fall time on filtered photomultiplier output pulse.

7.8 Correction to average pulse length, due to low pulse cut-off.

7.9 As 7.8, but showing cluster formation correction.

7.10 As 7.8, but showing correction for non-uniformity of bubble sizes. The 'error bars' correspond to the uncertainty in the spread of radii along a track.

7.11 Scatter plot of lacunarity against average track width. This shows all the data points from fig. 7.6, except those for which the CRT focus current $\neq 4.25$ Units.

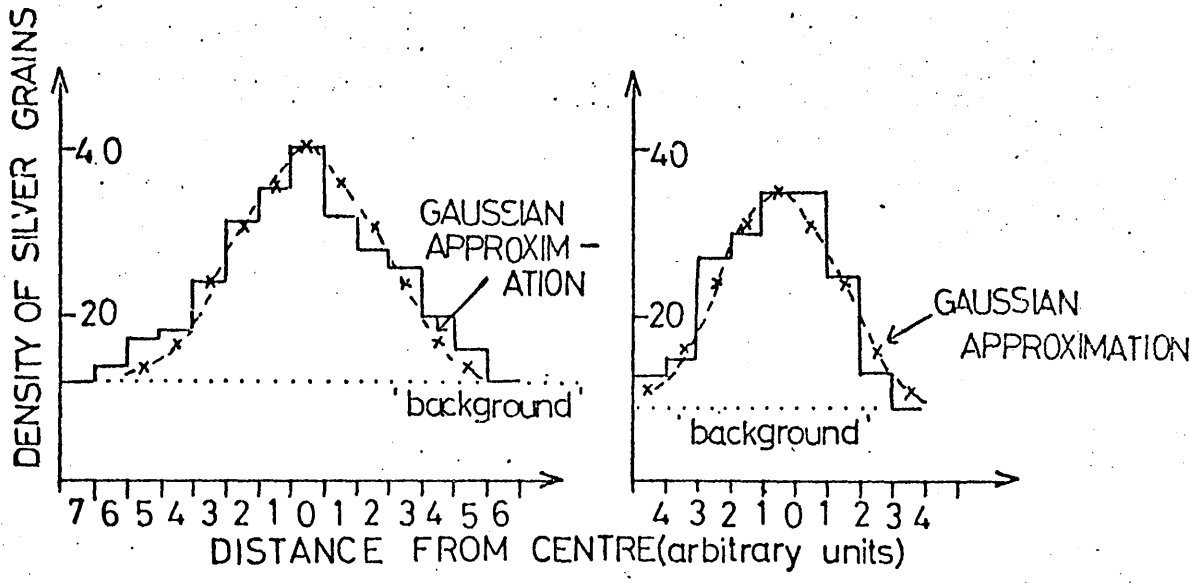

GRAIN DENSITY ACROSS TWO BUBBLE IMAGES

FIGURE 7.1

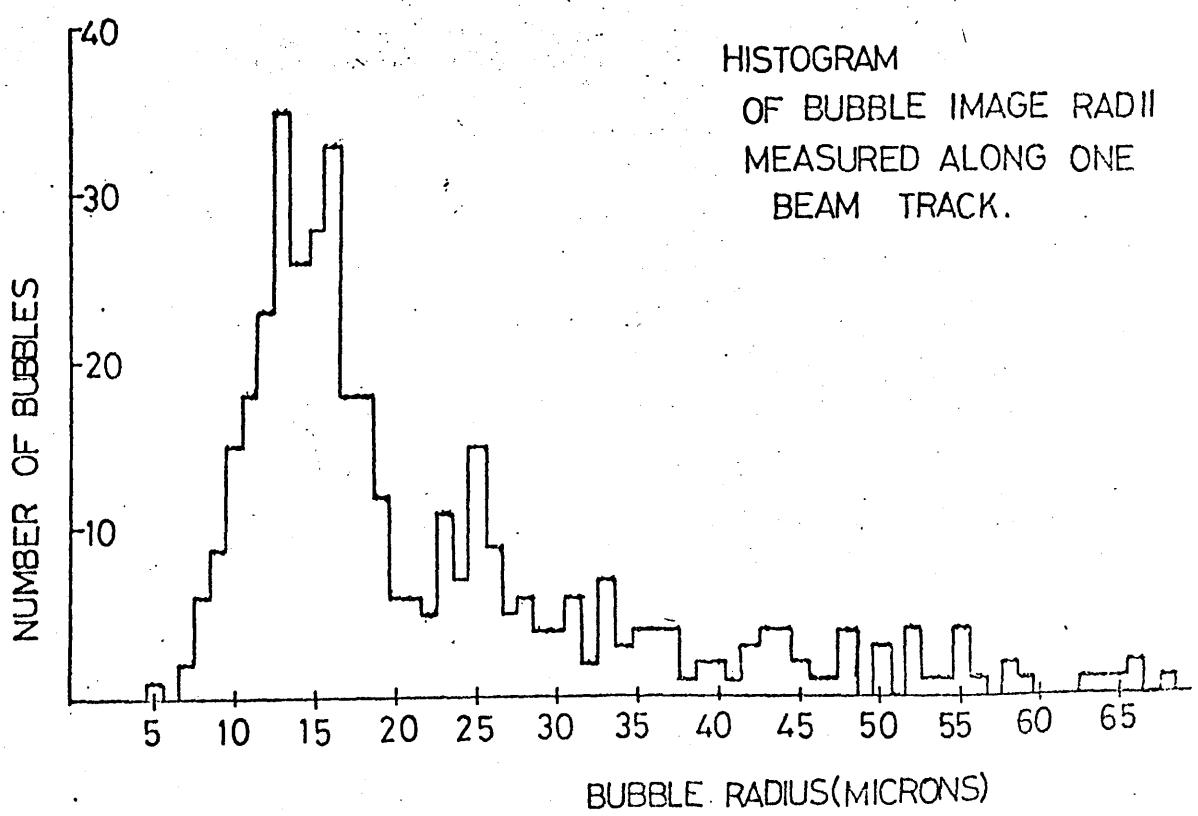

FIGURE 7.2

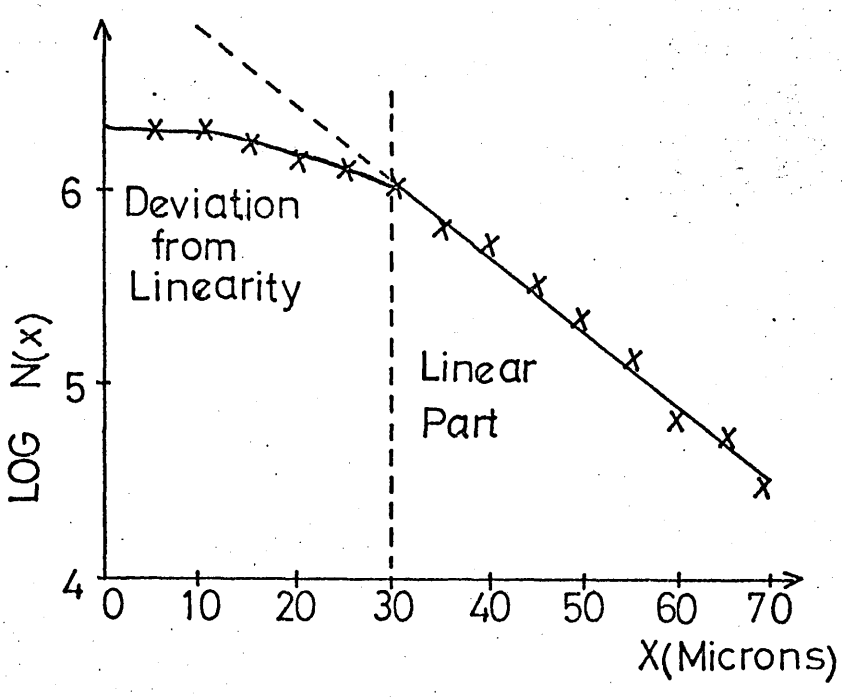

BUBBLE SEPARATIONS

FIGURE 7.3

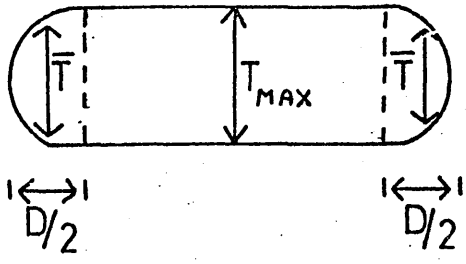

REPRESENTATION OF A CLUSTER OF UNRESOLVED BUBBLE IMAGES.

FIGURE 7.4

FIGURE 7.5

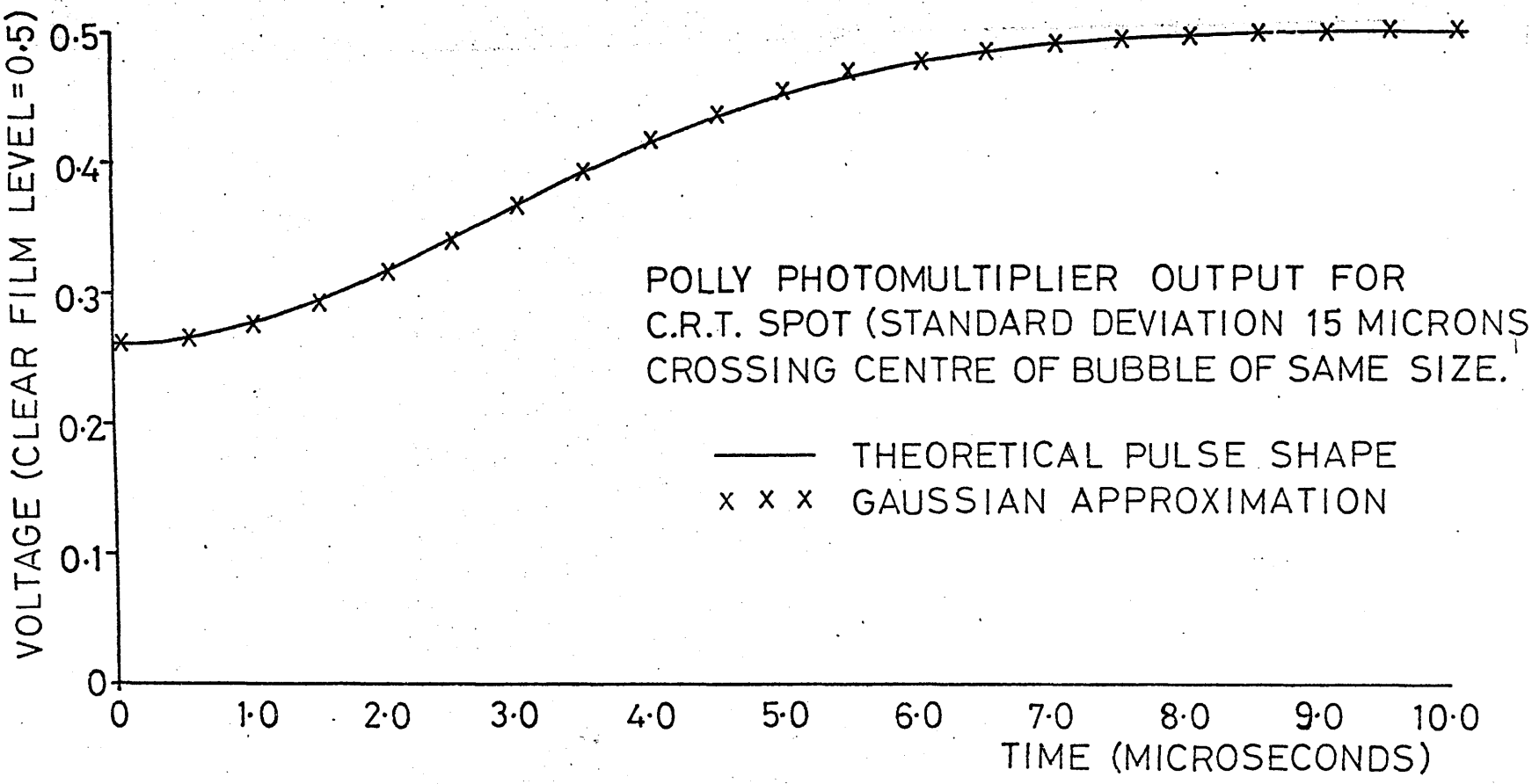
VOLTAGE (CLEAR FILM LEVEL = 0·5)
0·5
0·4
0·3
0·2
0·1
0
0
1·0
2·0
3·0
4·0
5·0
6·0
7·0
8·0
9·0
10·0
TIME (MICROSECONDS)
POLLY PHOTOMULTIPLIER OUTPUT FOR
C.R.T. SPOT (STANDARD DEVIATION 15 MICRONS)
CROSSING CENTRE OF BUBBLE OF SAME SIZE.
THEORETICAL PULSE SHAPE
x x x GAUSSIAN APPROXIMATION

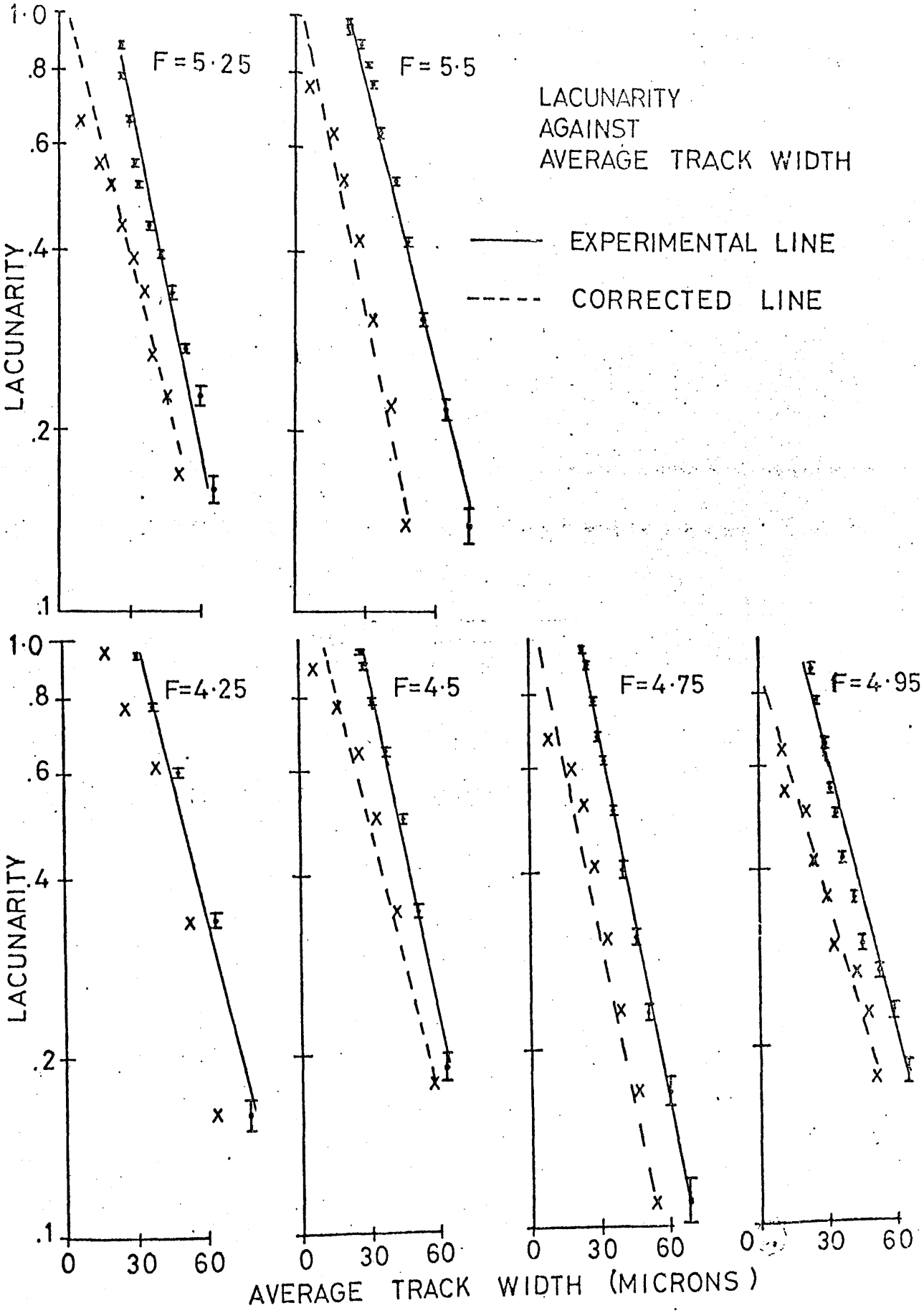
LACUNARITY AGAINST AVERAGE TRACK WIDTH
EXPERIMENTAL LINE
CORRECTED LINE
F = 5·25
F = 5·5
F=4·25
F=4·5
F=4·75
F=4·95
LACUNARITY
1·0
.8
.6
.4
.2
.1
0
30
60
AVERAGE TRACK WIDTH (MICRONS)

FIGURE 7.6

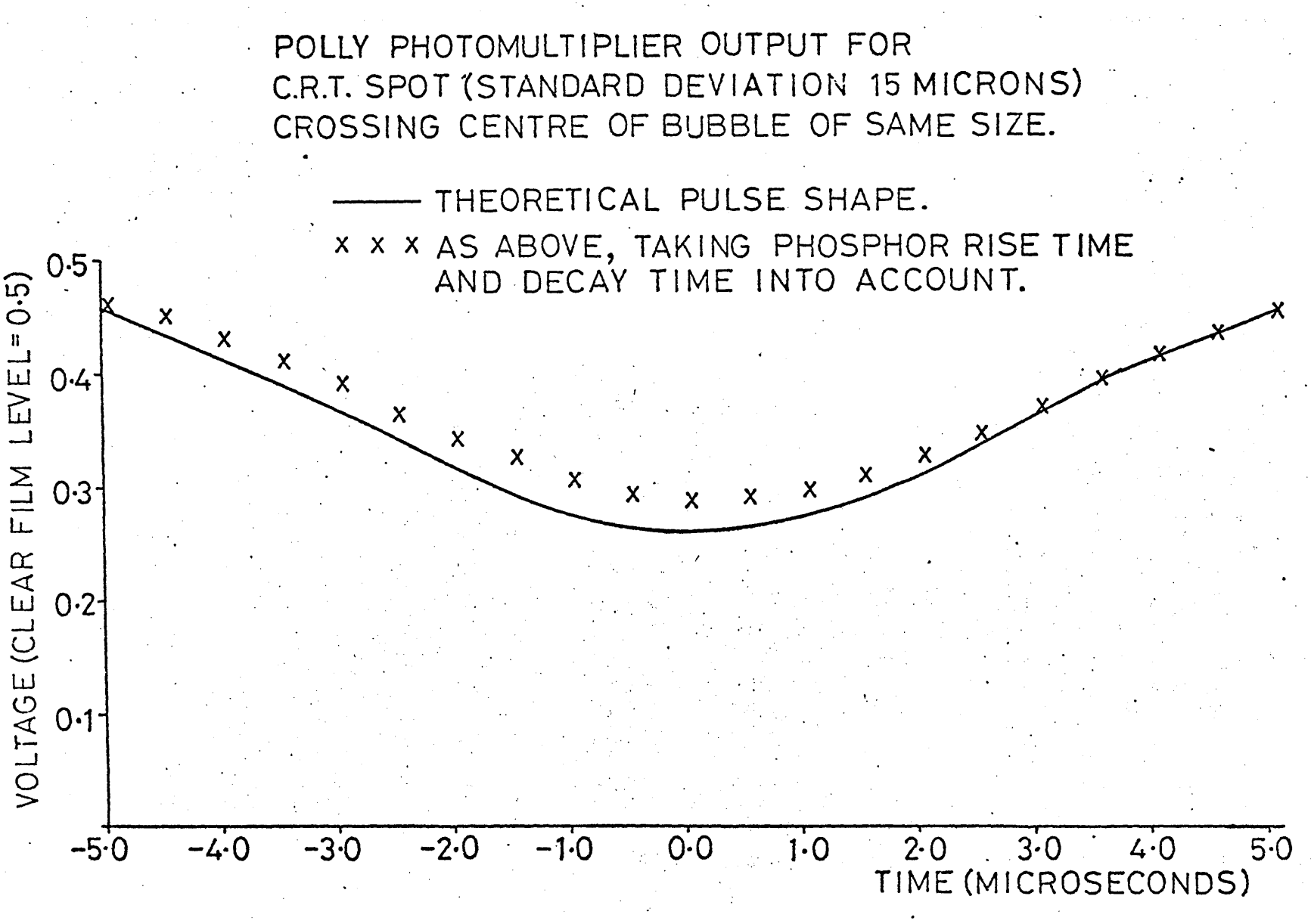
POLLY PHOTOMULTIPLIER OUTPUT FOR
C.R.T. SPOT (STANDARD DEVIATION 15 MICRONS)
CROSSING CENTRE OF BUBBLE OF SAME SIZE.
—— THEORETICAL PULSE SHAPE.
x x x AS ABOVE, TAKING PHOSPHOR RISE TIME
AND DECAY TIME INTO ACCOUNT.
VOLTAGE (CLEAR FILM LEVEL = 0·5)
0·5
0·4
0·3
0·2
0·1
-5·0
-4·0
-3·0
-2·0
-1·0
0·0
1·0
2·0
3·0
4·0
5·0
TIME (MICROSECONDS)

FIGURE 7.7

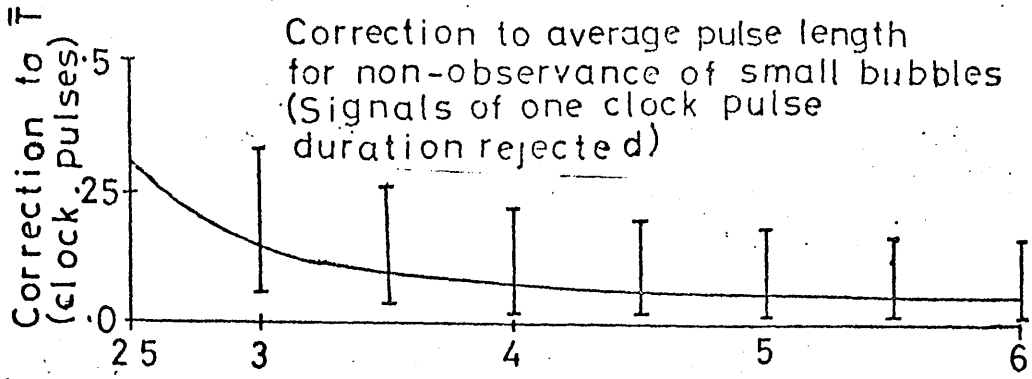

FIGURE 7.10

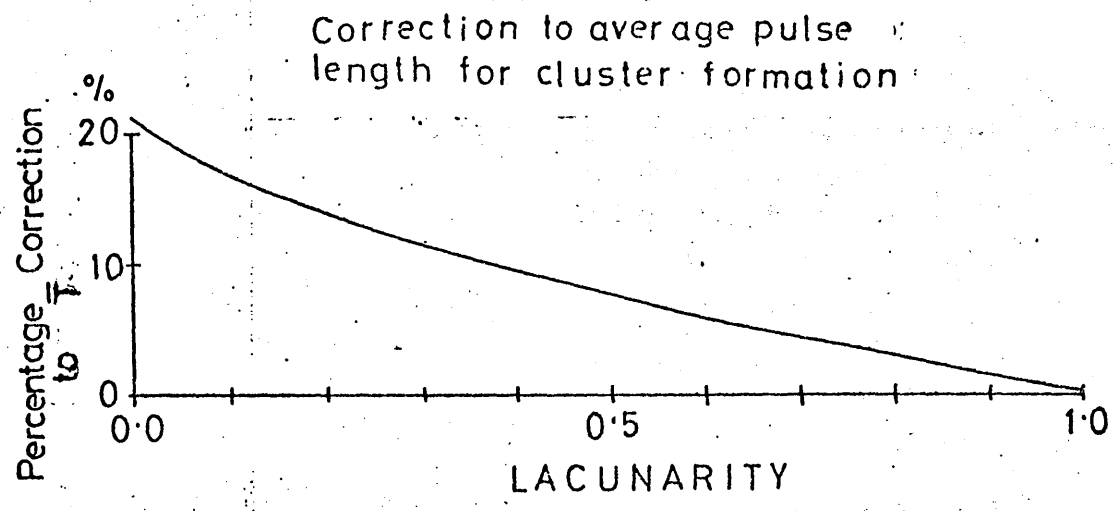

FIGURE 7.9

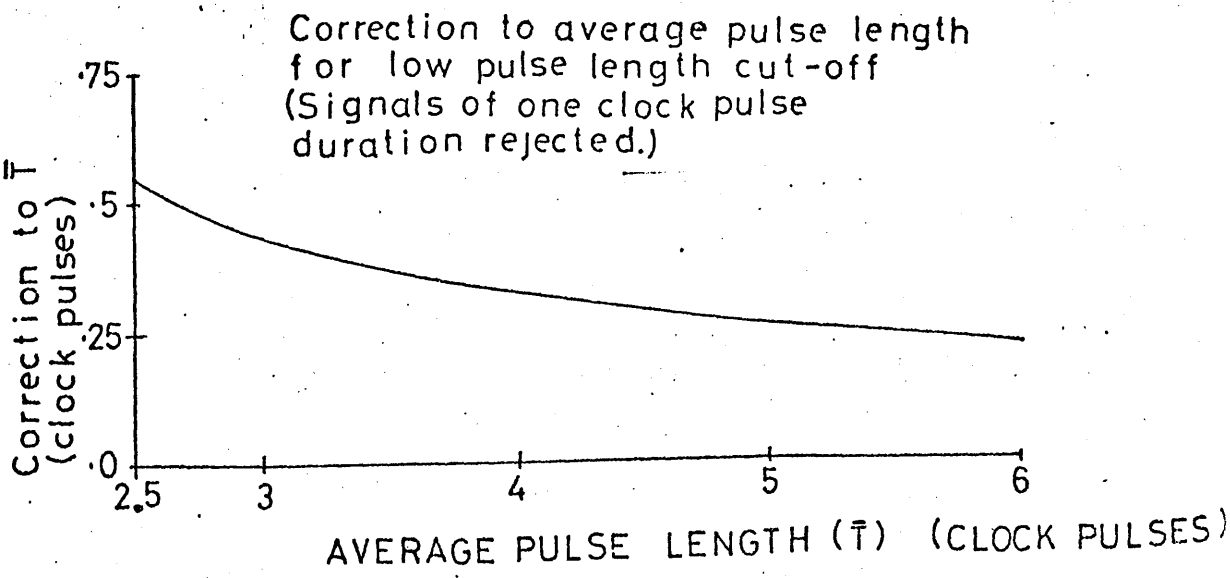

FIGURE 7.8

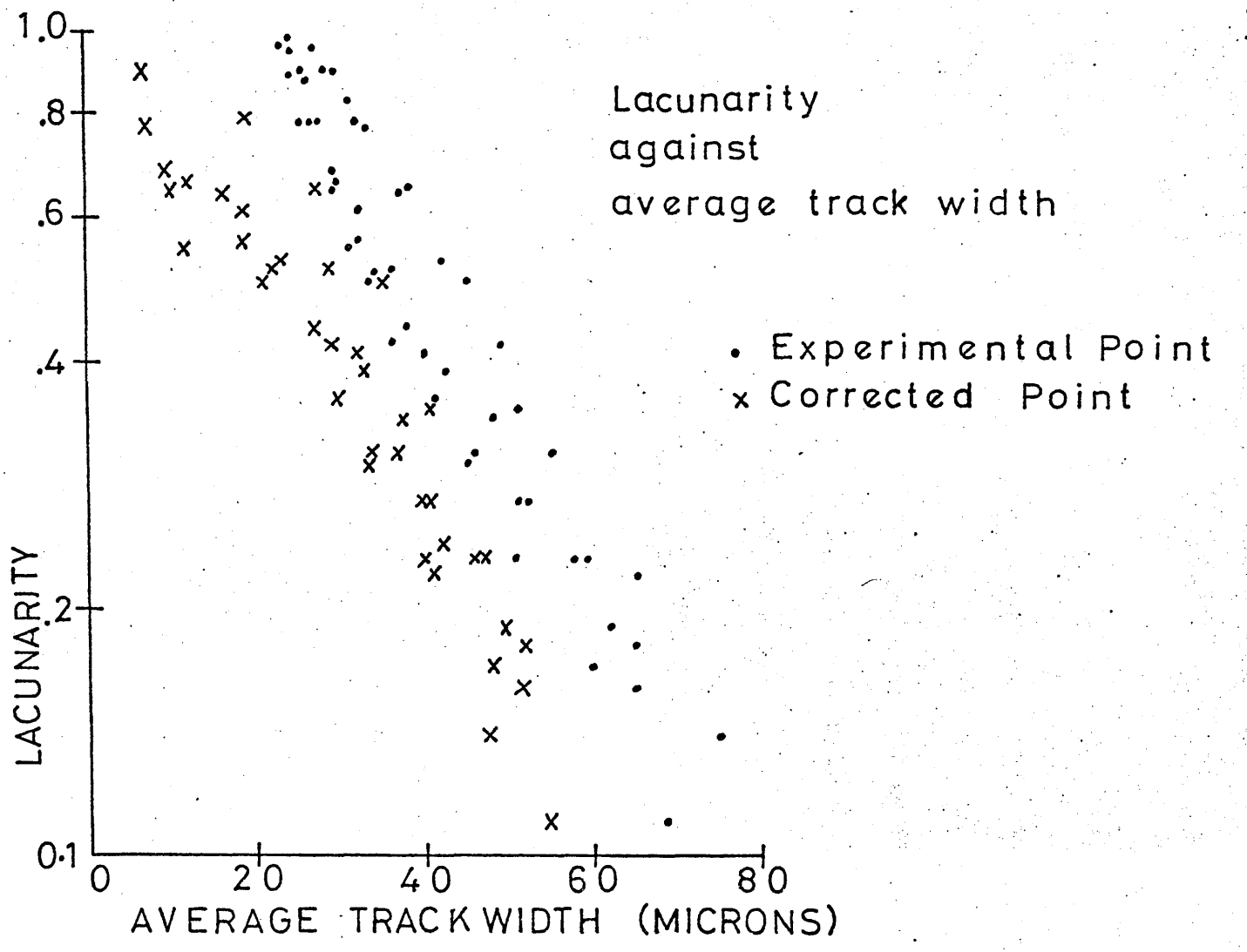
Lacunarity
against
average track width
• Experimental Point
x Corrected Point
LACUNARITY
1.0
.8
.6
.4
.2
0·1
0
20
40
60
80
AVERAGE TRACK WIDTH (MICRONS)

FIGURE 7.11

Appendix

Dalitz Plot and Angular Distribution

The transition amplitude from an initial state of $p\pi^+\pi^-$ spin $|J,\lambda\rangle$, to a final state of proton spin $|1/2,m_s\rangle$ ($T^J_{\lambda m_s}$ say) can be derived by considering the two-step decay:

$$N^* \longrightarrow \Delta^{++}(1236)\pi^- \qquad (A.1)$$

$$\Delta^{++}(1236) \rightarrow p\pi^+ \qquad (A.2)$$

and the isospin related processes:

$$N^* \longrightarrow \Delta^{0}(1236)\pi^+ \qquad (A.1')$$

$$\Delta^{0}(1236) \rightarrow p\pi^- \qquad (A.2')$$

The orbital angular momentum for the decay of an N^* of spin-parity J^P via $\Delta(1236)\pi$ is, for a parity conserving decay, given in the table below.

J^P	Possible Decay Angular Momenta
$1/2^+$	1
$3/2^-$	0,2
$5/2^+$	1,3

For $J^P = 3/2^-$ and $5/2^+$, it is assumed in the analysis that the lower angular momentum is dominant in the decay.

For the decay of the $\Delta(1236)$ via $p\pi$, $\ell' = 1$ is the only orbital angular momentum state possible for the $p - \pi^+$ system after decay. For decay (1), the appropriate decay factors are of the form:

$$C \langle J\, 3/2\, \ell \,|\, m_\Delta\, m_\ell\rangle\, Y_\ell^m(\theta,\phi)\, |\underline{p}|^\ell$$

where $|\ell, m_\ell\rangle$ is the orbital angular momentum of $\Delta(1236)-\pi$

system after decay of N^*: $m_\Delta (= \lambda - m_\ell)$ is the z-component of spin of $\Delta(1236)$: $\underset{\sim}{p}$ is the $\Delta(1236)$ momentum in the $p\pi\pi$ centre-of-mass system, and $|\underset{\sim}{p}|^\ell$ is an angular momentum barrier factor for the decay of the N^*: (θ, ϕ) are the angles describing the $\Delta(1236)$ line of flight direction in the N^* centre-of-mass (see figure 3.10).

For decay (2), we have factors of the form:

$$C \langle 3/2\ 1/2\ \ell' | m_s\ m_{\ell'} \rangle\ Y_{\ell'}^{m_{\ell'}}(\theta', \phi')\ BW(\Delta)$$

where $|\ell', m_{\ell'}\rangle$ (with $m_{\ell'} = m_\Delta - m_s$) is orbital angular momentum of $p - \pi$ system after decay of $\Delta(1236)$. (θ', ϕ') are the angles describing the proton line of flight direction in the $\Delta(1236)$ centre-of-mass (see figure 3.10). $BW(\Delta)$ is the form of Breit-Wigner (from refs. 3.10 and 3.11) appropriate for the decay of $\Delta(1236)$.

The Breit-Wigner function for the decay of the Δ in the analysis is:

$$BW \propto \sqrt{\frac{E}{q}} \left[\frac{\sqrt{E_0 \Gamma(E)}\,(E^2 - E_0^2)}{(E^2 - E_0^2)^2 + (E_0 \Gamma(E))^2} - \frac{i\,(E_0 \Gamma(E))^{3/2}}{(E^2 - E_0^2)^2 + E_0 \Gamma(E))^2} \right]$$

where E = energy of Δ^{++} in $(\Delta\pi)$ centre-of-mass system

q = momentum of proton in $\Delta(1236)$ centre-of-mass system

The energy dependence for the width:

$$\Gamma(E) = \Gamma_0 \left(\frac{q}{q_0} \right)^{2\ell+1} \frac{E_0\,(0.35 + q_0^2)^\ell}{E\,(0.35 + q^2)^\ell}$$

is the empirical form (reference 3.10). The mass and width for the $\Delta(1236)$ were taken as $E_0 = 1.236$ GeV, $\Gamma_0 = .12$ GeV.

For the $N^*(1470)$ terms included in the highest $p\pi^+\pi^-$ mass interval, a simple Breit-Wigner of mass 1.4 GeV/c^2 and width 100 MeV/c^2 was employed. The mass value was based on

the data in reference 3.12, rather than on phase shift values which tend to indicate a higher mass. Since we used a simple Breit-Wigner for the Roper resonance, the mass values from production experiments (as reference 3.12) are more appropriate here than phase shift values.

The relation between processes (1,2) and (1',2') are obtained from the isospin Clebsch-Gordan coefficients for the processes:

$$N^*(I=\tfrac{1}{2}, I_3=\tfrac{1}{2}) \xrightarrow{1/2} \pi^-\Delta^{++} \xrightarrow{1} p\pi^+$$
$$N^*(I=\tfrac{1}{2}, I_3=\tfrac{1}{2}) \xrightarrow{1/6} \pi^+\Delta^{0} \xrightarrow{1/3} p\pi^-$$
$$\pi^+\Delta^{0} \xrightarrow{2/3} n\pi^0$$

giving the ratio $\dfrac{\text{probability of decay via } \Delta^0\pi^+}{\text{probability of decay via } \Delta^{++}\pi^-} = \dfrac{1}{9}$

The transition amplitude via $\Delta^q\pi^-$ (where q is the charge of the $\Delta(1236)$) can be written:

$$T^J_{\lambda m_s}(\Delta^q) = \sum_{m_{\ell'}} \sum_{m_\ell} C\langle J\ 3/2\ \ell | m_\Delta m_\ell\rangle C\langle 3/2\ 1/2\ \ell' | m_s m_{\ell'}\rangle \times |p|^\ell \times Y^\ell_{m_\ell}(\theta,\phi)\ Y^{\ell'}_{m_{\ell'}}(\theta',\phi')\ BW(\Delta^q)$$

The overall transition amplitude from an initial N^* state of spin J is:

$$T^J_{\lambda m_s} = T^J_{\lambda m_s}(\Delta^{++}) + \tfrac{1}{3}\ T^J_{\lambda m_s}(\Delta^0)$$

and the amplitude expression, summing over N^* spin states, is

$$T_{\lambda m_s} = \sum R_J \exp(i\phi_J)\ T^J_{\lambda m_s}$$

where the R_J are real numbers, the square of which represent the relative proportion of different N^* spin states, and the ϕ_J are the relative phases.

The Dalitz Plot intensity expression in this case is:

$$I = \frac{1}{2}\sum_{\lambda m_s} |T_{\lambda m_s}|^2 + S \qquad (A.3)$$

where we average over the initial proton helicity and sum

over the final proton spin z-component m_s. The constant 'S' represents the non-interfering three body phase space decay, which gives a uniform Dalitz plot density.

Fitting the intensity expression to the data was carried out by maximising the log likelihood function:

$$L(R, \phi) = \sum_i \text{Log} \frac{I_i(R, \phi)}{N(R, \phi)}$$

with respect to the sets of variables R and ϕ. I is the intensity expression (eqn. A.3) evaluated for the 'i' event. N is a normalisation factor, obtained by phase space integration of the intensity expression using the programme FOWL (ref. 2.10). For the $p\pi^+\pi^-$ spin values which were fitted to the data ($J^P = 1/2^+, 3/2^-, 5/2^+$), there correspond five parameters (one of the relative phase factors can be arbitrarily fixed). Maximising the function L with respect to these parameters was performed by the programme MINUIT (ref. 2.9).